

# **Lawrence Berkeley National Laboratory**

## Lawrence Berkeley National Laboratory

### **Title**

Sequestration of Carbon Dioxide with Enhanced Gas Recovery-Case Study Altmark, North German Basin

### **Permalink**

<https://escholarship.org/uc/item/7sj2g8mc>

### **Authors**

Rebscher, Dorothee  
Oldenburg, Curtis M.

### **Publication Date**

2005-10-12

## Sequestration of Carbon Dioxide with Enhanced Gas Recovery — Case Study Altmark, North German Basin

Dorothee Rebscher  
Curtis M. Oldenburg

Earth Sciences Division 90-1116  
Lawrence Berkeley National Laboratory  
Berkeley, CA 94720  
December 2005

This work was supported by the European Project CO<sub>2</sub>-STORE under Contract No. ENK5-CT-2002-99621 and by the Lawrence Berkeley National Laboratory under Department of Energy Contract No. DE-AC03-76SF00098.

# Contents

<b>1</b>	<b>Introduction</b>	<b>6</b>
<b>2</b>	<b>Background</b>	<b>6</b>
<b>3</b>	<b>Method</b>	<b>8</b>
<b>4</b>	<b>Altmark Gas Reservoir</b>	<b>9</b>
<b>5</b>	<b>Requirements for Sequestration of Carbon Dioxide</b>	<b>13</b>
<b>6</b>	<b>Gas Mixture Properties</b>	<b>16</b>
6.1	Compressibility factor . . . . .	18
6.2	Density . . . . .	19
6.3	Viscosity . . . . .	20
<b>7</b>	<b>Development of the Hydrostratigraphic Model</b>	<b>21</b>
<b>8</b>	<b>Two-dimensional Simulation</b>	<b>23</b>
<b>9</b>	<b>Three-dimensional Simulation of a Base-case</b>	<b>27</b>
9.1	Production . . . . .	29
9.2	Injection . . . . .	29
9.3	CH <sub>4</sub> Extraction and CO <sub>2</sub> Injection Phase . . . . .	29
9.4	Relaxation Phase . . . . .	31
<b>10</b>	<b>Variation of the Injection Rates in the 3D Model</b>	<b>31</b>
10.1	CH <sub>4</sub> Extraction and CO <sub>2</sub> Injection Phase . . . . .	31
<b>11</b>	<b>Variation of the Permeabilities in the 3D Model</b>	<b>32</b>
11.1	Breakthrough During the CH <sub>4</sub> Extraction and CO <sub>2</sub> Injection Phase . . . . .	32
11.2	Relaxation Phase . . . . .	33
<b>12</b>	<b>Variation of Injection Strategies in the 3D Model</b>	<b>33</b>
12.1	Strategy . . . . .	34
12.2	Blocking One Layer with Different Amounts of Water for 5 years . . . . .	34
12.3	Blocking Two Layers with Different Amounts of Water for 5 years . . . . .	34
12.4	Blocking Two Layers with Different Amounts of Water for 10 years . . . . .	37
<b>13</b>	<b>Overall Summary</b>	<b>39</b>
<b>14</b>	<b>Discussion</b>	<b>40</b>
<b>15</b>	<b>Conclusions</b>	<b>41</b>
<b>16</b>	<b>Outlook</b>	<b>41</b>
<b>17</b>	<b>Acknowledgment</b>	<b>41</b>

## List of Figures

1	Map of Germany and Sachsen-Anhalt . . . . .	9
2	Map of the Altmark . . . . .	10
3	Production history of the natural gas fields in the Altmark . . . . .	11
4	Map of the Altmark region . . . . .	11
5	Subsidence in time based on data from the well Boizenburg . . . . .	13
6	Phase diagram for CO <sub>2</sub> . . . . .	15
7	Depth dependent CO <sub>2</sub> density and solubility in saline formation water for the North German Basin . . . . .	16
8	Labeling of the axes in the triangular diagrams . . . . .	17
9	Schematic illustration of end-member property distributions in CH <sub>4</sub> -N <sub>2</sub> -CO <sub>2</sub> systems. In the first triangle, a N <sub>2</sub> -free model is not good. In the second and third triangles a N <sub>2</sub> -free model gives a good approximation to the three-component real system. . . . .	18
10	The main area of interest in the triangular diagram of a CH <sub>4</sub> -N <sub>2</sub> -CO <sub>2</sub> system is the hatched area, which represents the conditions of the Altmark gas, which is 8 % — 60 % CH <sub>4</sub> , 40 % — 90 % N <sub>2</sub> . . . . .	19
11	Map of wells in the natural gas reservoir Peckensen . . . . .	21
12	Schematic of the five-spot configuration . . . . .	22
13	Sketch of the grid used in the 3D simulations . . . . .	23
14	Sketch of the 2D grid used in the simulations . . . . .	24
15	Variation of water injection rate — comparison of breakthrough times . . . . .	37
16	Compressibility-factor in the gas system CH <sub>4</sub> -N <sub>2</sub> -CO <sub>2</sub> (1) . . . . .	48
17	Compressibility-factor in the gas system CH <sub>4</sub> -N <sub>2</sub> -CO <sub>2</sub> (2) . . . . .	49
18	Density in the gas system CH <sub>4</sub> -N <sub>2</sub> -CO <sub>2</sub> (1) . . . . .	50
19	Density in the gas system CH <sub>4</sub> -N <sub>2</sub> -CO <sub>2</sub> (2) . . . . .	51
20	Viscosity in the gas system CH <sub>4</sub> -N <sub>2</sub> -CO <sub>2</sub> (1) . . . . .	52
21	Viscosity in the gas system CH <sub>4</sub> -N <sub>2</sub> -CO <sub>2</sub> (2) . . . . .	53
22	2D simulation of the high-permeability layer Z9–11 — pressure . . . . .	54
23	2D simulation of the high-permeability layer Z9–11 — liquid saturation . . . . .	55
24	2D simulation of the high-permeability layer Z9–11 — CO <sub>2</sub> mass fraction in the gas phase . . . . .	56
25	2D simulation of the high-permeability layer Z9–11 — CO <sub>2</sub> mass fraction in the liquid phase . . . . .	57
26	2D simulation of the Cases b1 to b11 — pressure after 1 year . . . . .	58
27	2D simulation of the Cases b13 to b18 — pressure after 1 year . . . . .	59
28	2D simulation of the Cases b1 to b11 — liquid saturation after 1 year . . . . .	60
29	2D simulation of the Cases b13 to b18 — liquid saturation after 1 year . . . . .	61
30	2D simulation of the Cases b1 to b11 — CO <sub>2</sub> mass fraction in the gas phase after 1 year . . . . .	62
31	2D simulation of the Cases b13 to b18 — CO <sub>2</sub> mass fraction in the gas phase after 1 year . . . . .	63
32	2D simulation of the Cases b1 to b11 — CO <sub>2</sub> mass fraction in the liquid phase after 1 year . . . . .	64

33	2D simulation of the Cases b13 to b18 — CO <sub>2</sub> mass fraction in the liquid phase after 1 year . . . . .	65
34	2D simulation of the Cases b1 to b11 — pressure after 40 years . . . . .	66
35	2D simulation of the Cases b13 to b18 — pressure after 40 years . . . . .	67
36	2D simulation of the Cases b1 to b11 — liquid saturation after 40 years . . . . .	68
37	2D simulation of the Cases b13 to b18 — liquid saturation after 40 years . . . . .	69
38	2D simulation of the Cases b1 to b11 — CO <sub>2</sub> mass fraction in the gas phase after 40 years . . . . .	70
39	2D simulation of the Cases b13 to b18 — CO <sub>2</sub> mass fraction in the gas phase after 40 years . . . . .	71
40	2D simulation of the Cases b1 to b11 — CO <sub>2</sub> mass fraction in the liquid phase after 40 years . . . . .	72
41	2D simulation of the Cases b13 to b18 — CO <sub>2</sub> mass fraction in the liquid phase after 40 years . . . . .	73
42	Three dimensional pressure distribution during the extraction and injection phase . . . . .	74
43	Diagonal slice of the pressure distribution during the extraction and injection phase . . . . .	75
44	Distribution of the liquid saturation during the extraction and injection phase . . . . .	76
45	Distribution of the CO <sub>2</sub> mass fraction in the liquid phase during the extraction and injection phase . . . . .	77
46	Distribution of the CH <sub>4</sub> mass fraction in the liquid phase during the extraction and injection phase . . . . .	78
47	Distribution of the CH <sub>4</sub> mass fraction in the gas phase during the extraction and injection phase . . . . .	79
48	Distribution of the CO <sub>2</sub> mass fraction in the gas phase during the extraction and injection phase . . . . .	80
49	Pressure in layer Zyk13 . . . . .	81
50	CO <sub>2</sub> mass fraction in the gas phase in layer Zyk13 . . . . .	82
51	CH <sub>4</sub> mass fraction in the gas phase in layer Zyk13 . . . . .	83
52	Extraction and injection phase of the base-case — pressure in time . . . . .	84
53	Extraction and injection phase of the base-case — CO <sub>2</sub> mass fraction in gas phase in time . . . . .	85
54	Extraction and injection phase of the base-case — CH <sub>4</sub> mass fraction in gas phase in time . . . . .	86
55	Simulations of the relaxation phase — pressure . . . . .	87
56	Simulations of the relaxation phase — liquid saturation . . . . .	88
57	Simulations of the relaxation phase — CH <sub>4</sub> mass fraction in the gas phase . . . . .	89
58	Simulations of the relaxation phase — CH <sub>4</sub> mass fraction in the liquid phase . . . . .	90
59	Simulations of the relaxation phase — CO <sub>2</sub> mass fraction in the gas phase . . . . .	91
60	Simulations of the relaxation phase — CO <sub>2</sub> mass fraction in the liquid phase . . . . .	92
61	Variation of the injection rate — pressure distribution after 1 year of CH <sub>4</sub> extraction and CO <sub>2</sub> injection . . . . .	93
62	Variation of the injection rate — distribution of CO <sub>2</sub> mass fraction in the gas phase after 1 year of CH <sub>4</sub> extraction and CO <sub>2</sub> injection . . . . .	94
63	Variation of the injection rate — pressure distribution after 40 years of CH <sub>4</sub> extraction and CO <sub>2</sub> injection . . . . .	95

64	Variation of the injection rate — distribution of CO <sub>2</sub> mass fraction in the gas phase after 40 years of CH <sub>4</sub> extraction and CO <sub>2</sub> injection . . . . .	96
65	Variation of the permeabilities in Cases a1 to a11 — pressure after 1 year . . . . .	97
66	Variation of the permeabilities in Cases a1 to a11 — CO <sub>2</sub> mass fraction in the gas phase after 1 year . . . . .	98
67	CO <sub>2</sub> breakthrough in the 3D simulations . . . . .	99
68	Variation of permeabilities — comparison of breakthrough times . . . . .	100
69	Variation of permeabilities — time dependence of CO <sub>2</sub> mass fraction in the gas phase of the breakthrough layers . . . . .	101
70	Variation of permeabilities — pressure of seven cases in the relaxation phase . . . . .	102
71	Variation of permeabilities — liquid saturation <i>SL</i> of seven cases in the relaxation phase . . . . .	103
72	Variation of permeabilities — CH <sub>4</sub> mass fraction in the gas phase of seven cases in the relaxation phase . . . . .	104
73	Variation of permeabilities — CH <sub>4</sub> mass fraction in the liquid phase of seven cases in the relaxation phase . . . . .	105
74	Variation of permeabilities — CO <sub>2</sub> mass fraction in the gas phase of seven cases in the relaxation phase . . . . .	106
75	Variation of permeabilities — CO <sub>2</sub> mass fraction in the liquid phase of seven cases in the relaxation phase . . . . .	107
76	H <sub>2</sub> O blocking of 2 layers — Case f . . . . .	108
77	H <sub>2</sub> O blocking of 2 layers — Cases f to i after 1 year and 2 years . . . . .	109
78	H <sub>2</sub> O blocking of 2 layers — CO <sub>2</sub> mass fraction in the gas phase during the CH <sub>4</sub> extraction and CO <sub>2</sub> injection phase . . . . .	110

## List of Tables

1	Characteristics of the Altmark reservoir . . . . .	12
2	Characteristics of the gas bearing sequences in the Western Altmark . . . . .	14
3	Main components of the natural gas in the Salzwedel-Peckensen reservoir . . . . .	14
4	Model characteristics . . . . .	22
5	Parameters used in the 2D simulations (i) . . . . .	25
6	Parameters used in the 2D simulations (ii) . . . . .	25
7	Parameters used in the 2D simulations (iii) . . . . .	25
8	Characteristics of the 3D simulations with different permeabilities . . . . .	28
9	Overview of the variations of the total injection rate . . . . .	32
10	Properties of the H <sub>2</sub> O-blocking scenarios . . . . .	35
11	Overview for the delay of breakthrough due to H <sub>2</sub> O blocking of 2 units . . . . .	36
12	Overview for the delay of breakthrough due to H <sub>2</sub> O blocking of two units with different parameters . . . . .	38

## 1 Introduction

Geologic carbon dioxide storage is one strategy for reducing CO<sub>2</sub> emissions into the atmosphere. Depleted natural gas reservoirs are an obvious target for CO<sub>2</sub> storage due to their proven record of gas containment. Germany has both large industrial sources of CO<sub>2</sub> and depleting gas reservoirs. The purpose of this report is to describe the analysis and modeling performed to investigate the feasibility of injecting CO<sub>2</sub> into nearly depleted gas reservoirs in the Altmark area in North Germany for geologic CO<sub>2</sub> storage with enhanced gas recovery.

## 2 Background

In 1997 the Kyoto Protocol [United Nations Framework Convention on Climate Change, 1997] raised public awareness of the anthropogenic effect on climate due to greenhouse gas emissions. Ratified now by 128 nations, it came into force on February 16, 2005. The greenhouse gas CO<sub>2</sub> is more and more acknowledged in science, politics, and society worldwide in the complex problem of global warming. Today's concentration in the atmosphere amounts to about 372 ppm, which is higher than at any time in at least the past 420 000 years [King, 2004]. Facing the expected continued global economic growth in the coming decades, studies on carbon-cycle models for various atmospheric CO<sub>2</sub> stabilization scenarios emphasize the need for action [Hoffert et al., 1998].

Obvious solutions include reduced consumption of energy, optimized power plant technologies, an increase in the efficiency of energy use, and lower carbon and carbon-free energy sources [Ybema et al., 1997]. Besides efforts for reduced generation of CO<sub>2</sub> [Geipel et al., 2003a,b] and sequestration in terrestrial ecosystems [Albrecht and Kandji, 2003], additional studies, like the investigation of new potential sinks of CO<sub>2</sub>, are necessary. Different approaches are recently discussed — the deep ocean [Ametistova et al., 2002], deep saline aquifers [White et al., 2003], gas and oil reservoirs [Oldenburg et al., 2001], coalbeds [White et al., 2003], advanced biological and chemical processes [U.S. Department of Energy, 1999], and carbon dioxide recycling [Hashimoto et al., 2001].

Some of the most important potential sinks are deep subsurface geologic formations. Estimates of the global sequestration capacity in geological formations amounts to  $9.23 \times 10^{14}$  kg of CO<sub>2</sub> [Stevens et al., 2000]. Depleted or nearly depleted gas and oil reservoirs are good candidates for permanent disposal for the following reasons:

- (i) Gas reservoirs have proven ability to store gases on geologic time scales, therefore minimizing the risk of CO<sub>2</sub> leakage to the atmosphere.
- (ii) The geological settings are already well studied by the operating hydrocarbon industry.
- (iii) Use of exploited hydrocarbon reservoirs leaves other regions undisturbed.
- (iv) Sequestration in hydrocarbon reservoirs does not require a large amount of new surface infrastructure and impact.
- (v) CO<sub>2</sub> injection into hydrocarbon reservoirs allows the simultaneous enhancement of oil and natural gas recovery, providing a potential subsidy on the cost of injection. In particular,

within the last two years much experience was gained concerning enhanced oil recovery (EOR) by injecting anthropogenic CO<sub>2</sub> at the Weyburn oil field (southeast Saskatchewan, Canada) e.g., [Islam et al., 1999]. Enhanced gas recovery may also be possible as the amount of gas left in place in depleted gas reservoirs may be significant. The average recovery factor is about 75 %, ranging from 30 % to almost 100 % [Laherrére, 1997]. The injection of CO<sub>2</sub> can be used to increase reservoir pressure and thereby displace the remaining gas toward production wells. We call this concept “carbon sequestration with enhanced gas recovery” (CSEGR). CSEGR is not new, but so far no results are known about testing in the field. This may change, as Gaz de France started to inject CO<sub>2</sub> in the dutch offshore K12b gas field by the midyear of 2004 [Gaz de France, 2005] and began simultaneously natural gas production and CO<sub>2</sub> injection in April 2005 [May, pers. comm., 2005]. Feasibility studies estimate that CSEGR is economic under current conditions at CO<sub>2</sub> supply costs of \$12/t or less, where the governing unknown factors are the ratio of CO<sub>2</sub> injected to CH<sub>4</sub> produced and the time of breakthrough [Oldenburg et al., 2004a]. The estimated disposal capacity in depleted oil and gas fields amounts to 141 GtC worldwide [Stevens et al. 2000].

The challenge of reducing atmospheric CO<sub>2</sub> concentrations is global in scale, indicating the need for collaboration of research institutes, government agencies, industry, and various advocacy groups. The International Energy Agency, including participants from Australia, Belgium, Canada, Denmark, Finland, France, Germany, Japan, Korea, The Netherlands, New Zealand, Norway, Sweden, Switzerland, United Kingdom, USA, and Venezuela, started the Greenhouse Gas Research and Development Programme in November 1991 [Riemer, 1996], [Freund, 1997]. The collaboration performs evaluations on reducing emissions, capturing and storing of greenhouse gases, as well as the dissemination of the results.

Recently, calls for research in different areas of carbon sequestration, with the ultimate aim to cut down greenhouse gas emissions, have been promoted, e.g., by the U.S. Department of Energy [U.S. Department of Energy, 1999] and by the European Union through the European Union 6th Framework Programme for Research and Development [European Parliament and Council of Europe, 2002]. The latter project provides funding for the European GESTCO project (European Potential for Geological Storage of Carbon Dioxide from Fossil Fuel Combustion), a joint research project conducted by eight national geological surveys [Christensen, 2000]. Furthermore the German Federal Ministry for Economics and Labour established the program COORETEC (CO<sub>2</sub>-Reduction-Technologies) [Geipel et al., 2003a,b].

The concept of carbon sequestration with enhanced gas recovery is of special interest for Germany because

- (i) CO<sub>2</sub> emissions are being regulated in Europe as a way of slowing down the increase in CO<sub>2</sub> concentrations in the atmosphere due to fossil fuel burning. The introduction of ecological tax reforms, e.g., [Welfens et al., 1999], and greenhouse gas emission trading, e.g., [Bode, 2003], which are obligated for German energy industries in 2005 [Geipel et al., 2003b], are embedded in the European climate efforts. They should be extended to a global scale by 2008.
- (ii) With Germany phasing out of nuclear energy, the demand for natural gas will increase, leading to a faster depletion of the gas reservoirs and rising CO<sub>2</sub> emissions. Another consequence

will be the enhanced prominence of the German lignite power plants with twice as much CO<sub>2</sub> emission per unit of energy compared to gas-fired power plants.

- (iii) The total storage capacity of the 66 gas fields of suitable size in Germany is estimated as  $2.56 \times 10^{12}$  kg CO<sub>2</sub> [May et al., 2002]. Many German gas reservoirs are nearing depletion [Pasternak et al., 2001], and besides underground natural gas storage [Sedlacek, 2002], the owners are looking for new beneficial uses of depleting gas reservoirs.
- (iv) Germany is one of the largest global carbon emitters. In 2001, the energy-related carbon emissions amounted to an equivalent of  $818 \times 10^9$  kg CO<sub>2</sub>; i.e., it was sixth after the United States ( $5738 \times 10^9$  kg CO<sub>2</sub>), China ( $3051 \times 10^9$  kg CO<sub>2</sub>), Russia ( $1613 \times 10^9$  kg CO<sub>2</sub>), Japan ( $1159 \times 10^9$  kg CO<sub>2</sub>), and India ( $920 \times 10^9$  kg CO<sub>2</sub>) [U.S. Department of Energy, 2003].
- (v) As a highly industrialized country, with only relatively modest natural resources, Germany is dependent on the development and realization of innovative, advanced technologies.

This report summarizes our studies of CO<sub>2</sub> sequestration in an almost depleted gas reservoir involving enhanced gas recovery (EGR) in the Altmark, North Germany. This work was carried out as a cooperation between the Federal Institute for Geosciences and Natural Resources (Bundesanstalt für Geowissenschaften und Rohstoffe, BGR, Hannover, Germany) and the Ernest Orlando Lawrence Berkeley National Laboratory (LBNL, Berkeley, U.S.). As such, this work is embedded in the GESTCO project.

### 3 Method

Numerical simulation has been used widely for studies of geological CO<sub>2</sub> sequestration in different geological settings, e.g., [Obdam et al., 2002]. The simulation approach is needed because these processes have rarely ever been tested or implemented in the field. In this study numerical simulations are performed using the general-purpose numerical simulation program TOUGH2. This simulator belongs to the MULKOM family of codes, developed at the Earth Sciences Division/LBNL, and is based on the integral finite difference method [Pruess et al., 1999]. TOUGH2 is a multi-dimensional simulator for modelling multi-component multiphase flow and heat flow in porous and fractured media. It considers fluid flow in liquid and gaseous phases, and the transitions between the phases, occurring under pressure, viscous, and gravity forces according to Darcy's law.

Equation of state modules (EOS) in TOUGH2 describe temperature, pressure, and volume for a given substance or mixture of substances. They provide the thermophysical properties of fluid mixtures, which are needed for the mass and energy balance equations. For the following simulations the research version for gas reservoirs called EOS7C was chosen [Oldenburg et al., 2004b], which is based on the modules EOS7 and EOS7R [Pruess et al., 1999]. EOS7C considers heat and the five mass components water, brine, CO<sub>2</sub>, tracer, and CH<sub>4</sub>. Real gas mixture properties are modeled, like densities and enthalpy within the range of relevant pressures and temperatures using a modification of the van der Waals' equation, known as the Peng-Robinson equation of state [Peng and Robinson, 1976]; [Reid et al., 1987].

## 4 Altmark Gas Reservoir

The natural gas reservoirs of the Altmark region ( $52.8^{\circ}\text{N}, 11.0^{\circ}\text{E}$ ) are situated in the Federal State Sachsen-Anhalt, in North Germany, and lie about halfway between Hannover and Berlin (see Figure 1). The area belongs to the North German Basin, which forms part of the Mid-European Basin. (For more background information, especially about the evolution of the basin, see e.g., [Plein, 1993], [Scheck and Bayer, 1999], [Kossow, 2001].) The gas-bearing layers were generated in the early Permian (Rotliegend). The Altmark reservoirs consists of nine subreservoirs (see Figure 2). They are now owned by Erdgas Erdöl GmbH (EEG) belonging to Gaz de France Deutschland GmbH.

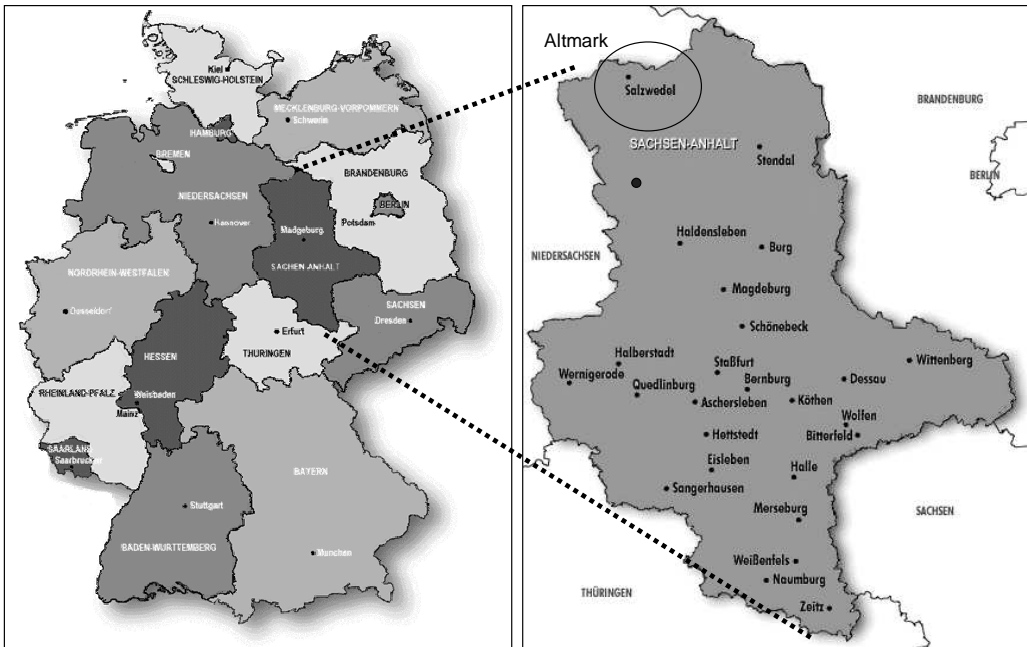


*Figure 1: The Altmark region is located in the German Federal State Sachsen-Anhalt close to the border to Niedersachsen.*

An overview of the characteristics of the Altmark reservoir is given in Table 1. There are nine subreservoirs. The main subreservoir of the Altmark is Salzwedel-Peckensen, which is also the most important gas field in Germany. The initial gas in place (IGIP) is estimated to be up to  $265 \times 10^9 \text{ m}^3$  (9 Tcf), hence it is one of the biggest gas reservoirs in Europe. Since the discovery of the field in 1968, 70 % of the natural gas has already been produced [Stottmeister, 1999]. Annual production peaked in 1984 through 1987, at  $12 \times 10^9 \text{ m}^3$  (424 Bcf). Within the last years, the production rate decreased to  $1.7 \times 10^9 \text{ m}^3$  (25 Bcf) (see Figure 3, [Pasternak et al., 2001]). Most likely, the entire reservoir will be depleted by the year 2020. Subsections may be available for CO<sub>2</sub> injection earlier.

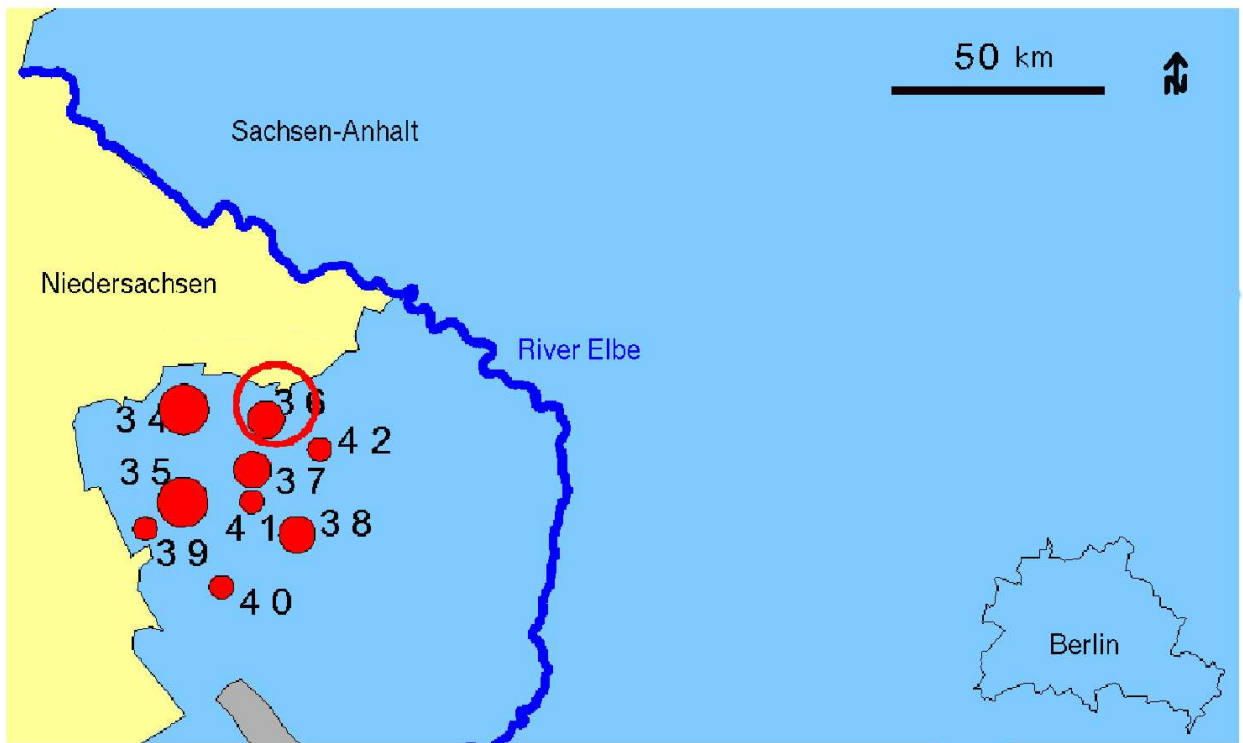


Figure 2: The natural gas reservoirs of the Altmark are located in the North German Basin, in the German Federal State Sachsen-Anhalt close to the border to Niedersachsen, about 150 km west of Berlin. There are nine subreservoirs as numbered in the diagram: 34 Salzwedel-Peckensen, 35 Heidberg-Mellin, 36 Riebau, 37 AltenSalzwedel, 38 Winkelstedt, 39 Mellin-Süd, 40 Wenze, 41 Zehtlingen, 42 Sanne. Map modified from [Wagner et al., 1998].

The Altmark reservoir is a compartmentalized anticlinal structure, divided by numerous faults of different sizes (Figure 4). The orientation of the horizontal principal stress is NW-SE. The reservoir extends laterally 35 km × 40 km, with vertical extent of more than 200 m. The reservoir is mainly sandstone and siltstone in varying percentages, with minor portions of clay (see Table 2).

As a first approximation, this variety in material sequences leads to the definition of 10 units, considered homogeneous in the lateral direction. For the Eldena Basissandstein (refer to Table 2), the measured dip ranges from  $0.2^\circ$  to  $0.6^\circ$ , with an average of  $0.3^\circ$  [Stoll, 1981], meaning the dip of the reservoir can be neglected. A compilation of the main parameters of the subreservoir Salzwedel-Peckensen given in published sources is listed in Table 1. The lithologic data are based on the structure described for the Saxon of the Western Altmark [Stoll, 1981], and the synopsis of the Rotliegend in the western part of the north-east German depression, including the Western and the Eastern Altmark [Kleditzsch, 2003].

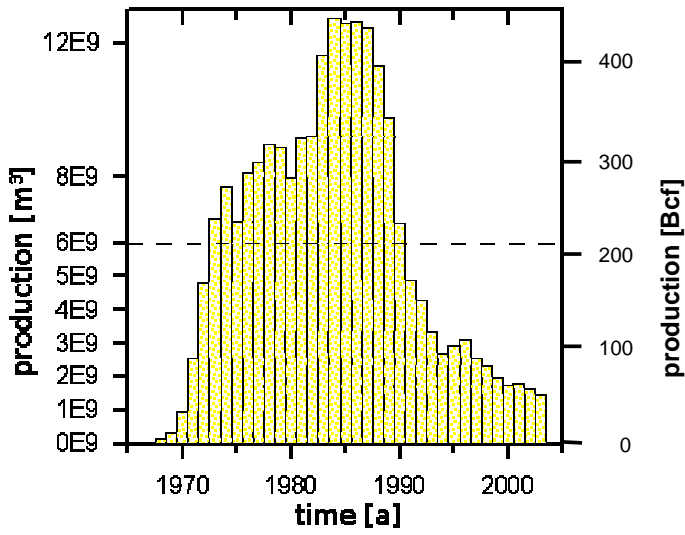


Figure 3: The production history of the natural gas fields of the Altmark between 1968 and 2003 show the declining gas production since 1987 (see e.g., [Pasternak et al., 2001]). The horizontal dashed line indicates the average annual gas production of about  $6 \times 10^9 \text{ m}^3$  (210 Bcf).

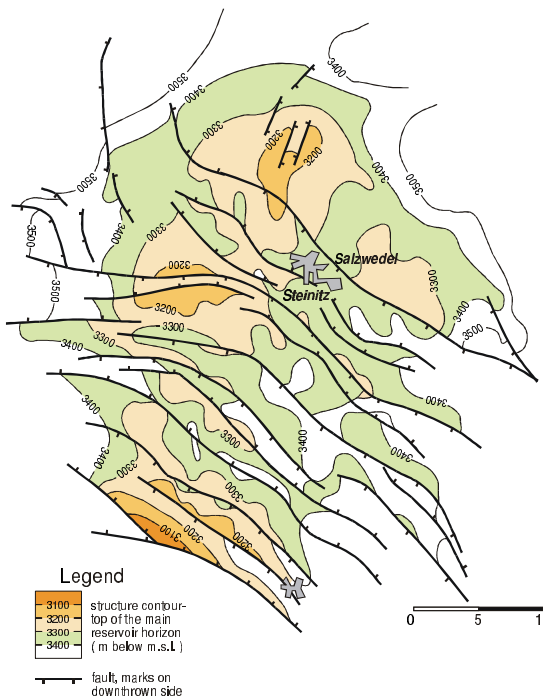


Figure 4: The map of the Altmark region with the town Salzwedel depicts the structure contours on top of the main reservoir horizon in the Rotliegend and the mainly NW-SE oriented faults [Krull, 2003].

*Table 1: Characteristics of the Altmark reservoir.*

		Reference
region	Altmark, North Germany	—
reservoir	Altmark	—
subreservoir	Salzwedel-Peckensen	—
size	30 km × 40 km	—
owner	Erdöl Erdgas GmbH	—
reservoir type	natural gas reservoir	—
gas initially in place	$265 \times 10^9 \text{ m}^3$	[Wendel et al., 2004]
gas production since	1968	[Stottmeister et al., 1999]
gas already produced	> 70 %	[Wendel et al., 2004]
number of production wells still in use (year 2001)	93	[Pasternak et al., 2001]
depth of top of gas bearing layers	3135 m	[Stottmeister et al., 1999]
depth of gas water contact	3442 m	[Stottmeister et al., 1999]
dip of layer <sup>(1)</sup>	< 1 °	[Stoll, 1981]
pH-value	6.0	[Brasser et al., 2001]
Na-Ca-Mg, Ca-Na-Mg, Na-Mg-Ca layer water	357 g/l	[Brasser et al., 2001]
temperature	115 °C – 130 °C	[Stottmeister et al., 1999]
vertical temperature gradient	34 °C/1000 m	[Clauser et al., 2002]
radiogenic heat production	$2.2 - 2.6 \mu \text{W/m}^3$	[Hoth et al., 1998]
pressure in the production zones	4.5 – 22 MPa	[Khoklov, 2004]
usable porosity	8 %	[Schumacher and May, 1990]
permeability	10 – 100 mD	[Stoll, 1981]

(1) for the Eldena Basissandstein, located below the water contact

The gas bearing layers in North Germany were generated in the lower Permian, between 225 – 285 million years BP. These layers of the Rotliegend are located at depths of about 3000 m, above Permo-Carboniferous volcanic rocks and Carboniferous sediments. They are covered by the Zechstein, a massive salt rock several hundreds of meters high. It forms the upper division of the Permian (Dyas) of Europe. The process of subsidence with time is shown for the well Boizenburg, located about 60 km north-northwest of Salzwedel (Figure 5). The Zechstein salt is virtually impermeable compared to other rocks, hence an effective barrier for fluid migration, and serves as an effective cap rock. The lithology and lithostratigraphy of the gas-bearing sequences in the Altmark are listed in Table 2.

The natural gas in the Altmark is predominantly nitrogen ( $\text{N}_2$ ). In Salzwedel-Peckensen nitrogen amounts to 40 % to 80 % of the natural gas [Stottmeister et al., 1999], see Table 3. The methane content lies between 8 % and 60 %, with an average of 32 %. Methane and deep-seated nitrogen are supposed to have migrated from carboniferous rocks [Schumacher and May, 1990]. Carboniferous shales may have made a significant contribution as a source of high nitrogen content, but this topic is still controversial [Hoth et al., 2003].

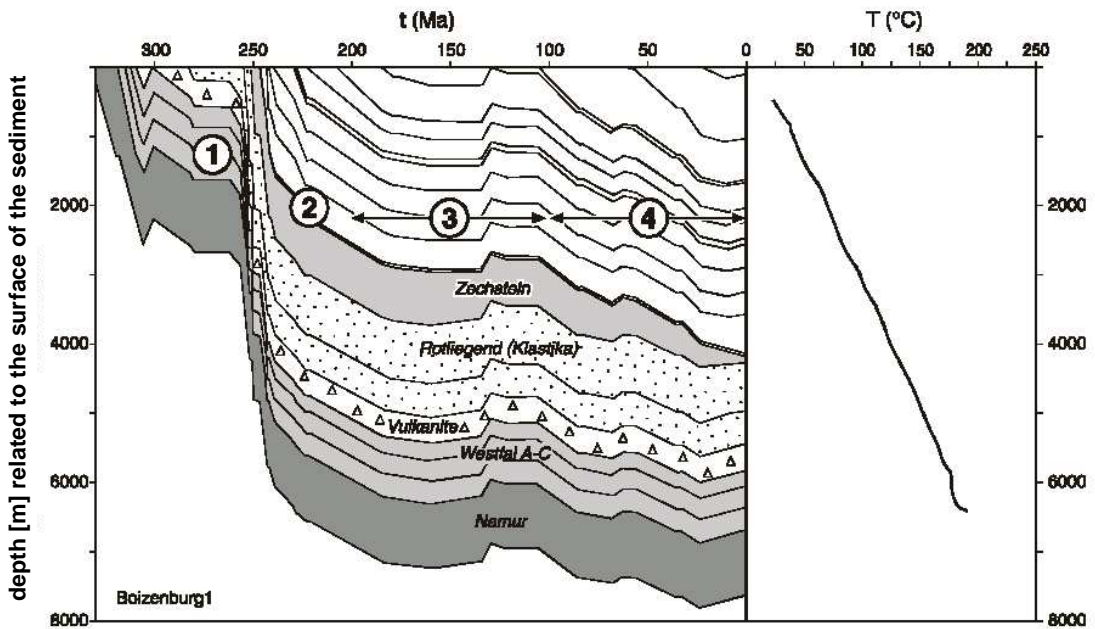


Figure 5: Subsidence in time based on data from the well Boizenburg, modified from [Hoth et al., 1998].

At present, the pressure in the undisturbed reservoir compartments amounts to 42.5 MPa [May, 2002]. During the production, the pressure evolved differently due to inhomogeneity between the layers and varies now between 4.5 MPa and 22 MPa [Khoklov, 2004]. The temperature ranges from 115 °C to 130 °C [Stottmeister et al., 1999]. Water infiltrates from the edges, but mainly from the bottom into the initially gas-saturated layers.

## 5 Requirements for Sequestration of Carbon Dioxide

The long- and short-term requirements of carbon dioxide sequestration include safety for humans and the environment, predictability based on simulations and case studies, verifiability based on measurements, and last but not least, affordability. Various studies have been published on a broad range of aspects, e.g., environmental impacts [Johnston and Santillo, 2002], safety [Jimenez and Chalaturnyk, 2002], injection strategies [Clemens and Wit, 2001], monitoring [Benson and Myer, 2002], gas leakage [Oldenburg and Unger, 2003], fluid leakage [Pruess, 2003], and economic feasibility [Clemens and Wit, 2001; Oldenburg et al., 2004a].

*Table 2: Characteristics of the gas bearing sequences in the Western Altmark, after [Stoll, 1981].*

Sequence	Lithology	Lithostratigraphy	Thickness [m]	Usable Porosity [%]	Abbreviation
Zyklus 17	silt	Mellin <sup>(1)</sup> Wechselfolge <sup>(2)</sup>	42	8	Zyk17
Zyklus 16	silt	Mellin Basisfolge <sup>(3)</sup>	30	5	Zyk16
Zyklus 15	silt	Mellin Wechselfolge	28	5	Zyk15
Zyklus 14	sand	Wechselfolge der oberen <sup>(4)</sup> Peckensen Schichten <sup>(5)</sup>	17	14	Zyk14
Zyklus 13	sand	Basissandstein <sup>(6)</sup> der oberen Pecken- sen Schichten	12	15	Zyk13
Zyklus 12	clay	Wechselfolge der unteren <sup>(7)</sup> Pecken- sen Schichten	25	5	Zyk12
Zyklus 9–11	silt	Mellin Wechselfolge	43.5	8	Z9–11
Zyklus 8	sand	Sandsteinfolge <sup>(8)</sup> der unteren Pecken- sen Schichten	22	15	Zyk08
Zyklus 7	sand	Eldena-Wechselfolge <sup>(9)</sup>	16	5	Zyk07
Zyklus 1–6	sand	Eldena-Basissandstein	90	5	zy1–6

(1) Mellin = municipality in the Altmark

(2) Wechselfolge = alternating series

(3) Basisfolge = base series

(4) ober- = upper-

(5) Schichten = stratum

(6) Basissandstein = base sandstone

(7) unter- = lower-

(8) Sandsteinfolge = sandstone series

(9) Eldena = municipality in Mecklenburg-Vorpommern

*Table 3: The main components of the dry natural gas in the Salzwedel-Peckensen reservoir [Müller et al., 1993].*

Gas component		vol.%
nitrogen	N <sub>2</sub>	40 % – 90 %
methane	CH <sub>4</sub> CH <sub>4</sub> average	8 % – 60 % 32 %
carbon dioxide	CO <sub>2</sub>	< 1 %
ethane	C <sub>2</sub> H <sub>6</sub>	< 1 %

In detail, the general requirements of the geologic settings for CO<sub>2</sub> sequestration in gas reservoirs are

- (1) A broad and adequate survey of the potential sequestration site with objective evaluation should be implemented.
- (2) Reservoir layers with adequate porosities and permeabilities should exist and be accessible.

- (3) In order to avoid CO<sub>2</sub> leakage, there is a need for a confining overlying layer with a low permeability, which seals the gas disposal region. No faults should be present to connect the reservoir and the ground surface. A permanent seal of wells in the area should be ensured.
- (4) An adequate storage capacity for the injected CO<sub>2</sub> should exist.
- (5) It is recommended that the recovery of natural gas in the reservoir should be close to the end.
- (6) The injection into the reservoir should be at adequate depths. The upper limit is dependent on the small compressibility of liquid-like supercritical CO<sub>2</sub> beyond the critical point of CO<sub>2</sub> at 31 °C, 7.4 MPa, see Figure 6. Hence the upper depth is determined by local gradients of temperature and pressure. The lower depth is limited by economics to excessive costs for drilling and pressurizing of CO<sub>2</sub>.
- (7) It is beneficial if a source of CO<sub>2</sub> is located nearby to the CSEGR site, e.g., a power plant with integrated CO<sub>2</sub> capture.
- (8) An already existing infrastructure, with, among other things, gas transportation pipelines, is advantageous.

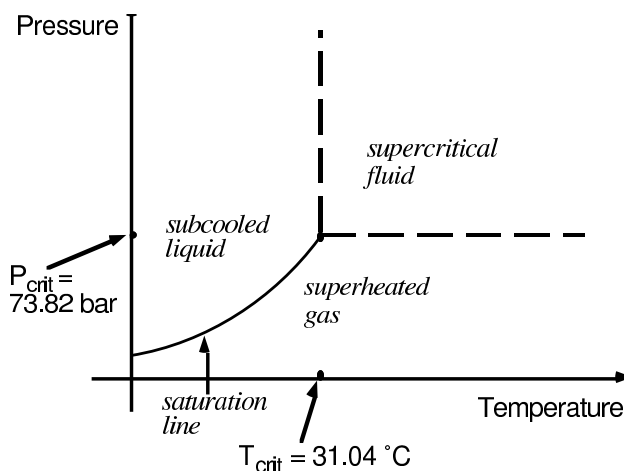


Figure 6: Phase diagram for CO<sub>2</sub> [Pruess, 2004].

Concerning these items, the special conditions in Salzwedel-Peckensen fulfill the requirements stated above:

- (re 1) More than 400 wells were drilled into the Rotliegend of the Altmark, providing a detailed understanding of the site.
- (re 2) Average usable porosities in the sand formation amount to 8 %, in the Western Altmark [Schumacher and May, 1990], permeabilities range from 10 mD to 100 mD.
- (re 3) Above the gas bearing sequences lies the several hundred meter thick Zechstein formation in depths above 3135 m, showing a low permeability and serving as a cap rock.

- (re 4) The total height of the sand/siltstone layers amounts to 226 m. Salzwedel-Peckensen is the largest natural gas field in Germany.
- (re 5) In the early nineties of the last century, 70 % of the gas in place was already produced. It is estimated that natural gas production will stop within the next 10 — 15 a.
- (re 6) The gas bearing layers span the depths of 3135 — 3442 m, which is deeper than the required optimal storage range of 1200 m to 1500 m in the North German Basin [May et al. 2003], see Figure 7.
- (re 7) The lignite power plant Schwarze Pumpe, with  $2 \times 800$  MW, is situated in the Lausitz, 300 km SE of the Altmark. [Vattenfall Europe AG, 2005]. Other options exist in the use of waste gas of a nearby industrial power station owned by Erdgas Erdöl GmbH or a fertilizer factory.
- (re 8) The existing infrastructure, like wells, gas transportation pipelines, etc. is available and in good condition.

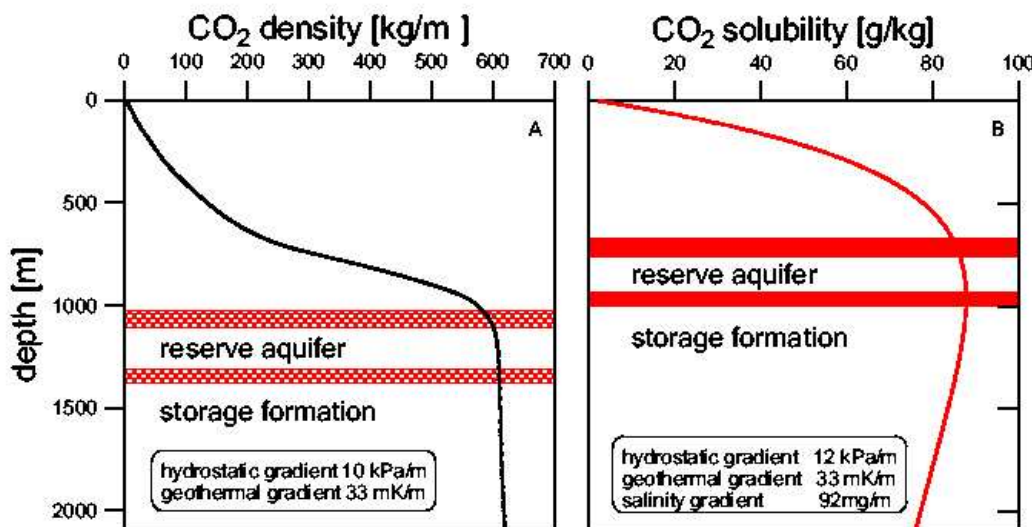


Figure 7: Using gradients typical for the North German Basin, the depth-dependent variation of  $\text{CO}_2$  density and solubility in saline formation water determines the optimal  $\text{CO}_2$  storage range below permeable seals (left diagram, A) and impermeable seals (right diagram, B) [May et al., 2003].

## 6 Gas Mixture Properties

In order to define numerical models for  $\text{CO}_2$  injection into gas fields, it is necessary to examine the potential gas mixtures after injection. Only the main gas components  $\text{CH}_4$  and  $\text{N}_2$  are considered (see Table 3). With the injected  $\text{CO}_2$ , this results in a ternary gas system. As EOS7C handles only  $\text{CH}_4$  and  $\text{CO}_2$ , the question arises whether it is sufficient to reduce the problem further to a

two-gas mixture simulation. Therefore gas mixtures composed of the three gases CH<sub>4</sub>, N<sub>2</sub>, CO<sub>2</sub> are evaluated to specify the gas compressibility-factor  $Z$ , density  $\rho$ , and viscosity  $\mu$ . The compressibility factor,  $Z$ , is defined in terms of the real gas law as

$$pV = Z n R T ,$$

where

$p$	=	pressure [Pa]
$V$	=	volume [m <sup>3</sup> ]
$n$	=	number of moles [mol]
$R$	=	real gas constant, 8.314 $\frac{\text{J}}{\text{mol K}}$
$T$	=	temperature [K].
$Z$	=	compressibility factor [ ].

Calculations were performed using the same Peng-Robinson equation of state implemented in EOS7C [Oldenburg et al, 2004b], but with consideration of N<sub>2</sub> along with CO<sub>2</sub> and CH<sub>4</sub>. All calculations were performed for gas mixtures with 1% difference in gas composition, leading to 5151 data points in total for one set of initial conditions. As mentioned in Section 4, Table 1, the pressure in the Altmark gas reservoir ranges from 4.5 MPa to 22 MPa. The field temperature ranges from 115 °C to 130 °C. Hence the calculations were executed for four different pressure values,  $p$  (5 MPa, 10 MPa, 15 MPa, and 20 MPa) at a constant temperature  $T$  of 125 °C (398 K). The results are plotted in triangular diagrams (see Figures 16 to 21), where each triangle vertex represents one of the three pure gases. The gas properties  $\rho$ ,  $\mu$ , and  $Z$  for the varying CH<sub>4</sub>-N<sub>2</sub>-CO<sub>2</sub> systems are indicated through the contour colors. Compositions are given in mass fraction. For the labeling of the axes see Figure 8.

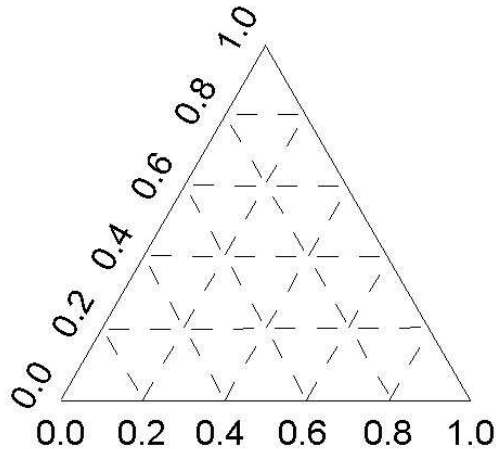


Figure 8: Labeling of the axes in the triangular diagrams in Figures 9, 10, and 16 to 21.

A schematic illustration of possible parameter distributions in CH<sub>4</sub>-N<sub>2</sub>-CO<sub>2</sub> systems is given in Figure 9. This figure shows that for the extreme case in which a property is independent of the CO<sub>2</sub>-CH<sub>4</sub> fraction, i. e., as in the first triangle, a N<sub>2</sub>-free gas model would be entirely inappropriate.

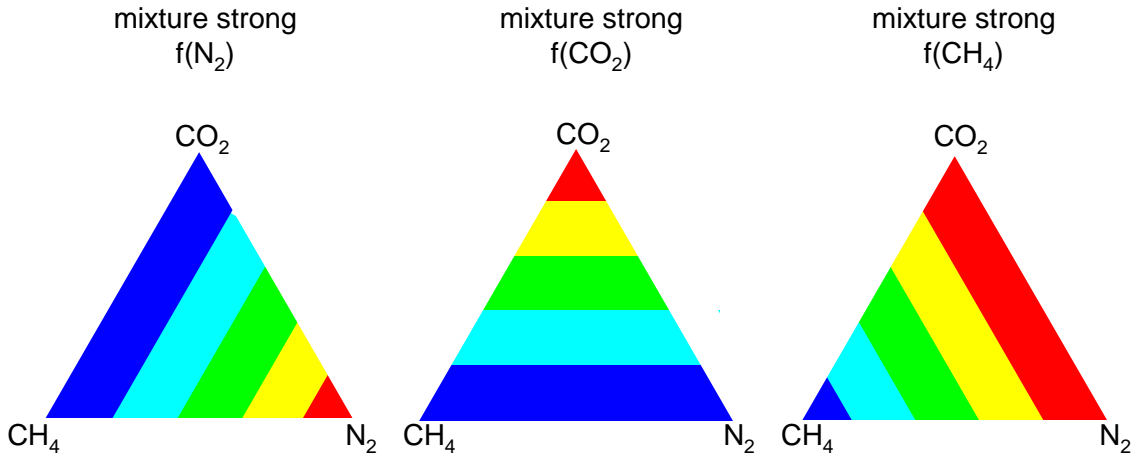


Figure 9: Schematic illustration of end-member property distributions in  $\text{CH}_4\text{-N}_2\text{-CO}_2$  systems. In the first triangle, a  $\text{N}_2$ -free model is not good. In the second and third triangles a  $\text{N}_2$ -free model gives a good approximation to the three-component real system.

For the case in which either there is no variation in property along the  $\text{CH}_4\text{-N}_2$  side or  $\text{CO}_2\text{-N}_2$  side, a  $\text{N}_2$ -free model is a reasonable approximation to the three-component system. It will be seen below that  $\text{CO}_2$  has a strong effect on compressibility factor, density, and viscosity in  $\text{CH}_4\text{-N}_2\text{-CO}_2$  mixtures. Therefore the three-component mixture can be reasonably approximated by the two-component system  $\text{CO}_2\text{-CH}_4$ . The main area of interest in the triangular diagrams is the one which represents the conditions of the Altmark gas, which is 8 % — 60 %  $\text{CH}_4$ , 40 % — 90 %  $\text{N}_2$ , i.e., the area with the  $\text{CH}_4:\text{N}_2$  ratios 1:9 to 6:4 with different amounts of  $\text{CO}_2$  (see Figure 10). This region should be compared with the side line connecting  $\text{CH}_4$  [100 %] with  $\text{CO}_2$  [100 %], representing the  $\text{CH}_4\text{-CO}_2$  system.

## 6.1 Compressibility factor

The compressibility-factor  $Z$  is calculated using the relationship in the real gas law. Figures 16 and 17 display  $Z$  as a function of composition in the  $\text{CH}_4\text{-N}_2\text{-CO}_2$  gas mixture. As expected,  $Z$  decreases at higher pressure. The  $\text{CH}_4$ ,  $\text{N}_2$ ,  $\text{CO}_2$  mixtures with a higher amount of  $\text{N}_2$  reveal higher  $Z$  values, while for those with a higher  $\text{CO}_2$  portion,  $Z$  is relatively smaller. This is valid for the whole pressure range presented. The  $Z$  range covers 0.9 to 1 for 5 MPa and 0.72 to 1.1 for 20 MPa, respectively. Gas systems only composed of  $\text{CH}_4$  and  $\text{CO}_2$  have compressibility-factors of 0.97 to 0.9 (5 MPa) and 0.97 to 0.72 (20 MPa). The average Altmark gas shows  $Z$  values of 0.9 to 1 for (5 MPa) and 0.72 to 1.1 (20 MPa).

The implications for the Altmark gas reservoir, derived from the study of the compressibility factor, are that gas mixtures higher in  $\text{CO}_2$  will be more compressible. Furthermore, the  $Z$ -factor for  $\text{CH}_4$  is nearly one and is a weak function of pressure above 10 MPa. The  $Z$ -factor of  $\text{N}_2$  is approximately one for all pressures modeled. For this study the differences between the ternary system and the  $\text{CH}_4\text{-CO}_2$  system are small enough.

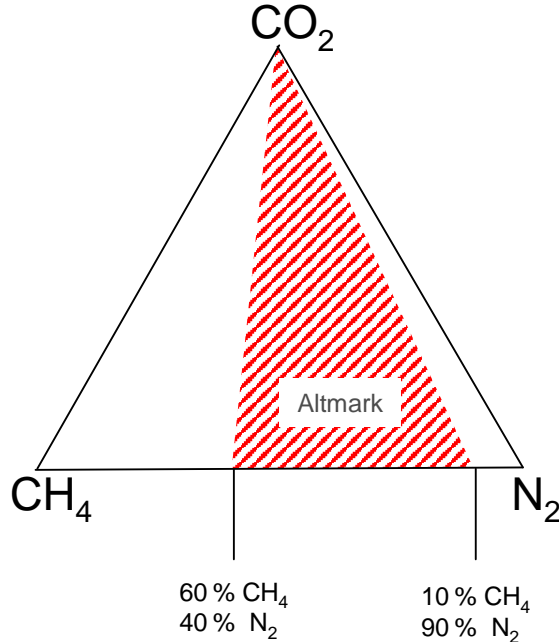


Figure 10: The main area of interest in the triangular diagram of a  $CH_4$ - $N_2$ - $CO_2$  system is the hatched area, which represents the conditions of the Altmark gas, which is 8% — 60%  $CH_4$ , 40% — 90%  $N_2$ .

## 6.2 Density

The density for gas mixtures is obtained with

$$\rho = \frac{p m_w}{Z R T} ,$$

whereas

- $m_w \hat{=}$  molecular weight of the mixture, equal to  $\sum_i x_i m_{w i}$
- $m_{w i} \hat{=}$  molecular weight of the mixture component  $i$
- $x_i \hat{=}$  mole fraction of the component  $i$ .

The molecular weights ( $kg \times mol^{-1}$ ) of interest are

- 0.01604 for  $CH_4$
- 0.02809 for  $N_2$
- 0.04401 for  $CO_2$ .

Figures 18 and 19 illustrate the density values for varying mixtures, at four different pressures. The density  $\rho$  of a gas mixture with  $CH_4$  increases with addition of  $N_2$  (see Figure 18). It rises relatively faster with an addition of  $CO_2$ . The density of pure  $CH_4$ , compared to  $CO_2$ , shows a direct pressure dependency. For the four pressure cases, density in the Altmark gas system increases

from about  $50 \text{ kg/m}^3$  (50 MPa) to  $260 \text{ kg/m}^3$  (20 MPa). Comparing these results of the CH<sub>4</sub>-CO<sub>2</sub> system with the CH<sub>4</sub>-N<sub>2</sub>-CO<sub>2</sub> system, the variation of density due to pressure is smaller, about  $20 \text{ kg/m}^3$  (50 MPa) to  $65 \text{ kg/m}^3$  (20 MPa) (see Figure 19).

The absolute values of density at 50 MPa range roughly from  $25 \text{ kg/m}^3$  to  $75 \text{ kg/m}^3$  in the ternary system,  $35 \text{ kg/m}^3$  to  $50 \text{ kg/m}^3$  in the Altmark gas system, and  $30 \text{ kg/m}^3$  to  $60 \text{ kg/m}^3$  in the CH<sub>4</sub>-CO<sub>2</sub> system. At 20 MPa, the density can be estimated as  $100 \text{ kg/m}^3$  to  $360 \text{ kg/m}^3$  for the ternary system,  $126 \text{ kg/m}^3$  to  $191 \text{ kg/m}^3$  in the Altmark gas system, and  $120 \text{ kg/m}^3$  to  $230 \text{ kg/m}^3$  in the CH<sub>4</sub>-CO<sub>2</sub> system.

Hence it can be stated that (i) the differences between the ternary system and the simpler CH<sub>4</sub>-CO<sub>2</sub> system are not big, as far as density is concerned, (ii) the density implications for CO<sub>2</sub> storage are that mixed gas decreases the density of CO<sub>2</sub> mixtures, therefore decreasing total potential CO<sub>2</sub> storage mass per reservoir volume.

### 6.3 Viscosity

The gas viscosity  $\mu$  of the fluid mixture is empirically correlated as a function of density and temperature [Chung et al, 1988]. The viscosities for CH<sub>4</sub>-N<sub>2</sub>-CO<sub>2</sub> gas systems at four different pressures are depicted in Figures 20 and 21. The viscosity increases with pressure. For gas systems with different amounts of CH<sub>4</sub>, N<sub>2</sub>, and CO<sub>2</sub>, mixtures with a higher content of CH<sub>4</sub> have the lowest viscosities, ranging from about  $1.5 \times 10^{-5} \text{ Pas}$  at 5 MPa to  $1.9 \times 10^{-5} \text{ Pas}$  at 20 MPa for pure methane. Ternary systems high in N<sub>2</sub> show a viscosity of  $2.2 \times 10^{-5} \text{ Pas}$  at 5 MPa, for those high in CO<sub>2</sub> reach  $2.1 \times 10^{-5} \text{ Pas}$  at 20 MPa. At pressures of 20 MPa, viscosity of CH<sub>4</sub>-CO<sub>2</sub> mixtures are a weak function of N<sub>2</sub> content. At lower pressures, viscosity of CH<sub>4</sub> mixtures is affected by CO<sub>2</sub> and N<sub>2</sub> almost equally.

Pure CH<sub>4</sub> undergoes the smallest change in viscosity from  $1.5 \times 10^{-5} \text{ Pas}$  (5 MPa) to  $1.9 \times 10^{-5} \text{ Pas}$  (20 MPa). The highest pressure-dependent viscosity is obtained for gas mixtures high in CO<sub>2</sub>. Pure carbon dioxide changes from about  $2.1 \times 10^{-5} \text{ Pas}$  (5 MPa) to  $3.4 \times 10^{-5} \text{ Pas}$  (20 MPa). Viscosity in the two-gas system CH<sub>4</sub>-CO<sub>2</sub> ranges from  $1.5 \times 10^{-5} \text{ Pas}$  to  $2.07 \times 10^{-5} \text{ Pas}$  (5 MPa), and  $1.9 \times 10^{-5} \text{ Pas}$  to  $3.4 \times 10^{-5} \text{ Pas}$  (20 MPa). Viscosity for the range of gas mixtures approximating the average natural gas in the Altmark is smaller, about  $1.93 \times 10^{-5} \text{ Pas}$  to  $2.18 \times 10^{-5} \text{ Pas}$  (5 MPa), and  $2.35 \times 10^{-5} \text{ Pas}$  to  $2.75 \times 10^{-5} \text{ Pas}$  (20 MPa).

The viscosity calculations for the Altmark gas reservoir imply that gas mixtures high in CO<sub>2</sub> content at pressures above 10 MPa will have a smaller mobility due to their higher viscosity. In general, the properties of gas mixtures in the CH<sub>4</sub>-N<sub>2</sub>-CO<sub>2</sub> system are most strongly affected by CO<sub>2</sub> in the pressure and temperature ranges of interest. Although our use of a CH<sub>4</sub>-CO<sub>2</sub> system is an approximation of the actual CH<sub>4</sub>-N<sub>2</sub>-CO<sub>2</sub> system that would be present at Altmark under a CSEGR scenario, the differences in gas mixture properties as shown here are not expected to strongly affect the results of our preliminary studies of CSEGR feasibility

## 7 Development of the Hydrostratigraphic Model

The gas reservoir Salzwedel-Peckensen is a large well field, with a long record of production. In 2001, there were 93 active wells. Existing wells will be used as CH<sub>4</sub> production, CO<sub>2</sub> injection, and monitoring sites in our CSEGR scenario. We assume the wells are regularly distributed in the field a few km apart (see the map in Figure 11). Due to this, the wells can be assumed to represent an approximate five-spot configuration (see Figure 12), requiring a 3D grid. Equal subareas of 4.4 km<sup>2</sup> will be assumed in the model, correspondong to well spacings of about 2.1 km.

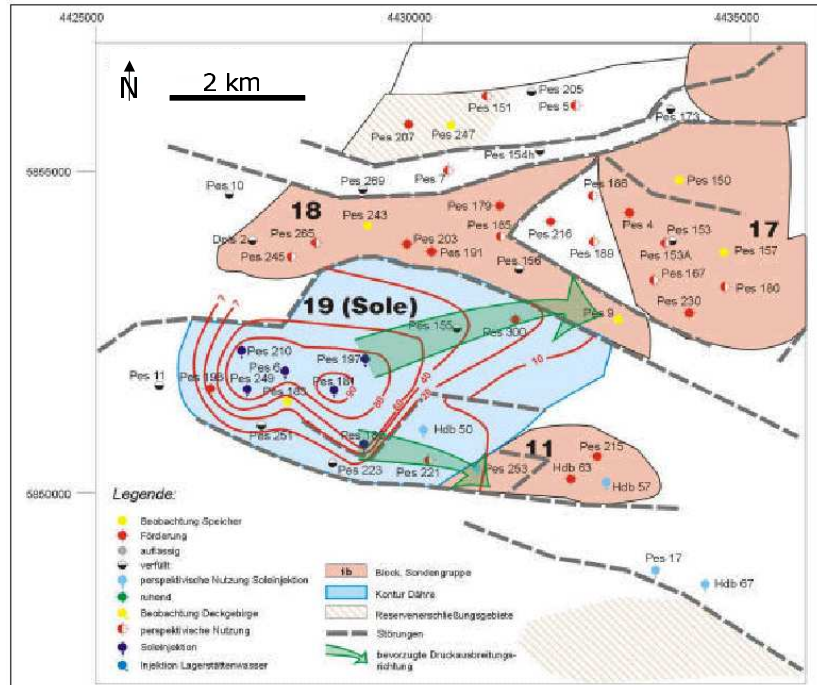


Figure 11: The natural gas reservoir Peckensen shows a dense distribution of wells [Ribbeck, 2001].

Exploiting symmetry, only one quarter of the five-spot configuration, the hatched area in Figure 12, needs to be simulated. The xy-grid consists of 15 × 15 gridblocks, with a width of the inner gridblocks of 150 m, amounting to a horizontal area of 2.1 km × 2.1 km. The main characteristics used in the 3D model are listed in Table 4.

The horizontal layering represents the lateral continuity of the sequences. The dip of the layers can be neglected. This leads to the generation of a strongly generalized geological layer model of the Altmark reservoirs [Rebscher and May, 2004]. Similar layers were combined to obtain practical numbers of gridblocks for the 3D simulation. Following the formations given in the literature based on well logs, the vertical zoning can be presented by nine units using six different rock types (see Section 4, Table 2).

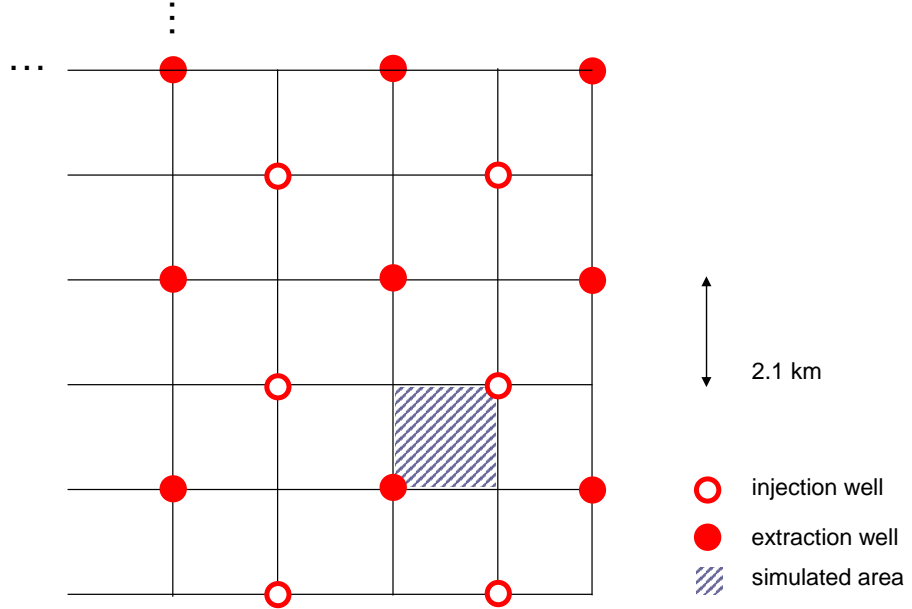


Figure 12: Schematic of five-spot configuration showing plan view of model domain.

Table 4: The main characteristics used in the 3D model (derived from properties in Table 1).

Model parameter	Value
model type	five-spot configuration
model area	2.1 km × 2.1 km
reservoir height	226 m
reservoir depth	3000 m
dip of layers	0°
temperature	120 °C, constant
pressure	hydrostatic distribution
pressure at the bottom	20 MPa
duration of CO <sub>2</sub> injection phase	40 years
total CO <sub>2</sub> injection when using 10 wells	4.2 × 10 <sup>11</sup> kg CO <sub>2</sub>
CO <sub>2</sub> injection rate at one sink site <sup>(1)</sup>	8 kg/s
geometry of source	vertical column
duration of CH <sub>4</sub> extraction	40 years, simultaneous to CO <sub>2</sub> injection
geometry of sink	vertical column

(1) The injection rate is varied in section 10. For the same amount on total CO<sub>2</sub> injection, an injection rate of 3 kg/s corresponds to 27 injection and extraction sites each.

Each of the geologic layers is represented by two identical grid layers in the model, only the pressure values are hydrostatically adjusted depending on their vertical position. Hence using nine geologic layers and 15 gridblocks both in x- and y-directions leads to  $15 \times 15 \times 9 \times 2 = 4050$  gridblocks in total (see Figure 13). In the vertical, the closed compartment extends to 226 m. For closeness to reality, the parameter values are chosen based on measured published sources (Section 4).

As no detailed, confidential industry data are used, the described model should be regarded more as a generic tool than a model for specific reservoir prediction. It is suitable for general application to gas reservoirs composed of layers with a range of permeabilities, and is particularly useful for sites in the North German Basin.

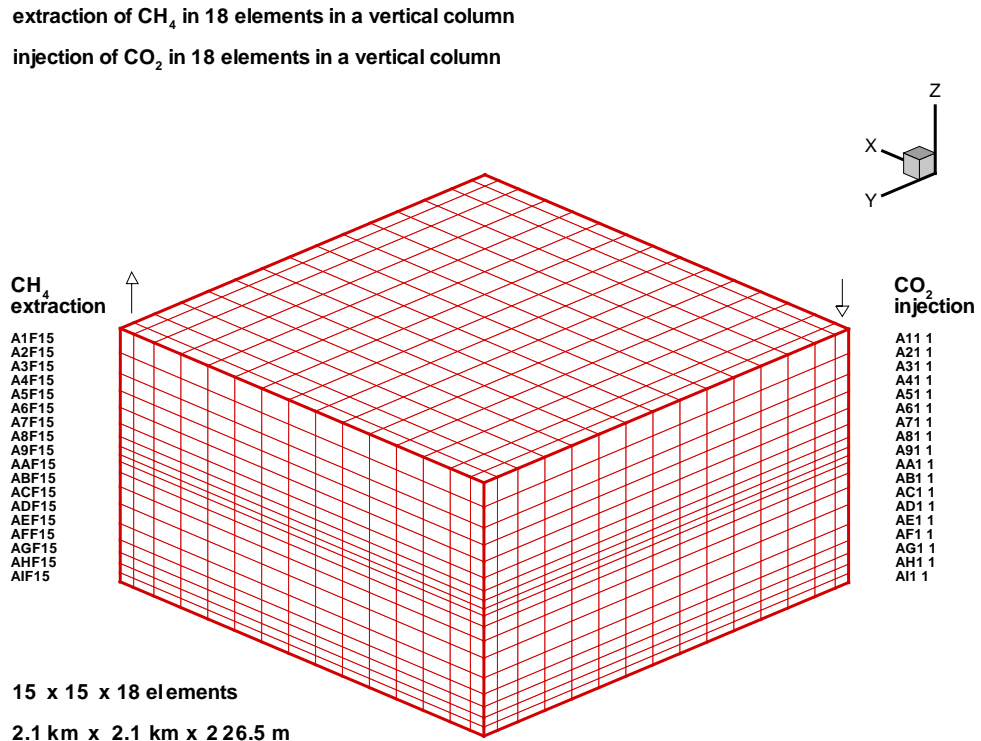


Figure 13: The 3D mesh is discretized in xyz into  $15 \times 15 \times 18$  gridblocks. The horizontal sizes of the gridblocks at the edge are adjusted to the conditions of a five-spot configuration. Injection and extraction sites are located in opposite corners.

## 8 Two-dimensional Simulation

In order to test the model for the three dimensional case, two-dimensional horizontal scenarios were simulated first. As described above, the discretization of the xy-grid consists of  $15 \times 15$  gridblocks, covering an area of  $4.4 \text{ km}^2$ . The height of one gridblock is 14 m, approximately the average size of a gridblock in the 3D simulations, and exactly the size of a gridblock of layer Zyklus 15 (Table 2). At the beginning the reservoir layers are assumed to be filled with a homogeneous gas mixture. In the Salzwedel-Peckensen reservoir the main components are  $\text{CH}_4$  and  $\text{N}_2$  (see Table 3). Following the results of Section 6, we neglect  $\text{N}_2$  and assume a binary  $\text{CH}_4\text{-CO}_2$  gas mixture. At the beginning no  $\text{CO}_2$  is present in the reservoir. As the water contact lies below the study area, it is assumed that gases are not dissolved in water.

The CO<sub>2</sub> injection well is located in one corner gridblock, the origin of the xy-plane, i.e., in the lower left corner (see Figure 14). The opposing corner gridblock, in the upper right, represents the extraction site for which constant conditions (Dirichlet condition) are set. In order to leave the thermodynamic parameters unchanged by mass exchange, the extraction gridblock is assigned a virtual volume size of about 10<sup>50</sup> m<sup>3</sup>, functioning as a constant-pressure sink for whatever gas arrives there. The downhole pressure at the production well is 20 MPa.

Due to the given lateral homogeneity of the reservoir, the rock properties in each model layer are assumed to be homogeneous over the entire grid. Different layers are chosen (see Tables 5 to 7) to be simulated in order to represent the vertical heterogeneity of the lithology of the Salzwedel-Peckensen reservoir (see Table 2).

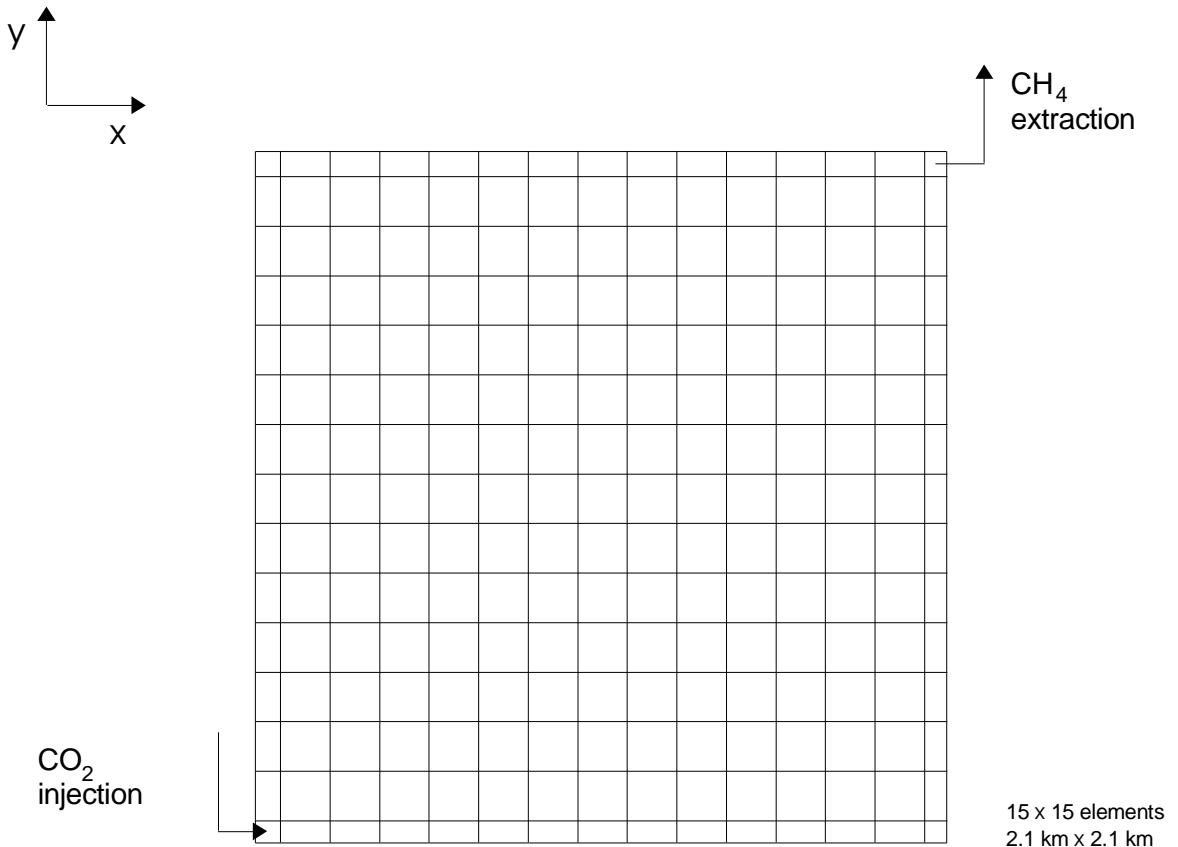


Figure 14: The 2D mesh is discretized in xy by 15 × 15 gridblocks.

*Table 5: The different parameters which are used in the 2D simulations of single units (i). The injection rate amounts to 0.0178 kg/s.*

	Case b1	Case b2	Case b3	Case b4	Case b5	Case b6
permeability [m <sup>12</sup> ]	$1 \times 10^{-12}$	$5 \times 10^{-16}$	$1 \times 10^{-12}$	$5 \times 10^{-16}$	$1 \times 10^{-12}$	$5 \times 10^{-16}$
usable porosity [%]	8	8	5	5	15	15
equivalent to Unit	Z9–11	Zyk17	—	Zyk12	Zyk13	approx. Zyk14
injection rate [kg/s]	0.0178	0.0178	0.0178	0.0178	0.0178	0.0178
time of breakthrough	>40 a					
simulated time	40 a					
machine	P 4 <sup>(1)</sup>					
number of time steps	37	77	37	73	37	42
calculation time	8 s	32 s	8 s	32 s	8 s	8 s

(1) ≈ Intel(R) Pentium(R) 4 CPU 2.80GHz 512 KB, LINUX

*Table 6: The injection rate of the 2D simulations amounts to 2.9091 kg/s (ii).*

	Case b7	Case b8	Case b9	Case b10	Case b11	Case b12
permeability [m <sup>12</sup> ]	$1 \times 10^{-12}$	$5 \times 10^{-16}$	$1 \times 10^{-12}$	$5 \times 10^{-16}$	$1 \times 10^{-12}$	$5 \times 10^{-16}$
usable porosity [%]	8	8	5	5	15	15
equivalent to Unit	Z9–11	Zyk17	—	Zyk12	Zyk13	approx. Zyk14
injection rate [kg/s]	2.9091	2.9091	2.9091	2.9091	2.9091	2.9091
1 % CO <sub>2</sub> contamination	0.6 a	—	0.5 a	—	1.6 a	—
10 % CO <sub>2</sub> contamination	1.2 a	—	0.7 a	—	2.2 a	—
50 % CO <sub>2</sub> contamination	1.7 a	—	1.0 a	—	3.2 a	—
simulated time	40 a	1.3 d	40 a	3.9 d	40 a	3.9 d
machine	P 4 <sup>(1)</sup>					
number of time steps	280	9999	313	9999	222	9999
calculation time	136 s	1544 s	176 s	1544 s	104 s	1544 s

(1) ≈ Intel(R) Pentium(R) 4 CPU 2.80GHz 512 KB, LINUX

*Table 7: The injection rate of the 2D simulations amounts to 0.0068 kg/s (iii).*

	Case b13	Case b14	Case b15	Case b16	Case b17	Case b18
permeability [m <sup>12</sup> ]	$1 \times 10^{-12}$	$5 \times 10^{-16}$	$1 \times 10^{-12}$	$5 \times 10^{-16}$	$1 \times 10^{-12}$	$5 \times 10^{-16}$
usable porosity [%]	8	8	5	5	15	15
equivalent to Unit	Z9–11	Zyk17	—	Zyk12	Zyk13	approx. Zyk14
injection rate [kg/s]	0.0068	0.0068	0.0068	0.0068	0.0068	0.0068
time of breakthrough	>40 a					
simulated time	40 a					
machine	P 4 <sup>(1)</sup>					
number of time steps	37	41	37	54	37	37
calculation time	8 s	8 s	8 s	24 s	8 s	8 s

(1) ≈ Intel(R) Pentium(R) 4 CPU 2.80GHz 512 KB, LINUX

Three parameters (permeability, porosity, and injection rate) are varied for a first simulation of the horizontal units (see Tables 5 to 7). Values are chosen to represent individual units used later in the 3D grid. Since the permeability  $k$  is scale dependent, the highest  $k$  value in the model is multiplied by 10 compared to the maximum  $k$  of  $100 \times 10^{-12} \text{ m}^2$  cited in the literature. Usable porosities of 5 %, 8 %, and 15 % were chosen, related to the average value of 8 % quoted in the literature [Schumacher and May, 1990]. As no information was available on the spatial inhomogeneities within one geologic layer, porosity and permeability are assumed to be isotropic throughout the whole xy grid. The permeabilities vary from 0.5 mD to 1000 mD, representing hydrostratigraphic units with higher amounts of clay and silt, and higher amounts of sand, respectively. The CO<sub>2</sub> injection rates come to 0.0068 kg/s, 0.0178 kg/s, and 2.9091 kg/s. They are based on the distribution of the CO<sub>2</sub> injection into different units, depending on their permeability and their thickness, used in the 3D simulations (see Section 9.2).

The two-dimensional simulation examines the flow in the Units Z9–11, the silt layer of the Mellin Wechselfolge, with a usable porosity of 8 % and a high permeability of 1000 mD, representing the structure with the highest  $k$  in the 3D model. In the so-called Case b1, a moderate CO<sub>2</sub> injection rate of 0.0178 kg/s is chosen. The injected gas spreads radially from the injection well in the lower left corner to the production well in the upper right. Within 1 year, CO<sub>2</sub> in the gas phase reaches 90 % inside a circle with a radius of 300 m around the injection site. At the end of the expected 40 years injection phase, this radius grows to 700 m, i. e., less than 15 % of the reservoir area is filled with CO<sub>2</sub>. The natural gas extracted at the production well is not contaminated.

In order to illustrate the effect of a higher injection rate, calculations with an injection rate of 2.9091 kg/s are made for comparison. Figures 22 to 25 document the time-dependent distribution of pressure, liquid saturation, and CO<sub>2</sub> in gas and liquid phases within the simulated time frame of 40 years for Case b11. The spatial coordinates are given in meters. After one year, almost a quarter of the reservoir is filled with CO<sub>2</sub>. The radius of the 90 % CO<sub>2</sub> in the gas-phase front reaches 1 km. At a distance of 1.8 km from the injection site, the CO<sub>2</sub> concentration in the gas phase is still lower than 5 %. Already within about one year, CO<sub>2</sub> reaches the production well, i. e., the contamination of natural gas with CO<sub>2</sub> occurs. In more detail, after 0.6 a the CO<sub>2</sub> reaches 1 % in the neighboring gridblock of the production well, and 50 % after 1.6 a in Unit z9-11, Case 7 (see Table 6). In the other high-permeability Unit Zyk13, CO<sub>2</sub> reaches 1 % in the neighboring gridblock of the production well after 1.7 a, and 50 % after 3.2 a. In the Cases b1 to b6 and b13 to b18 with injection rates of 0.0178 kg/s and 0.0068 kg/s a breakthrough does not occur within the extraction and injection period of 40 years. During the simulated time, the pressure always remains below 22.0 MPa, and drops slightly in the last decades, due to the higher solubility of the intruding CO<sub>2</sub> compared to the displaced CH<sub>4</sub>, and the corresponding CO<sub>2</sub> dissolution into the aqueous phase.

The simulations listed in Tables 5 to 7 were performed in order to investigate the influence on the flow through the main characteristics of the hydrostratigraphic units, like porosity, permeability, and the injection rate. Figures 26 to 33 document the results, i. e., distribution of pressure, liquid saturation, and CO<sub>2</sub> in gas and liquid phase after 1 year of CO<sub>2</sub> injection and simultaneous CH<sub>4</sub> extraction. The same cases are reproduced in Figures 34 to 41 at the end of the active period of 40 years. Each column has the same porosity, from left to right 5 %, 8 %, and 15 %, respectively. The permeability changes by more than three orders of magnitude to cover the variation of the layers, i. e., from sand to clay composition. The simulations in the first and third rows in the

Figures 26 to 32, and 34 to 40, first row in 27 to 33, and 35 to 41 are performed using 1000 mD. The remaining diagrams are calculated with a lower  $k$  of 0.5 mD. The effect of the CO<sub>2</sub> injection rate was tested for three different values. An intermediate rate of 0.178 kg/s in the first two rows of the Figures 26 to 32, 34 to 40, increases to 2.9091 kg/s in the lower rows of the Figures 26 to 32, 34 to 40, and drops to a lower value of 0.0068 kg/s in the Figures 35 to 41. In general, the differences within a row of plots are smaller than those between the columns, i.e., the variability of the usable porosities has only a minor impact on the parameter distributions, compared to the influence of the changed injection rate.

After 40 years of CO<sub>2</sub> injection at 0.0178 kg/s, the reservoir with  $k$  of 1000 mD is filled to about 10 % to 30 % with 90 % CO<sub>2</sub> in the gas phase (see Figure 38). For the Cases 1, 3, and 5 the limit to 5 % CO<sub>2</sub> in the gas phase reaches a radius around the injection well of about 1 km to 1.6 km. Depending on the usable porosity, the 90 % front reaches the 500 m to 900 m radius. As the permeabilities are smaller in the Cases 2, 4, and 6, the area filled with 90 % CO<sub>2</sub> in the gas phase after 40 years is slightly smaller than in the cases discussed above. The 5 % front crosses at 500 m to 800 m, the 90 % at 1 km to 1.4 km. However, for the Cases 7, 9, and 11, with injection rates of 2.9091 kg/s, practically the whole reservoir is filled with CO<sub>2</sub> in about 1 year (see Figure 30). Using a relatively low injection rate of 0.0068 kg/s for Cases 13 to 18, 5 % to 10 % of the 2D reservoir is flooded with 90 % CO<sub>2</sub> in the gas phase after 40 years, depending on permeability and usable porosity. The unit Zyk13, with the highest permeability of 1000 mD and the lowest usable porosity of 5 %, exhibits the fastest CO<sub>2</sub> spreading through the grid, hence the earliest breakthrough at the CH<sub>4</sub> production well. The second case showing a fast contamination of the produced CH<sub>4</sub> is the Unit Z9–11 with the same high  $k$  and a usable porosity of 8 %.

## 9 Three-dimensional Simulation of a Base-case

The 3D model was derived similarly to the 2D model. A volume representing a quarter of a five-spot configuration is used to model of the Salzwedel-Peckensen reservoir (see Section 7). Only the reservoir region with the gas-containing Units Zyklus 17 to Zyklus 7 [Bandlova, 1998], [Stoll, 1981] and the adjacent layers are of interest for the simulation. These nine layers are represented using six different rock types, each with homogeneous, isotropic properties (see Table 8). (Here the base-case is named Case a10.) The Unit Zyklus 1–6 lies probably below the gas-water contact and is excluded from the model domain.

The pressures in the active production regions range from 4.5 MPa to 22 MPa [Khoklov, 2004]. For the model, a hydrostatic pressure regime with 20 MPa at the bottom of the simulated reservoir region is used. A constant temperature of 120 °C is assumed throughout the reservoir. As mentioned earlier in Section 4, the produced natural gas consists mainly of three different gas components. For first 3D simulations, it is sufficient to consider CH<sub>4</sub> together with N<sub>2</sub> as one gas (which fills the reservoir at the beginning) and CO<sub>2</sub> as a second gas. This assumption is justified on the basis of gas mixture calculations, (see Section 6), and is already applied in the 2D model (see Section 8).

Table 8: Eleven 3D cases are simulated with different permeabilities, as low as  $5 \times 10^{-17} \text{ m}^2$  to  $2.5 \times 10^{-15} \text{ m}^2$  and as a high as  $10^{-13} \text{ m}^2$  to  $10^{-11} \text{ m}^2$ .

	Case a1	Case a2	Case a3	Case a4	Case a5	Case a6	Case a7	Case a8	Case a9	Case a10	Case a11
perm. in Zyk13 [ $\text{m}^2$ ]	$1 \times 10^{-12}$	$1 \times 10^{-13}$	$1 \times 10^{-13}$	$1 \times 10^{-11}$	$1 \times 10^{-13}$	$2 \times 10^{-12}$	$5 \times 10^{-13}$	$2 \times 10^{-13}$	$5 \times 10^{-12}$	$1 \times 10^{-13}$	$1 \times 10^{-11}$
perm. in Z9-11 [ $\text{m}^2$ ]	$1 \times 10^{-12}$	$1 \times 10^{-13}$	$1 \times 10^{-13}$	$1 \times 10^{-11}$	$1 \times 10^{-13}$	$2 \times 10^{-13}$	$5 \times 10^{-12}$	$2 \times 10^{-13}$	$5 \times 10^{-12}$	$1 \times 10^{-13}$	$1 \times 10^{-11}$
perm. in other units [ $\text{m}^2$ ]	$5 \times 10^{-16}$	$5 \times 10^{-16}$	$5 \times 10^{-16}$	$5 \times 10^{-17}$	$5 \times 10^{-15}$	$1 \times 10^{-16}$	$2.5 \times 10^{-15}$	$5 \times 10^{-16}$	$5 \times 10^{-16}$	$1 \times 10^{-16}$	$2.5 \times 10^{-15}$
injection rates $q_i$ [kg/s]											
in A11.1 and A21.1	0.0178	0.1516	0.0018	0.0178	0.0178	0.0178	0.0178	0.0090	0.0004	0.0036	0.0009
in A31.1 and A41.1	0.0127	0.1083	0.0013	0.0127	0.0127	0.0127	0.0127	0.0064	0.0003	0.0026	0.0006
in A51.1 and A61.1	0.0118	0.1011	0.0012	0.0118	0.0118	0.0118	0.0118	0.0060	0.0002	0.0024	0.0006
in A71.1 and A81.1	0.0072	0.0614	0.0007	0.0072	0.0072	0.0072	0.0072	0.0034	0.0001	0.0015	0.0004
in A91.1 and A11.1	1.0148	0.8664	1.0325	1.0148	1.0148	1.0148	1.0148	1.0245	1.0341	1.0305	1.0335
in AB1.1 and AC1.1	0.0106	0.0903	0.0011	0.0106	0.0106	0.0106	0.0106	0.0053	0.0002	0.0021	0.0005
in AD1.1 and AE1.1	2.9091	2.4838	2.9598	2.9091	2.9091	2.9091	2.9091	2.9370	2.9644	2.9541	2.9626
in AF1.1 and AG1.1	0.0093	0.0794	0.0009	0.0093	0.0093	0.0093	0.0093	0.0047	0.0002	0.0019	0.0005
in AH1.1 and AI1.1	0.0068	0.0578	0.0007	0.0068	0.0068	0.0068	0.0068	0.0034	0.0001	0.0014	0.0003
simulated time	40 a	40 a	6.7 a	40 a	5.4 a	40 a	23.4 a	40 a	40 a	40 a	18.0 a
Zyk13 and Z9-11											
compared to those in standard Case 1	1	10 × smaller	10 × higher	10 × smaller	10 × higher	5 × smaller	5 × higher	5 × smaller	5 × higher	10 × smaller	10 × higher
other units compared to those in standard Case 1	1	1	1	10 × smaller	10 × higher	5 × smaller	5 × higher	1	1	5 × smaller	5 × higher
high permeability to low permeability											
time at which CO <sub>2</sub> in gas phase close to production well > 1%	4.7 a	7.8 a	2.1 a	7.8 a	1.9 a	7.0 a	2.5 a	6.9 a	2.7 a	7.7 a	2.0 a
time at which CO <sub>2</sub> in gas phase close to production well > 10 %	5.6 a	9.8 a	2.6 a	9.8 a	2.4 a	8.6 a	3.1 a	8.4 a	3.3 a	9.7 a	2.4 a
CO <sub>2</sub> in gas phase close to production well > 20 %	6.2 a	10.8 a	3.0 a	10.7 a	2.7 a	9.5 a	3.4 a	9.2 a	3.7 a	10.6 a	2.8 a
CO <sub>2</sub> in gas phase close to production well > 30 %	6.6 a	11.6 a	3.6 a	11.5 a	3.2 a	10.1 a	3.9 a	9.9 a	4.3 a	11.5 a	3.2 a
CO <sub>2</sub> in gas phase close to production well > 40 %	7.2 a	12.4 a	4.3 a	12.4 a	3.7 a	10.9 a	4.5 a	10.6 a	5.0 a	12.2 a	3.9 a
CO <sub>2</sub> in gas phase close to production well > 50 %	8.1 a	13.2 a	5.8 a	13.2 a	4.7 a	11.7 a	5.3 a	11.3 a	6.0 a	13.2 a	4.9 a
machine	P 4 (1)	P 4 (1)	P 4 (1)	AMD (2)	AMD (2)	P 4 (1)	P 4 (1)	P 4 (1)	P 4 (1)	P 4 (1)	P 4 (1)
number of time steps	354	211	263	232	176	273	345	275	558	231	402
calculation time	6136 s	3544 s	— (3)	6064 s	— (3)	4112 s	— (3)	4032 s	10672 s	3240 s	— (3)

(1)  $\hat{=}$  Intel(R) Pentium(R) 4 CPU 2.80GHz 521 KB, LINUX  
(2)  $\hat{=}$  AMD Athlon(tm) MP Processor 1800+ 256 KB, LINUX  
(3)  $\hat{=}$  no convergence

The 3D calculations presented in this section are carried out in three steps:

1. A steady initial state is established, by (i) performing a 1D simulation of one vertical column and (ii) replicating this column in the two lateral directions so as to obtain the initial conditions for the 3D grid.
2. The subsequent CH<sub>4</sub> extraction and CO<sub>2</sub> injection phase has a duration of 40 years.
3. The final relaxation phase lasts for at least an additional 40 years.

## 9.1 Production

CH<sub>4</sub> is produced in such a way that the bottomhole well pressure remains constant i.e., an implementation of Dirichlet conditions. This is realized by using gridblocks with huge sizes for the production grid blocks, virtual volumes are of the order of 10<sup>55</sup> m<sup>3</sup> to 10<sup>56</sup> m<sup>3</sup>. This procedure for creating the sink was already applied in the 2D model and is retained for the following simulations.

## 9.2 Injection

The storage capacity of the site should allow for the accumulation of about  $4.2 \times 10^{11}$  kg CO<sub>2</sub> ( $212 \times 10^9$  m<sup>3</sup>) over a time period of 40 years. This corresponds to an injection rate of 332.9 kg/s. Assuming 10 injection sites, and considering that in the five-spot configuration only a quarter of one well region is used, this leads to an injection rate of about 8 kg/s CO<sub>2</sub> per well in the model.

Furthermore, in order to respect the properties of the different geologic layers, one has to calculate injection rates  $q_i$  for each unit  $i$  using

$$q_i = Q \frac{k_i h_i}{\sum_j k_j h_j} , \quad \sum_i q_i = Q ,$$

where

$Q \hat{=} \text{total injection rate in the five-spot configuration}$

$k_i \hat{=} \text{permeability of unit } i$

$h_i \hat{=} \text{height of unit } i .$

## 9.3 CH<sub>4</sub> Extraction and CO<sub>2</sub> Injection Phase

Simulations of CH<sub>4</sub> extraction and CO<sub>2</sub> injection are performed for a base-case for a time period of 40 years. Figures 42 to 48 show the time-dependent development of the parameters in the 3D grid — pressure, liquid saturation, and CO<sub>2</sub> and CH<sub>4</sub> in gas and liquid phases. For a better overview the diagrams of Figures 43 to 48 illustrate the data using a diagonal vertical slice of the square five-spot volume. The spatial coordinates are given in meters.

The extraction of CH<sub>4</sub> occurs in 18 gridblocks in a vertical column. In the diagrams (e.g., Figures 42 to 48) the production well is located in the left corner (see also Figure 13). The injection

well is situated in the opposite right corner. The injection of CO<sub>2</sub> is distributed among 18 layers according to the height and permeability of each layer (Table 8, eleventh column, Case a10), as described in the Section 9.2. The Units Zyk13 (gridblocks AD1 1, AE1 1) and Z9–11 (AD1 1, AE1 1) have isotropic permeabilities of  $1 \times 10^{-12} \text{ m}^2$ , while all other units have isotropic permeabilities of  $5 \times 10^{-16} \text{ m}^2$ . In Table 8, the distribution of the usable porosities is listed. The CO<sub>2</sub> is injected at a constant total rate  $Q$  of 8 kg/s in the entire model area over the complete simulation time.

Starting with initial conditions of steady state, the injected CO<sub>2</sub> pressurizes the reservoir and sweeps the methane in the direction of the extraction well. Obvious is the faster CO<sub>2</sub> flow in the units with higher permeabilities, Zyk13 and Z9–11, as the highest portions of the CO<sub>2</sub> injection take place there, with  $q_{\text{Zyk13}}$  of 1.0148 kg/s per injection gridblock and  $q_{\text{z9-11}}$  of 2.9091 kg/s per injection gridblock. The CO<sub>2</sub> breakthrough at the production well occurs in these units first. Breakthrough time is defined as the time when the injected CO<sub>2</sub> arrives at a neighboring gridblock adjacent to the production well. The CO<sub>2</sub> reaches the CH<sub>4</sub> production site first in the Unit Z9–11. The limit of 1% CO<sub>2</sub> in the gas phase at the sink site is obtained after 7.7 years, and the 10% threshold after 10.6 years.

The arrival of CO<sub>2</sub> at blocks A9F14 and AAF14 (upper and lower gridblock of Zyk13, purple and light blue lines) and ADF14 and AEF14 (upper and lower gridblock of Z9–11, red and green lines) is illustrated in Figure 67, diagram first row, first column. The CO<sub>2</sub> flow is faster in Z9–11, because porosity is lower here. Within Z9–11 the lower gridblock shows the faster increase in CO<sub>2</sub> concentration in the gas phase due to gravity effects. Illustrations of the development of pressure, liquid saturation, and CO<sub>2</sub> and CH<sub>4</sub> in their gas phase in Zyk13 are given in horizontal slices of the 3D simulations in Figures 49 to 51, which should be compared with Figures 22 to 41 of the 2D simulations of Section 8.

This case reveals the potential difficulties of carbon sequestration with enhanced gas recovery. Specifically CO<sub>2</sub> may flow much faster in some layers as compared to the main portion of the reservoir, so premature contamination of the extracted gas may occur through these layers. In the remaining layers there would still be CH<sub>4</sub> left in place, and significant storage volume for CO<sub>2</sub> would remain unused at the end of the injection period. In addition to the spatial distribution of the main parameters, it is of interest to have a closer look at their development in time. Figures 52 to 54 show the time-dependent development of pressure, liquid saturation, and gas composition at specific gridblocks: the column of the injection well (blocks A11 1 — AI1 1), a neighboring vertical column (blocks A12 1 — AI2 1), a neighboring vertical column to the extraction well (blocks A1F14 — AIF14), and for a comparison the column of the extraction well itself (blocks A1F15 — AIF15). As required, the gridblocks at the extraction site stay at their hydrostatic pressure level (see Figure 52). Within the other columns the pressure starts from the hydrostatic distribution and increases at an earlier or a later time depending on their distance to the injection well, reaching maximum pressure values of 20.15 MPa to 20.6 MPa in the lowest reservoir unit. The maximum value for  $p$  obtained at the injection well is at about 20.8 MPa.

Analyzing the same vertical columns for CO<sub>2</sub> in the gas phase shows (i) zero CO<sub>2</sub> at the extraction site, and (ii) increasing concentrations of CO<sub>2</sub> in the gas phase at the injection site, starting from zero asymptotically to 1, with different gradients due to the different injection rates in each unit and the different hydrostatic pressure due to their vertical position (see Figure 53). In the

vertical column close to the injection well, the gradients of the increase vary widely, 100 %/year to 40 %/year. In the proximity of the production site, CO<sub>2</sub> emerges first after about 7.7 years in gridblock AEF14, the lower block in Z9–11. As CO<sub>2</sub> concentrations increase, the concentrations of CH<sub>4</sub> decrease (see Figure 54).

## 9.4 Relaxation Phase

Subsequent to the 40-year extraction and injection phase, a relaxation phase is performed for the base-case, i. e., neither sink nor source is applied. Results for the distribution of pressure, liquid saturation, and CH<sub>4</sub> and CO<sub>2</sub> concentrations in liquid and gas phases are provided in Figures 55 to 60.

Over time, the reservoir shows an equalizing of the disturbances and approaches balanced conditions. Hydrostatic pressure is re-established after a few decades, and differences in gas composition between different layers are reduced. In particular, the low permeability Unit Zyk12, situated between the two higher permeability Units Zyk13 and z9-11, adopts the conditions of its neighbors.

# 10 Variation of the Injection Rates in the 3D Model

Carbon dioxide sequestration with enhanced gas recovery in a reservoir is a complex problem, influenced by many different parameters. In order to obtain a better understanding of the characteristics of the reservoir and the behavior of the fluids and gases involved, sensitivity tests for different parameters are helpful. One main parameter of interest is the injection rate. It is not exactly known today how much CO<sub>2</sub> will be available at what time, and how many wells can be used in total, and in what kind of geometric pattern. Hence we have investigated the effects of varying CO<sub>2</sub> injection rate on CSEGR.

Proceeding from the base-case, described in Section 9.3, five different injection rates  $Q$  are modeled, ranging from 0.8 kg/s to 16.0 kg/s ( $\hat{=} 2.5 \times 10^7$  kg/a to  $5 \times 10^6$  kg/a) (see Table 9). The injection rate of each unit  $q_i$  is calculated depending on the permeabilities and unit thickness. As initial conditions, the steady state of Section 9.3 is used.

## 10.1 CH<sub>4</sub> Extraction and CO<sub>2</sub> Injection Phase

All simulations were performed for a 40-year period of CH<sub>4</sub> extraction, with simultaneous CO<sub>2</sub> injection, retaining the other model characteristics as listed above. Therefore the total amount of CO<sub>2</sub> injection reaches  $2 \times 10^9$  kg to  $2 \times 10^{10}$  kg within the 40-year life span of the sequestration site.

For simulations with high injection rates  $Q$ , the production well shows an undesirable early contamination with CO<sub>2</sub>. After 40 years the cases with smaller  $Q$  are still below 30 % CO<sub>2</sub> in the gas phase (Case c,  $Q = 1.6$  kg/s) and 0.1 % CO<sub>2</sub> in the gas phase (Case d,  $Q = 0.8$  kg/s), respectively.

The 3D plots in Figures 61 to 64 illustrate 3D-cubes or a 2D-diagonal-section of the 3D-cube, representing distribution of pressure, liquid saturation, and CH<sub>4</sub> and CO<sub>2</sub> concentration in liquid

*Table 9: Case a to Case e represent variations of the total CO<sub>2</sub> injection rate Q.*

	Case a	Case b	Case c	Case d	Case e
total injection CO <sub>2</sub> rate $Q$ [kg/s]	8.0	4.0	1.6	0.8	16.0
$Q$ compared to $Q$ in Case a	1	2 × smaller	5 × smaller	10 × smaller	2 × bigger
simulated time	40 years				
injection rates $q_i$ [kg/s] in A11 1 and A21 1 (Zyk17)	0.0036	0.0018	0.0007	0.00036	0.0072
A31 1 and A51 1 (Zyk16)	0.0026	0.0013	0.0005	0.00026	0.0052
A51 1 and A61 1 (Zyk15)	0.0024	0.0012	0.0005	0.00024	0.0048
A71 1 and A81 1 (Zyk14)	0.0015	0.0007	0.0003	0.00015	0.0029
A91 1 and AA1 1 (Zyk13)	1.0305	0.5152	0.2061	0.10305	2.0601
AB1 1 and AC1 1 (Zyk12)	0.0021	0.0011	0.0004	0.00021	0.0043
AD1 1 and AE1 1 (Z9–11)	2.9541	1.4770	0.5908	0.29541	5.9081
AF1 1 and AG1 1 (Zyk08)	0.0019	0.0009	0.0004	0.00019	0.0038
AH1 1 and AI1 1 (Zyk07)	0.0014	0.0007	0.0003	0.00014	0.0027
time CO <sub>2</sub> in gas phase > 1 %	7.7 a	14.0 a	29.2 a	> 40 a	4.2 a
time CO <sub>2</sub> in gas phase > 10 %	9.7 a	17.2 a	34.7 a	> 40 a	5.3 a
time CO <sub>2</sub> in gas phase > 50 %	13.2 a	23.1 a	> 40 a	> 40 a	7.3 a
CO <sub>2</sub> in gas phase after 40 a	97.4 %	88.2 %	29.5 %	0.08 %	98.7 %
machine	P 4 <sup>(1)</sup>				
time steps	231	207	151	115	202
calculation time	3240 s	2944 s	2168 s	1624 s	2928

(1)  $\hat{=}$  Intel(R) Pentium(R) 4 CPU 2.80GHz 512 KB, LINUX

and gas phases. For the analysis of the effect of the injection rate  $Q$ , the variation of  $Q$  ranges from 0.8 kg/s to 16.0 kg/s. The simulations of CH<sub>4</sub> extraction and CO<sub>2</sub> injection over 1 year show the evolution of pressure  $p$  in the 3D grid. In further variation of parameters subsequently, the relatively high injection rate  $Q$  of Case a (8 kg/s) is used.

## 11 Variation of the Permeabilities in the 3D Model

In addition to the injection rate, the properties of different geological layers play a role in the behavior of a reservoir. In order to study the effects of permeability  $k$ , which represents one of the main parameters, eleven cases are simulated. Permeabilities are chosen as low as  $5 \times 10^{-17} \text{ m}^2$  to  $2.5 \times 10^{-15} \text{ m}^2$  for the units representing geological layers with higher amounts of clay and silt, and as a high as  $10^{-13} \text{ m}^2$  to  $10^{-11} \text{ m}^2$  for units representing higher proportions of sand (see Table 8). Also the permeability ratio varies between lower- and higher- $k$  units ranges from 1:200 to 1:10000. All other properties are left unchanged.

### 11.1 Breakthrough During the CH<sub>4</sub> Extraction and CO<sub>2</sub> Injection Phase

The spatial evolution after 1 year of pressure and CO<sub>2</sub> gas-phase concentration is depicted in Figures 65 to 66 for the 11 different cases (see Table 8). The appearance of CO<sub>2</sub> close to the production well is of importance for the evaluation of enhanced gas recovery. This is illustrated using the CO<sub>2</sub> concentration in the gas phase in the neighboring vertical column to the extraction well, i. e., in

the gridblocks A9F14 to A1F14 (see Figure 67). The CO<sub>2</sub> arrival in the neighboring gridblock of the production well is first observed at the bottom of the high-permeability Unit Z9–11, gridblock AEF14, as already presented in Section 9.3. A comparison of the different times to reach given CO<sub>2</sub> mass fractions in the gas phase is shown in Figure 68. Different colors show the development of CO<sub>2</sub> mass fraction in the gas phase. In the simulated cases the breakthroughs occur between a few years and more than ten years. The increase from 1 % to 50 % takes place within about 2 years to 5 years.

The progress of the breakthrough is documented in Figure 67. For each of the simulated cases a1 to a11, the CO<sub>2</sub> concentration in the gas phase in 18 gridblocks in a vertical column, near the production well is determined. The blocks A9F14 and AAF14 (upper and lower gridblock of Zyk13) and ADF14 and AEF14 (upper and lower gridblock of Z9–11) shows the highest and fastest CO<sub>2</sub> contamination. Here, the time of breakthrough, noted on top of each plot, is defined for the time  $t$  when the CO<sub>2</sub> concentration in the gas phase reaches 10 % in the gridblock AEF14. The time of breakthrough lies within about 2 years and 10 years. It is mainly influenced by the permeability of the high permeability units,  $k$  of the other low-permeability unit is of only minor consequence. In cases including high-permeability units with very high permeabilities of  $10^{-11} \text{ m}^2$ , the time  $t$  comes to 2.4 years to 2.6 years, with relatively high permeabilities of  $10^{-12} \text{ m}^2$  and  $t$  amounts to 3.3 years to 5.6 years, and with moderate permeabilities of  $10^{-13} \text{ m}^2$ ,  $t$  runs up to 8.6 a to 9.8 a, respectively. Figure 69 shows a direct comparison of the time-dependent CO<sub>2</sub> concentration in the gas phase of the gridblock AEF14 in all eleven cases.

## 11.2 Relaxation Phase

The relaxation phase with a duration of 40 years is calculated for the cases 1, 2, 4, 6, 8, 9, and 10. Figures 70 to 75 illustrate the time-dependent distribution of pressure, liquid saturation, and CH<sub>4</sub> and CO<sub>2</sub> concentrations in liquid and gas phases.

Within each diagram the equalizing effect of time is recognizable. The main differences between the cases show up on the right-hand side of the plots, the area where the injection was placed during the active period, and the lower parts of the reservoir containing the units with the higher permeabilities.

## 12 Variation of Injection Strategies in the 3D Model

In order to optimize production and injection, i. e., to pressurize the reservoir and to delay the breakthrough at the extraction well, it may be possible to block the unit(s) with higher permeabilities in order to direct injected CO<sub>2</sub> into layers it otherwise would not enter. There are many different approaches tested already in enhanced oil recovery, e. g., chemical techniques (surfactants, polymers) [Zazovsky, 2004]. Although breakthroughs can be retarded, additional costs are a disadvantage.

For enhanced gas recovery, one option is to control the gas mobility by injecting water into selected layers. An advantage of this injection strategy is the possibility of disposing of water, which is an

unwanted by-product of natural gas extraction. Hence different cases with varying water injection rates into high-permeability layers were performed.

### 12.1 Strategy

In these examples, the sequence of TOUGH2 runs consists of the following:

1. establishing steady state;
2. blocking of high permeability unit(s) by injection of water simultaneously with CH<sub>4</sub>-extraction;
3. CH<sub>4</sub>-extraction and CO<sub>2</sub>-injection phase for 40 years;
4. relaxation phase.

Initial conditions were chosen to be the same as in Case a1, i.e., a permeability of  $10^{-12} \text{ m}^2$  for the high-permeability units Zyk13 and Z9–11, and  $5 \times 10^{-16} \text{ m}^2$  for the other, less permeable units (Table 8). Again the extraction of CH<sub>4</sub> in a vertical column is accomplished using huge volumes in the gridblocks A1F15 to AIF15.

### 12.2 Blocking One Layer with Different Amounts of Water for 5 years

Different cases were performed with varying amounts of water injected in the Unit Z9–11, where early CO<sub>2</sub> breakthrough would otherwise occur. The specifications are listed in Table 10. Performing 5 a of CH<sub>4</sub> extraction and H<sub>2</sub>O injection followed by the 40 years period of CH<sub>4</sub> extraction and CO<sub>2</sub> injection gives the following scenario: The CO<sub>2</sub> breakthrough still takes place in the Unit Zyk9–11 within the period of 40 years. It occurs first in the lower part of the high-permeability unit Z9–11. So the delay of breakthrough is given by the lowest gridblock in Z9–11 close to the production well, gridblock AEF14. The breakthrough time is listed for CO<sub>2</sub> in the gas phase reaching 1%, 10% and 50%.

The amount of water was varied from  $Q$  equal to 2.9 kg/s to 11.6 kg/s. Depending on the injected amount of water, 1% of the gas phase is CO<sub>2</sub> after about 5.5 years to 5.7 years. The threshold of 10% is reached after about 7 years. After 13 years to 12 years half of the gas phase close to the extraction site consists of CO<sub>2</sub>. At the end of a period of 40 years the maximum of CO<sub>2</sub> in the gas phase in the layer Zyk13 amounts to about  $2 \times 10^{-3}$ .

As had been expected, the CO<sub>2</sub> reaches the production well later when water blocking is applied. However, the delay of the breakthrough compared to Case a1 is very small, amounting to about 1 year. The concentration of 1% CO<sub>2</sub> in the gas phase is delayed for 0.7 years to 1 year, the concentration of 10% for 1.3 years to 1.7 years.

### 12.3 Blocking Two Layers with Different Amounts of Water for 5 years

In order to develop more effective blocking, further simulations were performed for mobility reduction in the layers Zyk13 as well as Z9–11 [Rebscher et al., 2004]. Water is injected for 5 years in these

Table 10: Properties of the  $H_2O$ -blocking scenarios.

	Case f	Case g	Case h	Case i
$H_2O$ injection rate $Q$	2.9091 kg/s	5.8182 kg/s	8.7272 kg/s	11.6364 kg/s
$Q$ compared to $Q$ in Case f	1	2 $\times$ bigger	3 $\times$ bigger	4 $\times$ bigger
$CO_2$ in gas phase of Unit Zyk13 after 40 years	$2.5 \times 10^{-3}$	$2.1 \times 10^{-3}$	$1.9 \times 10^{-3}$	$1.8 \times 10^{-3}$
time $CO_2$ in gas phase of Unit Z9–11 > 1 %	5.49 a	5.51 a	5.64 a	5.73 a
time $CO_2$ in gas phase of Unit Z9–11 > 10 %	6.86 a	6.90 a	7.10 a	7.27 a
time $CO_2$ in gas phase of Unit Z9–11 > 50 %	12.88 a	12.41 a	12.26 a	11.97 a
delay of breakthrough for > 1 % $CO_2$ in the gas phase compared to Case a1	0.74 a	0.76 a	0.89 a	0.98 a
delay of breakthrough for > 10 % $CO_2$ in the gas phase compared to Case a1	1.26 a	1.30 a	1.50 a	1.67 a
simulated time	40 a	40 a	40 a	40 a
machine	P 4 <sup>(1)</sup>	P 4 <sup>(1)</sup>	P 4 <sup>(1)</sup>	P 4 <sup>(1)</sup>
calculation time	7616 s	9208 s	8640 s	8216 s
time steps	399	369	415	421

(1)  $\hat{=}$  Intel(R) Pentium(R) 4 CPU 2.80 GHz 512 KB, LINUX

high-permeability layers (Zyk13 with the gridblocks A911 and AA11; Z9–11 with the gridblocks AD11 and AE11). The amount of water is varied from  $Q$  equal to 2.9 kg/s to 14.5 kg/s, Case f to Case j. The distribution of the water in the four gridblocks reflects the thickness of the Unit Zyk13, which is 12 m, and that of Z9–11, which is 43.4 m. In Table 11, the delay of breakthrough is stated for the time at which  $CO_2$  in the gas phase close to the production well exceeds 1 % and 10 %. The cases Case f to Case j represent variations of the total  $H_2O$  injection rate while Case a1 is the comparative case without water blocking.

Figure 76 shows the development of the water flow pattern by showing the liquid saturation  $SL$  at different time steps from the beginning (1 s) to the end of the water-injection period at 5 a. Obvious is the lateral intrusion of water in the two units. Due to gravity, the lower gridblocks of the Unit Z9–11 and Zyk13 show higher liquid saturation ( $SL$ ) values compared to the upper gridblocks of the same units. Further spreading of water in the z-direction because of gravity wets the underlying units also.

For comparison of the different water injection rates, the distributions of the different liquid saturations in the four scenarios Case f to Case i after 1 year and 2 years is shown in Figure 77. The figure illustrates the water flow patterns and the resultant, different distances covered by the water mass. After the 5 year term, the water reaches maximal distances of several hundreds of meters (Case f, injection rate 2.9 kg/s) to about 1 km (Case i, injection rate 11.6 kg/s).

*Table 11: Case f to Case j represent variations of the total  $H_2O$  injection rate for blocking the two high-permeability Units Zyk13 and of Z9–11.*

	Case a1	Case f	Case g	Case h	Case i	Case j
Q [kg/s]	—	2.9091	5.8182	8.7273	11.6364	14.5455
$Q$ compared to $Q$ in Case f	0	1	2 × bigger	3 × bigger	4 × bigger	5 × bigger
$q_i$ [kg/s] in Zyk13	—	0.7523	1.5047	2.2571	3.0094	3.7618
$q_i$ [kg/s] in Z9–11	—	2.1567	4.3135	6.4702	8.6270	10.7837
time $CO_2$ in gas phase > 1 %	4.75 a	4.96 a	5.07 a	5.16 a	5.28 a	5.31 a
time $CO_2$ in gas phase > 10 %	5.60 a	5.90 a	6.01 a	6.17 a	6.26 a	6.44 a
time between $CO_2$ in gas phase > 1 % til > 50 %	3.30 a	3.39 a	3.49 a	3.59 a	3.77 a	3.95 a
delay of breakthrough for > 1 %	—	0.213 a	0.323 a	0.516 a	0.529 a	0.555 a
delay of breakthrough for > 10 %	—	0.299 a	0.409 a	0.568 a	0.663 a	0.841 a
simulated time	40 a	40 a	40 a	40 a	42.4 a	40 a
machine	P 4 <sup>(1)</sup>					
number of time steps	354	418	509	471	10513	565
calculation time	6136 s	7248 s	10088 s	8632 s	—	11288 s

(1)  $\hat{=}$  Intel(R) Pentium(R) 4 CPU 2.80GHz 512 KB, LINUX

Following this 5 year period, the 40 years  $CH_4$  extraction and  $CO_2$  injection takes place (see Figure 78). The breakthrough still occurs first in the lower part of the high-permeability layer Z9–11. Hence the delay of breakthrough depends on the lowest gridblock in Z9–11, close to the production well, gridblock AEF14. This time is given for two concentration levels of  $CO_2$  in the gas phase, when it reaches 1 % and 10 %. Depending on the previously injected  $H_2O$ , the  $CO_2$  breakthroughs occur after about 5 years to 5.3 years for the threshold of 1 %  $CO_2$  in the gas phase. The 10 % limit is reached after 5.9 years to 6.4 years.

Compared to the case where no  $H_2O$  blocking was applied, Case a1, this is equivalent to a delay of  $CO_2$  breakthrough at the production well of 0.2 years to 0.6 years (1 % limit), 0.3 years to 0.8 years (10 % limit), respectively. An overview of the breakthrough times, as the time of  $CO_2$  arrival in the neighboring gridblock of the production well, is given in Figure 15.  $CO_2$  arrival is first observed in the bottom unit of the high-permeability Unit Z9–11. Different colors show the development of the increasing amount of  $CO_2$  in the gas phase. The six cases differ in the water injection rate ranging from no water (Case a1) to 14.5 kg/s (Case j) (see Table 11). In the simulated cases the breakthroughs occur at about 6 a, an increasing water injection rate leads to larger delay times. These delay times are relatively small, but they show that the undesired  $CO_2$  breakthrough can be retarded, e. g., using  $H_2O$  blocking, and more effective mobility-reducing strategies could potentially be developed.

In general, the following processes reduce the effectiveness of water injection for mobility reduction: First, the injected  $CO_2$  displaces water. In the two-phase gas-water system, the available pore space for the gas is reduced resulting in an unwanted higher gas-flow velocity. In addition, flow of water due to gravity is significant. Thus the fast path through the high-permeability unit is reopened. The conclusion is that the breakthrough times are increased, but remain on the same order of magnitude.

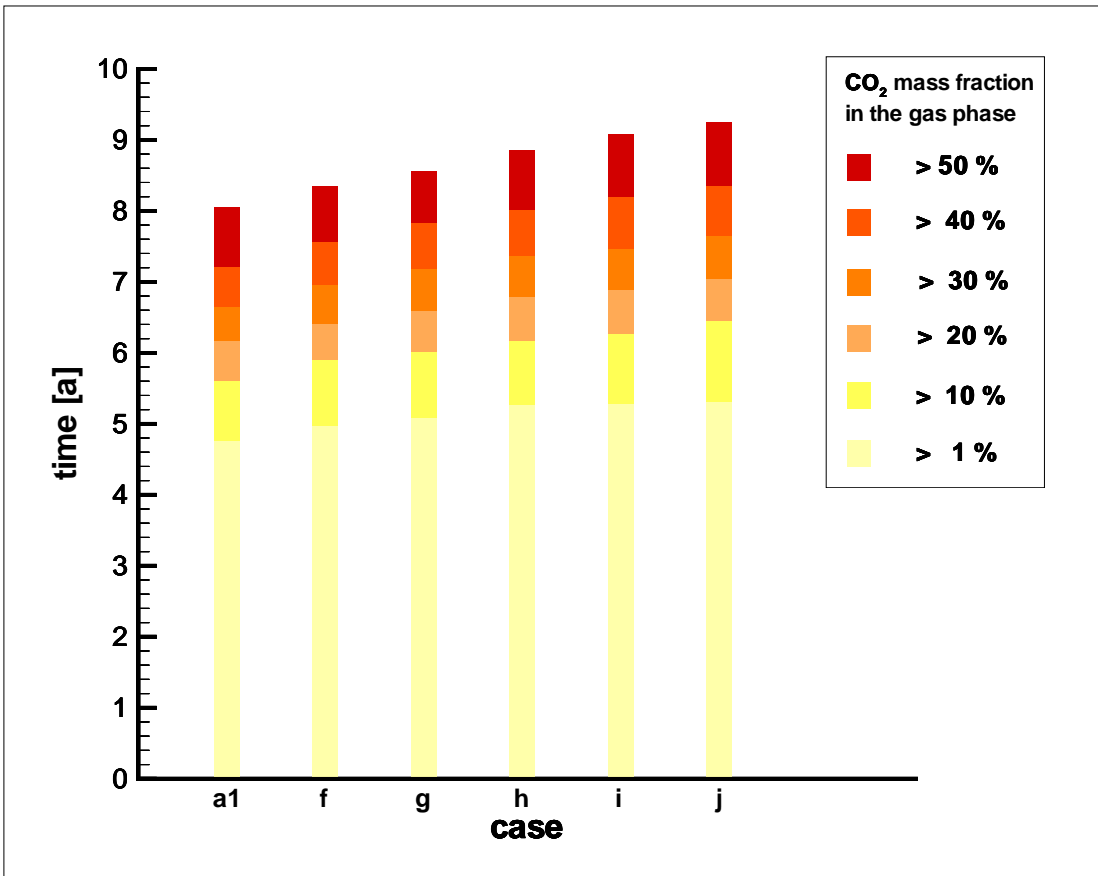


Figure 15: Time of  $\text{CO}_2$  arrival in the neighboring gridblock of the production well for Case a1 and Case f through Case j.

## 12.4 Blocking Two Layers with Different Amounts of Water for 10 years

In order to study the influence of time on the water blocking, one simulation with a water-blocking phase of 10 years is chosen, 1.5047 kg/s water for Unit Zyk13 (gridblocks A911 and AA11) and 4.3135 kg/s water for Z9–11 (gridblocks AD11 and AE11). All other parameters remained unchanged, including continuous  $\text{CH}_4$  extraction. The injection rate equals the one in Case g, but the injected volume of  $\text{H}_2\text{O}$  amounts in total to the same amount as in Case 7.

After this  $\text{H}_2\text{O}$  blocking phase of 10 years duration, the common  $\text{CH}_4$  extraction and  $\text{CO}_2$  injection phase starts. It is of interest to evaluate the  $\text{CO}_2$  breakthrough and compare this case with

- (i) no  $\text{H}_2\text{O}$  blocking, i.e., Case a1 of Table 8,
- (ii) 5 years blocking with same  $\text{H}_2\text{O}$  injection rate, i.e., Case g of the previous subsection,
- (iii) 5 years blocking with same total amount of injected  $\text{H}_2\text{O}$ , i.e., Case i of the previous subsection.

Table 12 gives an overview of the simulations of these four cases, listing the specifications of the water injection phase in the upper part of the table, followed by results CO<sub>2</sub> injection phase in the middle part. The three cases to the left in Table 12 represent the simulations with variations of the H<sub>2</sub>O injection strategy for blocking the two high-permeability Units Zyk13 and of Z9–11. They differ in the duration of blocking with H<sub>2</sub>O and their injection rates.

*Table 12: Properties of cases with variations of the H<sub>2</sub>O injection strategy for blocking the two high-permeability Units Zyk13 and of Z9–11.*

	Case a1	Case g	Case i	Case 10a
$q_i$ [kg/s] in Zyk13	—	1.5047	2.2571	1.5047
$q_i$ [kg/s] in Z9–11	—	4.3135	8.6270	4.3135
Q [kg/s]	0	5.8182	11.6364	5.8182
$Q$ compared to $Q$ in Case g	0	1	2 × bigger	same
H <sub>2</sub> O injection phase	0 a	5 a	5 a	10 a
H <sub>2</sub> O injection phase compared to Case g	0	1	same	2 × longer
time CO <sub>2</sub> in gas phase > 1 %	4.75 a	5.07 a	5.28 a	5.36 a
time CO <sub>2</sub> in gas phase > 10 %	5.60 a	6.01 a	6.26 a	6.34 a
time between CO <sub>2</sub> in gas phase > 1 % til > 50 %	3.30 a	3.49 a	3.77 a	3.71 a
delay of breakthrough for > 1 %	—	0.323 a	0.529 a	0.610 a
delay of breakthrough for > 10 %	—	0.409 a	0.663 a	0.740 a
simulated time	40 a	40 a	42.4 a	40 a
comparison to Case g	no blocking	—	2 × higher injection rate	2 × longer injection period
machine	P 4 <sup>(1)</sup>	P 4 <sup>(1)</sup>	P 4 <sup>(1)</sup>	AMD <sup>(2)</sup>
number of time steps	354	509	10513	576
calculation time	6136 s	10088 s	—	22880

(1) ≈ Intel(R) Pentium(R) 4 CPU 2.80GHz 512 KB, LINUX

(2) ≈ AMD Athlon(tm) MP Processor 1800+ 256 KB, LINUX

Case a1 is the comparison case without H<sub>2</sub>O blocking. In Case i an injection rate twice as high was used as in Case g. Case 10a has an injection period twice as long as Case g. The time of breakthrough is stated for the time at which CO<sub>2</sub> in the gas phase close to the production well exceeds 1 % and 10 %. The CO<sub>2</sub> breakthrough delay times are given in comparison to Case a1.

The times when the CO<sub>2</sub> breakthroughs happen close to the CH<sub>4</sub> production site are all of the same order of magnitude of about 5 years. The delay of breakthroughs compared to the non-blocking simulation Case a1 amounts to 0.3 years in Case g. Roughly a doubled time span of 5 years is obtained with a total water injection mass for Case i, 0.6 years for Case 10a, respectively. So only a minor difference can be observed if the distribution of water is varied in time.

## 13 Overall Summary

### Pre-studies

Based on publicly available data, parameters for the area of investigation were compiled. Evaluations of compressibility factor, density, and viscosity showed that the N<sub>2</sub>-CH<sub>4</sub>-CO<sub>2</sub> problem can be approximated as one with a gas mixture composed of only CH<sub>4</sub> and CO<sub>2</sub>. Simulations in a 2D areal geometry were performed covering 18 cases using different permeabilities on a 15 × 15 grid. These simulations represent horizontal slices of the 3D five-spot volume.

### Conceptual model description

The 3D grid is based on a five-spot-configuration with more than 4000 grid blocks, representing a section of the natural gas field Salzwedel-Peckensen with an area of 2.1 km × 2.1 km and a depth of 3000 m. The CH<sub>4</sub>-filled reservoir consists of nine layers, composed of six different rock types with usable porosities between 5 % and 15 % and permeabilities ranging from 0.5 mD to 1000 mD. Starting from steady-state conditions, constant temperatures of 120 °C, and a hydrostatic pressure distribution above 20 MPa, a 40 years active period of CH<sub>4</sub> extraction and simultaneous CO<sub>2</sub> injection is simulated. Sink and source sites representing wells are realized through vertical columns continuing from top to bottom, at opposite corners of the model cube.

### Base-case description

In the base-case, lower permeabilities of units amount to 0.05 mD, higher ones to 1000 mD. A total CO<sub>2</sub> injection rate of 8 kg/s is applied.

### Base-case results

Due to the injection of CO<sub>2</sub> the reservoir repressurizes. The gas injection sweeps the CH<sub>4</sub> towards the extraction well. The breakthrough occurs first in the thickest unit with the highest permeability. The contamination of the produced CH<sub>4</sub> by CO<sub>2</sub> ranges from 1 % after 4.7 years to 50 % after 8.1 years.

### Variations on the base-case

Three different modifications of the simulations were tested: (i) variation of CO<sub>2</sub> injection rate, (ii) variation of permeability of the rock layers, (iii) rates of water injection mobility reduction:

- Five cases were studied with total CO<sub>2</sub> injection rates covering 0.8 kg/s to 16 kg/s in the five-spot configuration. The resulting breakthrough times, taken when the CO<sub>2</sub> in the gas phase close to the production well exceeds 10 %, range from 5.3 years to longer than 40 years. CO<sub>2</sub> concentrations in the gas phase after 40 years cover a wide range from 0.1 % to almost 100 %.
- Eleven cases with differing permeabilities, as low as  $5 \times 10^{-17} \text{ m}^2$  to  $2.5 \times 10^{-15} \text{ m}^2$  and as a high as  $10^{-13} \text{ m}^2$  to  $10^{-11} \text{ m}^2$  are modeled. The time of breakthrough at the production well is essentially determined by the permeability of the high-permeability layers. Here permeabilities of  $10^{-11} \text{ m}^2$  lead to breakthroughs after about 2.5 years, permeabilities of  $10^{-13} \text{ m}^2$  to just under 10 years.

- Five cases were simulated with total water injection rates ranging from 2.9 kg/s to 14.5 kg/s for a time period of 5 years. In order to evaluate the delay of CO<sub>2</sub> breakthrough, a comparison with water injection lasting 10 years was simulated.

## 14 Discussion

As the simulations are based on publicly available data, they are rather generic and cannot be used for detailed reservoir modeling. However, the simulations contribute to the understanding of the complex processes and hence to decision-making as to whether the Altmark area in North Germany is a suitable site for carbon dioxide sequestration with enhanced gas recovery (CSEGR).

Decreasing pressures in gas reservoirs represent a problem for the gas industry, as gas production declines. Injection of CO<sub>2</sub> or other gases leads to higher pressures in reservoirs, which is of special importance for depleted or almost depleted gas reservoirs. The CO<sub>2</sub> sweeps the CH<sub>4</sub> towards the extraction site. On the other hand, one has to be concerned about fluid mobilities, as a breakthrough of the injected CO<sub>2</sub> at the extraction site is not desirable in the gas industry, because the CO<sub>2</sub> contaminates the extracted natural gas. The financial success of CSEGR depends mainly on the amount of CO<sub>2</sub> contamination, the time it occurs, and how much additional natural gas can be produced on what time scale.

Hence detailed studies on the basis of real data are needed in order to make predictions for particular reservoirs. The simulations presented here show that it is possible to repressurize the Altmark reservoir and enhance the natural gas production. The results of the different parameter variations show that (i) the area of investigation is a potential site for CSEGR, and (ii) the importance of detailed information of the region. The simulations with water injection emphasize that a delay of contamination and breakthrough can be obtained with adjusted injection strategies. The study stresses that there is a need for mobility control, especially as there are high-permeability units present.

Another economical factor is the number of wells, their use for natural gas extraction, CO<sub>2</sub> injection, or monitoring, their geometrical pattern, and which well spacing is suitable to achieve the desired annual injection rate, as well as the intended lifetime of the sequestration site. The conservative simulations performed here give rough estimates. The approximately 80 accessible wells in Salzwedel-Peckensen allow for an adequate distance between extraction and injection sites of about 2 km. To give a rough estimate, in Case c with an injection rate of 1.6 kg/s, about  $5 \times 10^6$  t CO<sub>2</sub> per year could be sequestered with a life span of about 40 years, whereas in Case a using 8 kg/s, about  $27 \times 10^6$  t CO<sub>2</sub> per year could be sequestered for about 10 years. Permeabilities of the rock layers were varied to simulate other representative cases. Here the extracted CH<sub>4</sub> is contaminated in Case a1 with 1% CO<sub>2</sub> after 4.7 years and with 50% after 8.1 years, in Case a10 with 1% CO<sub>2</sub> after 7.7 years and with 50% after 13.2 years. CO<sub>2</sub> breakthrough could be significantly retarded if the high-permeability layers would be blocked efficiently. Corresponding simulations based on further approaches besides water injection have not yet been studied.

## **15 Conclusions**

The numerical simulations on CO<sub>2</sub> sequestration with enhanced gas recovery (CSEGR) suggest that the Altmark area in the North German Basin is suitable for CO<sub>2</sub> storage. In the almost depleted natural gas field Salzwedel-Peckensen, the most prominent subreservoir of the Altmark, additional natural gas can be produced for 5 to 40 years. In the simplified 3D model the CO<sub>2</sub> breakthrough occurs first through the high-permeability layers within 10 years to more than 40 years in the simulations with various potential injection rates, and within 3 years to 10 years in the simulations with variation of the layer permeabilities. With appropriate injection and extraction strategies, e. g., by injecting water in the high-permeability units, the CO<sub>2</sub> breakthrough can be retarded for about another year. We performed parameter variations to cover a wide range of scenarios possible in the Altmark. More specific predictions can be obtained by further simulations based on detailed field data. In general, CSEGR appears to be promising for increasing natural gas production in the Altmark reservoirs while simultaneously sequestering CO<sub>2</sub>.

## **16 Outlook**

Further enhancements for simulations on carbon sequestration in the Altmark can be obtained with the following recommendations

- Consider using a more complex model, e. g., higher number of different units, consideration of lateral heterogeneities, extension to multigas system, consideration of chemical reactions;
- Use realistic production history based on actual production data;
- Simulate different injection strategies, e. g., inject dense supercritical CO<sub>2</sub> not into the entire vertical column, but only into lower areas of the reservoir, in order to push the lighter CH<sub>4</sub> gas upward;
- Analyse different blocking methods in addition to water injection;
- Calculate an optimal timing of the start of CO<sub>2</sub> injection;
- Optimize injection and extraction rates;
- Field testing is needed combined with simulations based on realistic data.

## **17 Acknowledgment**

The authors wish to express their thanks to Franz May of the Federal Institute for Geosciences and Natural Resources (BGR, Hannover, Germany) and Karsten Pruess of the Lawrence Berkeley National Laboratory for their constructive suggestions and comments. In addition, the authors are grateful to Karsten Pruess and Jens Birkholzer (Lawrence Berkeley National Laboratory) for their incisive reviews of the manuscript. The work was supported by the European Project CO<sub>2</sub>-STORE under Contract No. ENK5-CT-2002-99621 and the Lawrence Berkeley National Laboratory under Department of Energy Contract No. DE-AC03-76SF00098.

## References

- Albrecht, A. and S. T. Kandji, Review — Carbon sequestration in tropical agroforestry systems, *Agriculture, Ecosystems and Environment*, **99**, 15-27, 2003
- Ametistova, L., J. Twidell, and J. Briden, The sequestration switch: removing industrial CO<sub>2</sub> by direct ocean absorption, *The Science of the Total Environment*, **289**, 213-223, 2002
- Bandlowa, T., Erdgasführung im Karbon-Perm-Trias-Komplex der Mitteleuropäischen Senke, *Geolog. Jb.*, **A 151**, 3–65, 1998
- Benson, S. M. and L. Myer, Monitoring to ensure safe and effective geologic sequestration of carbon dioxide, Intergovernmental Panel on Climate Change (IPCC) Workshop for Carbon Capture and Storage, Regina, Canada, pp 15, November 18 – 21, 2002,  
<http://www.ecn.nl/ps/products/ipcc02/ccs02-10.pdf>
- Bode, S., Abatement Costs vs. Compliance Costs in Multi-Period Emissions Trading — The Firms' Perspective, Hamburgisches Welt-Wirtschafts-Archiv, (HWWA, Hamburg Institute of International Economics), HWWA Discussion Paper 230, pp 42, June 2003,  
[http://hwwa.de/Publikationen/Discussion\\_Paper/2003/230.pdf](http://hwwa.de/Publikationen/Discussion_Paper/2003/230.pdf)
- Brasser, Th., K. Fischer-Appelt, J. Larue, and J. Moenig, Hydrochemischer Character von Tiefenwässern in ausgewählten Regionen Deutschlands, Fachliche Unterstützung des BMU-Arbeitskreises zur Auswahl von Enlagerstandorten, pp 86, August 2001,  
[http://www.akend.de/aktuell/berichte/pdf/indikatoren\\_anhang1.pdf](http://www.akend.de/aktuell/berichte/pdf/indikatoren_anhang1.pdf)
- Christensen, N. P., Assessing European Potential for Geological Storage of CO<sub>2</sub> from Fossil Fuel Combustion GEUS, 5th International Conference on Greenhouse Gas Control Technologies, Cairns Australia, pp 7, August 13 – 15, 2000,  
<http://www.entek.chalmers.se/anly/symp/01christensen.pdf>
- Chung, T.-H., M. Ajlan, L. L. Lee, and K. E. Starling, Generalized multiparameter correlation for nonpolar and polar fluid transport properties, *Ind. Eng. Chem. Res.*, **27**, 671-679, 1988
- Clauser, C., H. Deetjen, F. Höhne, W. Rühaak, A. Hartmann, R. Schellschmidt, V. Rath, and A. Zschocke, Erkennen und Quantifizieren von Strömung: Eine geothermische Rasteranalyse zur Klassifizierung des tiefen Untergrundes in Deutschland hinsichtlich seiner Eignung zur Endlagerung radioaktiver Stoffe, Endbericht zum Auftrag 9X0009-8390-0, Rheinischwestfälische Technische Hochschule, Aachen und Institut für Geowissenschaftliche Gemeinschaftsaufgaben, Hannover, pp 159, June 6, 2002,  
<http://www.akend.de/aktuell/berichte/pdf/rasteranalyse.pdf>
- Clemens, T. G. and K. Wit, Zero Emission Power Generation Power plant concepts and CO<sub>2</sub> injection into gas fields, Shell Technology EP, Rijswijk, EP 2001-5403, December 2001

European Parliament and Council of Europe, Decision No 2002/ /EC of the European Parliament and of the Council of June 27 2002 concerning the Sixth Framework Programme of the European Community for research, technological development and demonstration activities, contributing to the creation of the European Research Area and to innovation (2002-2006), PE-CONS 3635/02, Luxembourg, pp 86, 2002

Freund, P., International Collaboration on Capture, Storage and Utilisation of Greenhouse Gases, *Waste Management*, **17**, No. 5/6, 281-287, 1997

Gaz de France, The 2004 results: budget and research projects, pp1, 2005,  
<http://www.gazdefrance.com/public/page.php?iddossier=849&idarticle=2211>

Geipel H., T. Rüggeberg, H. Markus, H. Höwener, U. Schlagheck, J. Seier, and P. Markewitz, COORETEC — CO<sub>2</sub>-Reduktions-Technologien, Forschungs- und Entwicklungskonzept für emissionsarme fossil befeuerte Kraftwerke, Bundesministerium für Wirtschaft und Arbeit, Referat Kommunikation und Internet (LP4), Kurzfassung, Bonn, pp 15, April 30, 2003a,  
<http://www.cooretec.de/datapool/page/1329/kurzfassung.pdf>

Geipel H., T. Rüggeberg, H. Markus, H. Höwener, U. Schlagheck, J. Seier, and P. Markewitz, COORETEC — CO<sub>2</sub>-Reduktions-Technologien, Forschungs- und Entwicklungskonzept für emissionsarme fossil befeuerte Kraftwerke, Bericht der COORETEC-Arbeitsgruppen, Bundesministerium für Wirtschaft und Arbeit, Referat Kommunikation und Internet (LP4) - ISSN 0342 — 9288 (BMWA-Dokumentation), Nr.: 527, Kurz- und Langfassung, pp 109, Bonn, Dezember 2003b,  
<http://www.fz-juelich.de/ptj/projekte/datapool/page/1329/doku527.pdf>

Hashimoto, K., H. Habazaki, M. Yamasaki, S. Meguro, T. Sasaki, H. Katagiri, T. Matsui, K. Fujimura, K. Izumiya, N. Kumagai, and E. Akiyama, Advanced materials for global carbon dioxide recycling, *Materials Science and Engineering*, **A304-306**, 88-96, 2001

Hoffert, M. I., K. Caldeira, A. K. Jain, E. F. Haites, L. D. D. Harveyk, S. D. Potter, M. E. Schlesinger, S. H. Schneider, R. G. Watts, T. M. L. Wigley, and D. J. Wuebbles, Energy implications of future stabilization of atmospheric CO<sub>2</sub> content, *Nature*, **395**, 881-884, 1998

Hoth, P. E. F., A. Seibt, T. Kellner, and E. Hünges, Geothermie Report 97-1: Geowissenschaftliche Bewertungsgrundlagen zur Nutzung hydrogeothermaler Ressourcen in Norddeutschland, it Geo-forschungszentrum Potsdam Scientifical Technical Report STR97/15, pp 150, 1998, <http://www.gfz-potsdam.de/bib/pub/str9715/9715.htm>

Hoth, P. E. F., Mingram B., and L'uders V., New Indications for the Genesis and Migration of Nitrogen-rich Gases in Northern Germany — Fluid Inclusion and Nitrogen Geochemistry Studies of Permo-Carboniferous Rocks, AAPG Annual Meeting 2003: Energy - Our Monumental Task, May 9, 2003 — May 14, 2003, Salt Lake City, Utah,  
[http://aapg.confex.com/aapg/sl2003/techprogram/paper\\_77577.htm](http://aapg.confex.com/aapg/sl2003/techprogram/paper_77577.htm)

Islam, R., S. Huang, Q. Malik, and M. Dong, Potential of Greenhouse Gas Storage and Utilization through Enhanced Oil Recovery, Final Report, Petroleum Technology Research Centren (PTRC), Canada, pp 181, September 1999

Jimenez, J. A. and R. J. Chalaturnyk, Are disused Hydrocarbon Reservoirs safe for Geological Storage of CO<sub>2</sub>? Sixth International Conference on Greenhouse Gas Control Technologies, GHGT-6, October 1 – 4, 2002,  
<http://www.rite.or.jp/GHGT6/pdf/G1-1.pdf>

Johnston, P. and D. Santillo, Carbon Capture and Sequestration: Potential Environmental Impacts Intergovernmental Panel on Climate Change (IPCC) , Workshop for Carbon Capture and Storage, Regina, Canada, pp 16, November 18 – 21, 2002,  
<ftp://ftp.ecn.nl/pub/www/library/conf/ipcc02/ccs02-07.pdf>

Khoklov, K., 35 Jahre Erdgasförderung aus der Altmark — Produktionssicherung in der späten Abbauphase, presentation at DGMK-Frühjahrstagung, 2004

King, A. D., Climate Change Science: Adapt, Mitigate, or Ignore?, *Science*, **303**, 176-177, January 9, 2004,  
<http://www.sciencemag.org/cgi/reprint/303/5655/176.pdf>

Kleditzsch, O., Beiträge zur Genese, Lithostratigraphie, Petrographie sowie Petrophysik sandiger Klastika des tieferen Oberrotliegenden (II) der Altmark und benachbarter Regionen, submitted PhD-thesis, TU Bergakademie Freiberg, Germany, 2003

Kossow, D., Die kinematische Entwicklung des invertierten intrakontinentalen Norddeutschen Beckens — Ergebnisse seismisch-stratigraphischer Untersuchungen und einer Profilbilanzierung, PhD Thesis, University of Potsdam, pp 123, March 2001,  
<http://www.gfz-potsdam.de/bib/pub/str0204/0204.pdf>

Krull, P. Bundesanstalt für Geowissenschaften und Rohstoffe, Hannover, Germany, pers. communication, 2003

Laherrére, J., Distribution and evolution of 'recovery factor', International Energy Agency, Oil reserves conference, November 11, 1997,  
<http://www.dieoff.org/page183.pdf>

May, F., Bundesanstalt für Geowissenschaften und Rohstoffe, Hannover, Germany, pers. communication, 2002

May, F., J. P. Gerling, and P. Krull, Underground storage of CO<sub>2</sub>, pp 10, 2002,  
[http://www.bgr.de/b123/at\\_co2\\_storage/co2\\_storage.htm](http://www.bgr.de/b123/at_co2_storage/co2_storage.htm)  
publ. in german: Untertagespeicherung von CO<sub>2</sub>, *VGB Power Tech*, **82**, No. 8, 45-50, 2002

May, F., P. Krull, and J. P. Gerling, GESTCO final report, Work Package 4, Storage Scenarios in North Germany, pp 47, 2003

Müller, E. P., H. Dubslaff, W. Eiserbeck, and R. Sallum, Zur Entwicklung der Erdöl- und Erdgas-exploration zwischen Ostsee und Thüringer Wald; in: Müller, P. E., and H. Porth (Eds.), Perm im Ostteil der Norddeutschen Senke, *Geologisches Jahrbuch A*, **A131**, pp 5, 1993

Obdam, A., L. G. H. Van der Meer, F. May, C. Kervevan, N. Bech, and A. F. B. Wildenborg, Effective CO<sub>2</sub> Storage Capacity in Aquifers, Gas Fields, Oil Fields and Coal Fields, Proceedings of the Sixth International Conference on Greenhouse Gas Control Technologies (GHGT-6), Kyoto, Japan, pp 6, October 1 – 4, 2002,  
<http://www.rite.or.jp/GHGT6/pdf/B1-6.pdf>

Oldenburg, C. M., K. Pruess, and S. M. Benson, Process Modeling of CO<sub>2</sub> Injection into Natural Gas Reservoirs for Carbon Sequestration and Enhanced Gas Recovery, *Energy & Fuels*, **15**, 293-298, 2001,  
[http://esd.lbl.gov/GEOSEQ/pdf/oldenburg\\_enfuels.pdf](http://esd.lbl.gov/GEOSEQ/pdf/oldenburg_enfuels.pdf)

Oldenburg, C. M. and A. J. A. Unger, On leakage and seepage from geologic carbon sequestration sites: unsaturated zone attenuation, *Vadose Zone Journal*, **2**, 287-296, 2003  
<http://www-library.lbl.gov/docs/LBNL/519/28/PDF/LBNL-51928.pdf>

Oldenburg, C. M., S. H. Stevens, and S. M. Benson, Economic feasibility of carbon sequestration with enhanced gas recovery (CSEGR), *Energy*, **29**, 1413-1422, 2004a  
[http://www-esd.lbl.gov/GEOSEQ/pdf/oldenburg\\_etal138.pdf](http://www-esd.lbl.gov/GEOSEQ/pdf/oldenburg_etal138.pdf)

Oldenburg, C. M., G. J. Moridis, N. Spycher, and K. Pruess, EOS7C Version 1.0: TOUGH2 module for carbon dioxide or nitrogen in natural gas (methane) reservoirs, *Lawrence Berkeley National Laboratory Report*, LBNL-56589, 2004b  
<http://www-library.lbl.gov/docs/LBNL/565/89/PDF/LBNL-56589.pdf>

Pasternak, M., M. Kosinowski, J. Loesch, J. Messner, and R. Sedlacek, Erdöl und Erdgas in der Bundesrepublik Deutschland 2001, Niedersächsisches Landesamt für Bodenforschung (NLfB, Geological Survey of Lower Saxony), Hannover, pp 62, 2001,  
[http://www.nlfb.de/rohstoffe/downloads/jahresbericht\\_2001.pdf](http://www.nlfb.de/rohstoffe/downloads/jahresbericht_2001.pdf)

Peng, D. Y. and D. B. Robinson, A New Two Constant Equation of State, *Ind. Eng. Chem. Fund.*, **15**, 59-64, 1976

Plein, E., Bemerkungen zum Ablauf der paläontologischen Entwicklung des Stefan und Rotliegend des Norddeutschen Beckens, *Geolog. Jb.*, **A 131**, 99–116, 1993

Pruess, K., C. Oldenburg, and G. Moridis, TOUGH2 User's Guide, Version 2.0, *Lawrence Berkeley National Laboratory Report*, LBNL-43134, Berkeley, CA, pp 210, November 1999

Pruess, K., Numerical Simulations of Fluid Leakage from a Geologic Disposal Reservoir for CO<sub>2</sub>, Proceedings, TOUGH Symposium 2003, Lawrence Berkeley National Laboratory, Berkeley, pp 8, May 12 – 14, 2003,  
<http://www-esd.lbl.gov/TOUGHsymposium/pdfs/Pruess.pdf>

Pruess, K., Numerical Simulations of Fluid Leakage from a Geological Disposal Reservoir for CO<sub>2</sub>, 2<sup>nd</sup> Symposium Dynamics of Fluids in Fractured Rock, Lawrence Berkeley National Laboratory Report, February 10-12, 2004, Berkeley

Rebscher, D. and F. May, Numerical simulations of CO<sub>2</sub> enhanced gas recovery in mature Rotliegend gas fields, DGMK-Tagungsbericht 2004-2, 109-117, ISBN 3-936418-17-9, 2004

Rebscher, D., F. May, and C. M. Oldenburg, CO<sub>2</sub> Injection in the Altmark Natural Gas Field, Germany: Simulations of Water Injection to Delay CO<sub>2</sub> Breakthrough, 3<sup>rd</sup> Annual Conference on Carbon Sequestration, Alexandria, VA, May 3 – 6, 2004,  
<http://www.carbonsq.com>

Reid, R. C., J. M. Prausnitz, and B. E. Poling, The Properties of Gases & Liquids, 4th Edition, McGraw Hill, 1987

Ribbeck, H., Natural Gas Storage Project at Peckensen, Germany - Part 1, Spring 2001 Technical Class, Orlando, Florida, USA, April 22, 2001,  
<http://www.solutionmining.org/M01S/Ribbeck%20-%20M01S%20Meeting%20Paper.pdf>

Riemer, P., Greenhouse Gas Mitigation Technologies, an Overview of the CO<sub>2</sub> Capture, Storage and Future Activities of the IEA Greenhouse Gas R&D Programme, *Energy Convers. Mgmt*, **37**, No. 6-8, 665-670, 1996

Scheck, M. and U. Bayer, Evolution of the Northeast German Basin — inferences from a 3D structural model and subsidence analysis, *Tectonophysics*, **313**, 145-169, 1999

Schumacher, K. H. and F. May, Trends der Verteilung fallen- und lagerstättengenetischer Parameter im Erdgaslagerstättengebiet der Westaltmark, *Erdöl, Erdgas, Kohle*, **106**, No. 6, 243-246, 1990

Sedlacek, R., Untertage-Erdgasspeicherung in Deutschland — Underground Gas Storage in Germany, *Erdöl Erdgas Kohle*, **118**, No. 11, 498-504, November 2002

Stevens, S. H., V. K. Kuuskraa, and J. Gale, Sequestration of CO<sub>2</sub> in Depleted Oil and Gas Fields: Global Capacity and Barriers to Overcome, Fifth International Conference on Greenhouse Gas Control Technologies, Cairns, Australia, pp 6, August 13 – 16, 2000,  
<http://www.ieagreen.org.uk/GHGT5-11.pdf>

Stoll, A., Forschungsaufgabe 'Strukturentwicklung Mitteldeutsche Hauptabbrüche und Südrand Norddeutsch-Polnische Senke', Themen-Nr. 5.07.2019, Zur Feinstruktur des Saxons der westlichen Altmark unter besonderer Berücksichtigung einer N-S-Traverse (Gebiet Salzwedel — Gebiet Mellin), Akademie der Wissenschaften der DDR, Zentralinstitut für Physik der Erde (ZIPE), Bereich Geologie, Berlin, pp 38, April 25, 1981

Stottmeister, L., et al. (Eds.), 66. Tagung der Arbeitsgemeinschaft Nordwestdeutscher Geologen, Salzwedel, Germany, pp 85, May 25 – 28, 1999

United Nations Framework Convention on Climate Change (UNFCCC), Kyoto Protocol to the United Nations Framework Convention on Climate Change, Kyoto, Japan, pp 33, December 11, 1997,  
<http://unfccc.int/resource/docs/convkp/kpeng.pdf>

U.S. Department of Energy, Office of Science, Office of Fossil Energy, Carbon Sequestration Research and Development, A 1999 Report by DOE's Office of Fossil Energy and Office of Science, pp 272, December 1999,  
[http://fossil.energy.gov:7778/programs/sequestration/publications/1999\\_rdreport/](http://fossil.energy.gov:7778/programs/sequestration/publications/1999_rdreport/)

U. S. Department of Energy, Country Analysis Briefs, Germany: Environmental Issues, pp 5, September 2003,  
<http://www.eia.doe.gov/emeu/cabs/germe.pdf>

Vattenfall Europe AG (VEAG), Das Kraftwerk Schwarze Pumpe, pp 1, 2005,  
[http://www.vattenfall.de/www/vattenfall/vattenfall\\_de/Unternehmen/Geschxftsfelder/Kraftwerke/Braunkohle/SchwarzexPumpe/index.jsp](http://www.vattenfall.de/www/vattenfall/vattenfall_de/Unternehmen/Geschxftsfelder/Kraftwerke/Braunkohle/SchwarzexPumpe/index.jsp)

Wagner, M., H.-J. Rasch, J. Piske, and B. Ziran, Mikrobielle Prospektion auf Erdöl und Erdgas in Ostdeutschland, *Geolog. Jb.*, **A 149**, 287–309, 1998,  
<http://www.microporlabs.de/jahrbuch.pdf>

Welfens, P. J. J., B. Meyer, W. Pfaffenberger, P. Jasinski, and A. Jungmittag, (Ed. P. Palinkas), Towards a re-orientation of national energy policies in the EU? — Germany as a case study, *European Parliament, Energy and Research Series*, ENER - 110 EN, pp 123, November 1999,  
[http://www.europarl.eu.int/workingpapers/ener/pdf/110\\_en.pdf](http://www.europarl.eu.int/workingpapers/ener/pdf/110_en.pdf)

Wendel, H., W. Lohr, K.-J. Twarok, and K. Khoklov, 35 Jahre Erdgasförderung aus der Altmark — Produktionssicherung in der späten Abbauphase, DGMK-Tagungsbericht 2004-2, ISBN 3-936418-17-9, pp 47-55, 2004

White, C. M., B. R. Strazisar, E. J. Granite, J. S. Hoffman, and H. W. Pennline, Separation and capture of CO<sub>2</sub> from large stationary sources and sequestration in geological formations — Coalbeds and deep saline aquifers [Review], *Journal of the Air & Waste Management Association*, **53**, No. 6, 645-715, June 2003

Ybema, J. R., P. Lako, I. Kok, E. Schol, D. J. Gielen, and T. Kram, Scenarios for Western Europe on long term Abatement of CO<sub>2</sub> Emissions, The Netherlands Energy Research Foundation ECN, ECN-C-97-051, pp 111, December 1997,  
<http://www.ecn.nl/docs/library/report/1997/c97051.pdf>

Zazovsky, A., CO<sub>2</sub> Flooding Fundamentals, Lawrence Berkeley National Laboratory, Earth Science Division, Reservoir Engineering Group Seminar, February 13, 2004

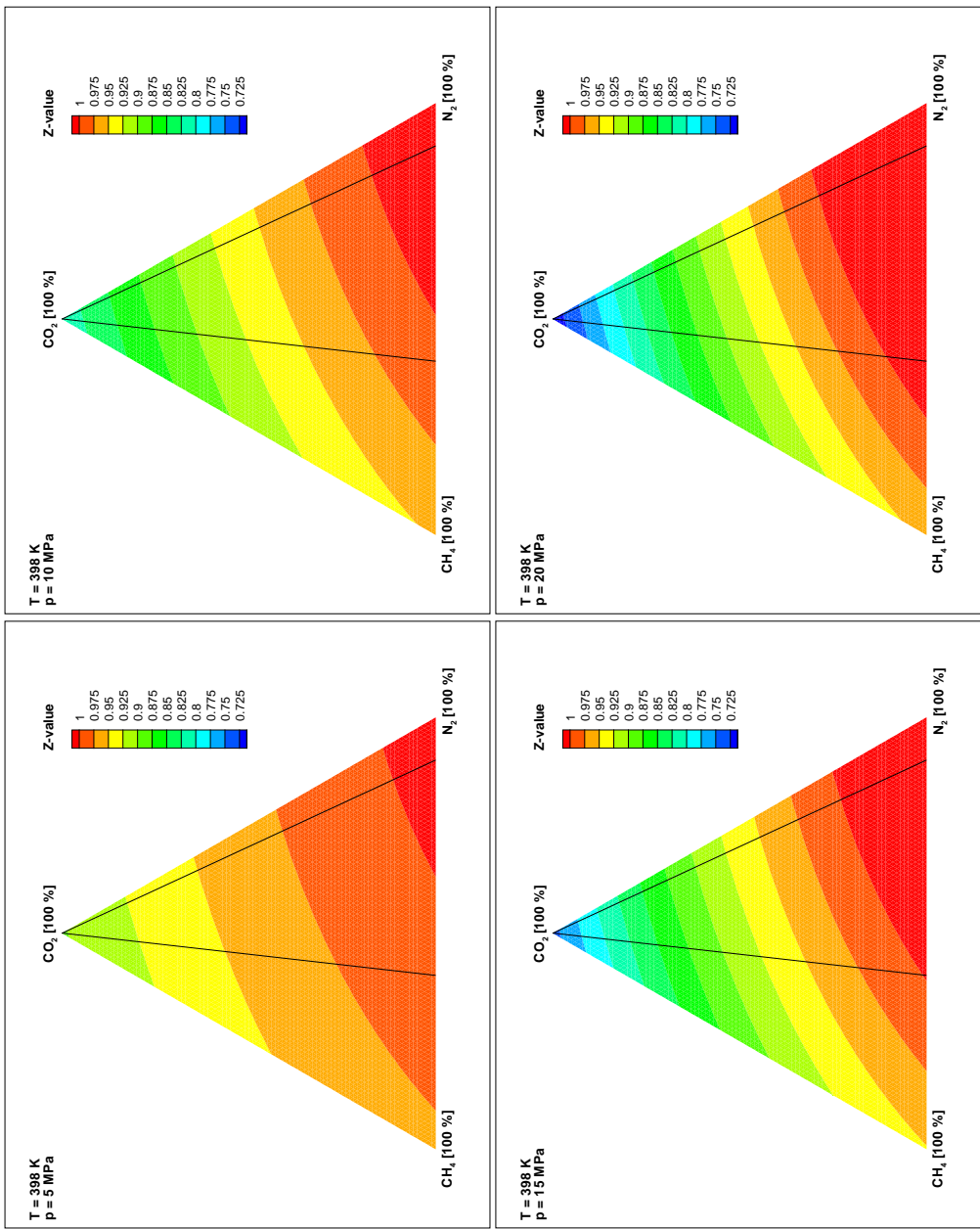


Figure 16: Compressibility-factor  $Z$  obtained for varying gas mixtures in the ternary system  $CH_4\text{-}CO_2\text{-}N_2$  documents a higher range under higher pressures. The contour levels are identical for a better comparison of the four different pressure cases. The two black lines indicate the conditions of the Altmark area (10).

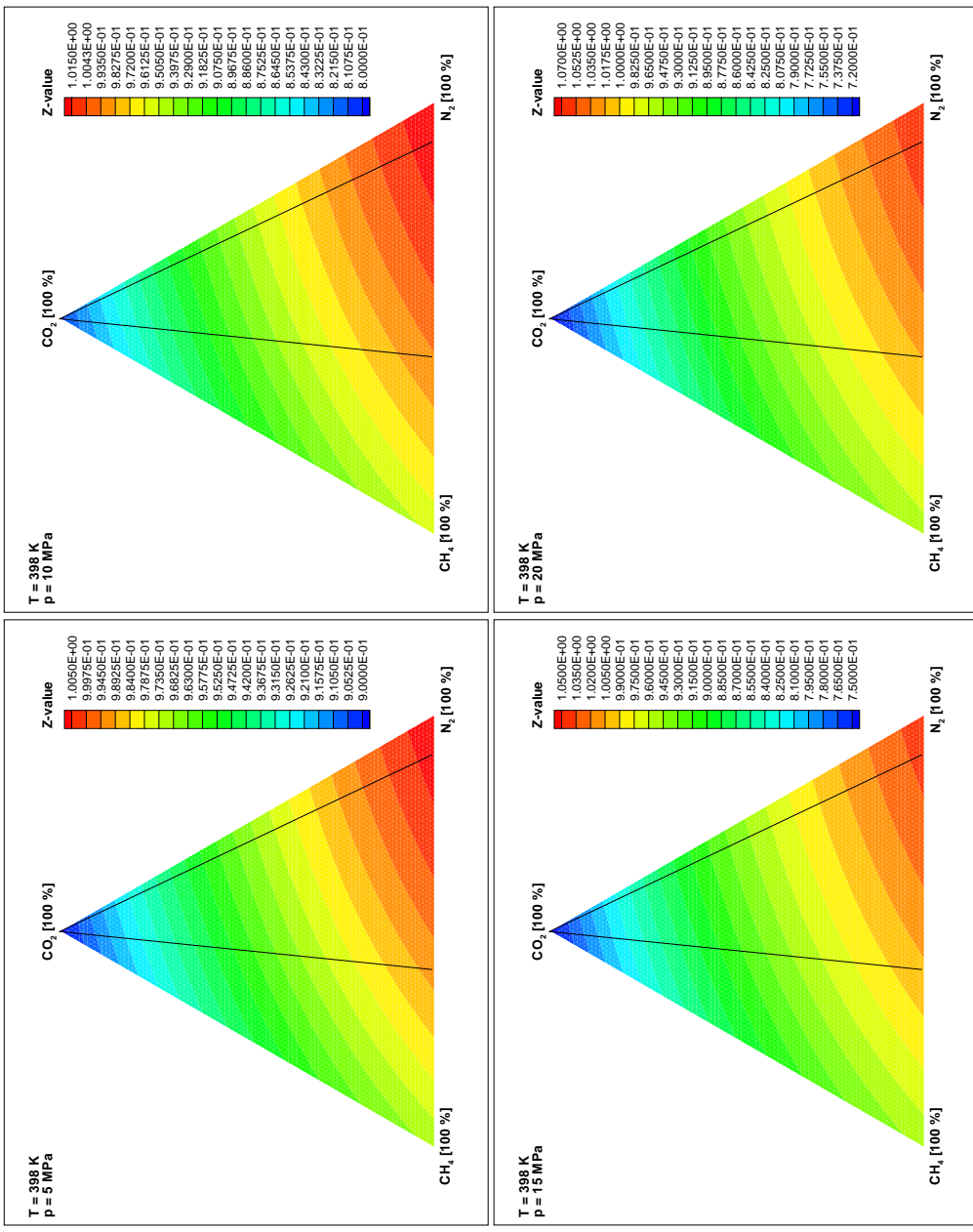


Figure 17: Compressibility-factor  $Z$  obtained for varying gas mixtures in the ternary system  $\text{CH}_4\text{-}\text{CO}_2\text{-}\text{N}_2$  differs within about 10 %, to 30 %, for the specific pressure values. The data are the same as in Figure 18, but the contour levels are optimized for each of the four different pressure values. The two black lines indicate the conditions of the Altmark area (10).

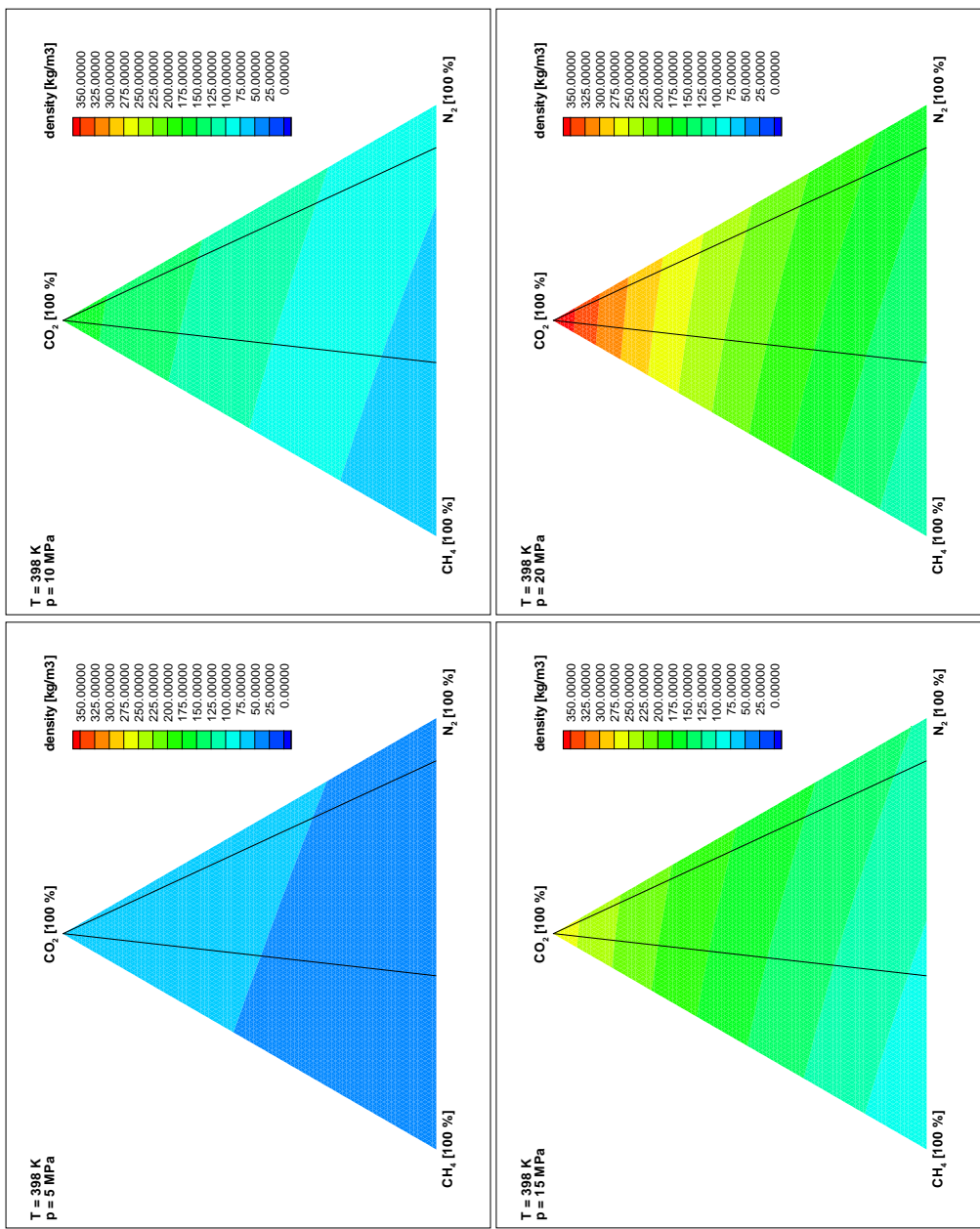


Figure 18: Density  $\rho$  for varying gas mixtures in the ternary system  $\text{CH}_4\text{-}\text{CO}_2\text{-}\text{N}_2$  documents higher values under higher pressures. The contour levels are identical for a better comparison of the four different pressure cases. The two black lines indicate the conditions of the Altmark area (10).

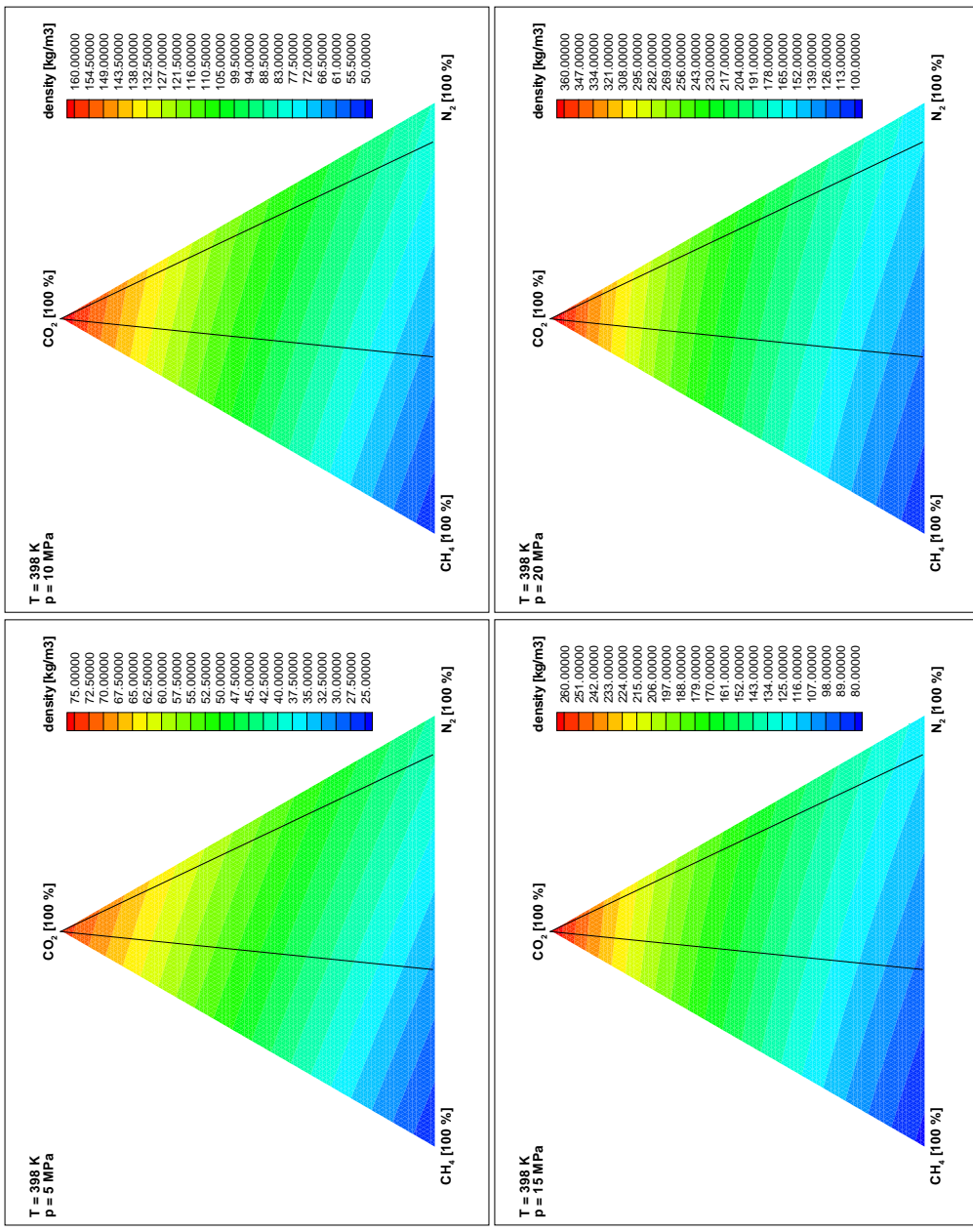


Figure 19: Density  $\rho$  for varying gas mixtures in the ternary system obtained for varying gas mixtures in the ternary system  $\text{CO}_2\text{-N}_2\text{-CH}_4$ - $\text{CO}_2$ - $\text{N}_2$  differs within a factor of about three. The data is the same as in Figure 18, but the contour levels are optimized for each of the four different pressure values. The two black lines indicate the conditions of the Altmark area (10).

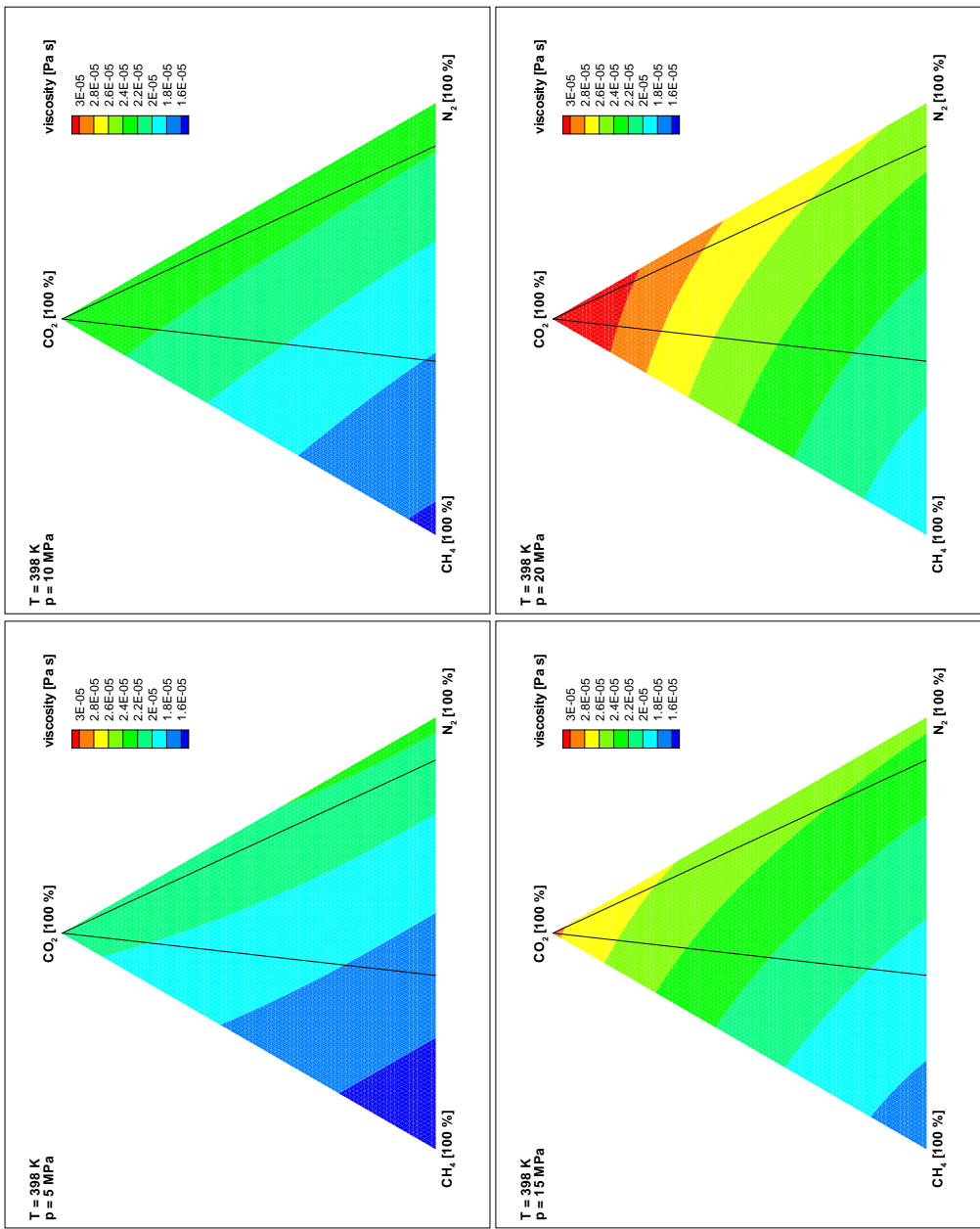


Figure 20: The viscosity  $\mu$  for varying gas mixtures in the ternary system  $CH_4$ - $CO_2$ - $N_2$  documents higher values under higher pressures. The contour levels are identical for a better comparison of the four different pressure cases. The two black lines indicate the conditions of the Altmark area (10).

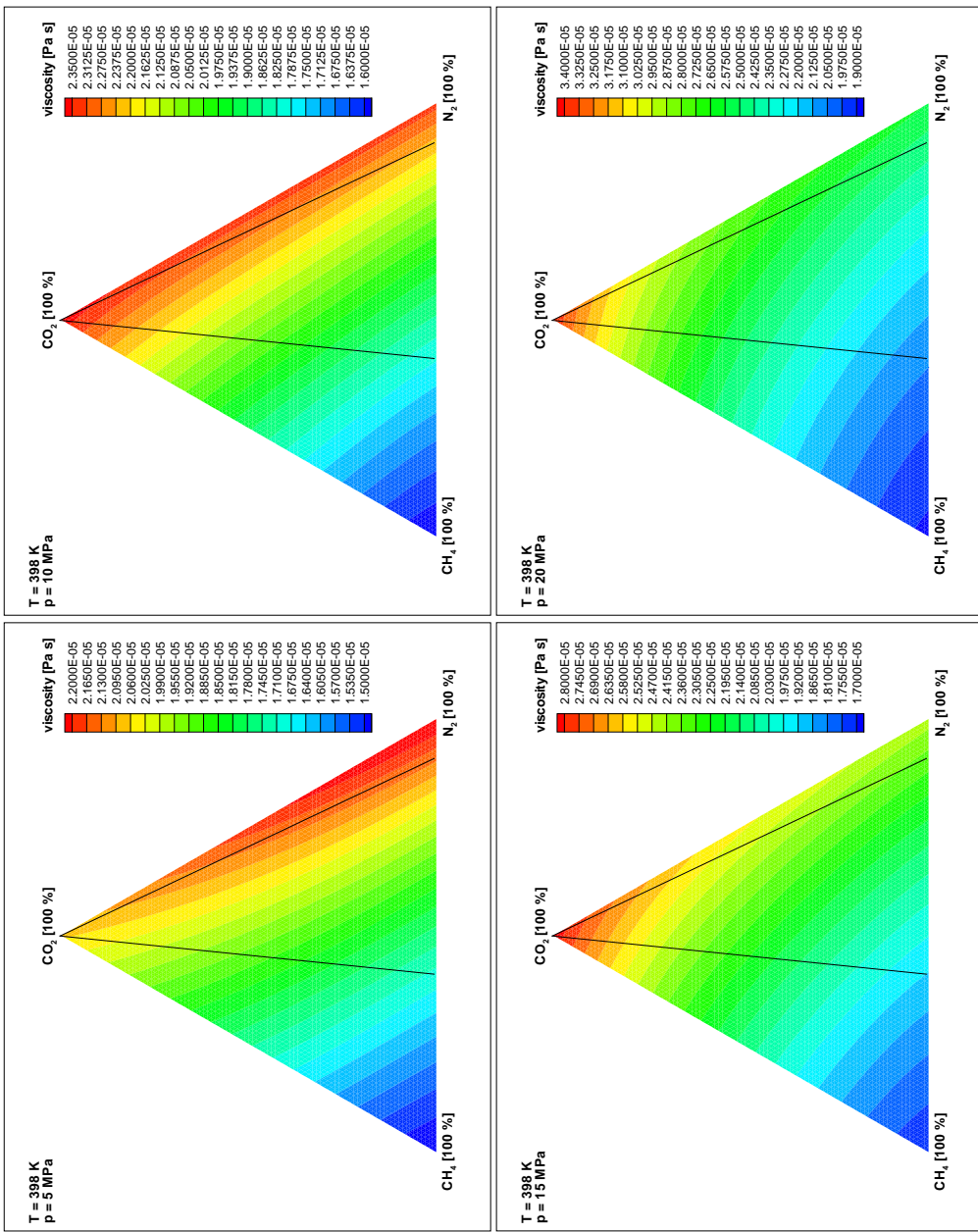


Figure 21: Viscosities  $\mu$  obtained for varying gas mixtures in the ternary system  $\text{CH}_4$ - $\text{CO}_2$ - $\text{N}_2$  differs within about 50 %, ascending with higher pressures. The data is the same as in Figure 20, but the contour levels are optimized for each of the four different pressure values. The two black lines indicate the conditions of the Altmark area (10).

## 2D simulation - CH<sub>4</sub> extraction and CO<sub>2</sub> injection

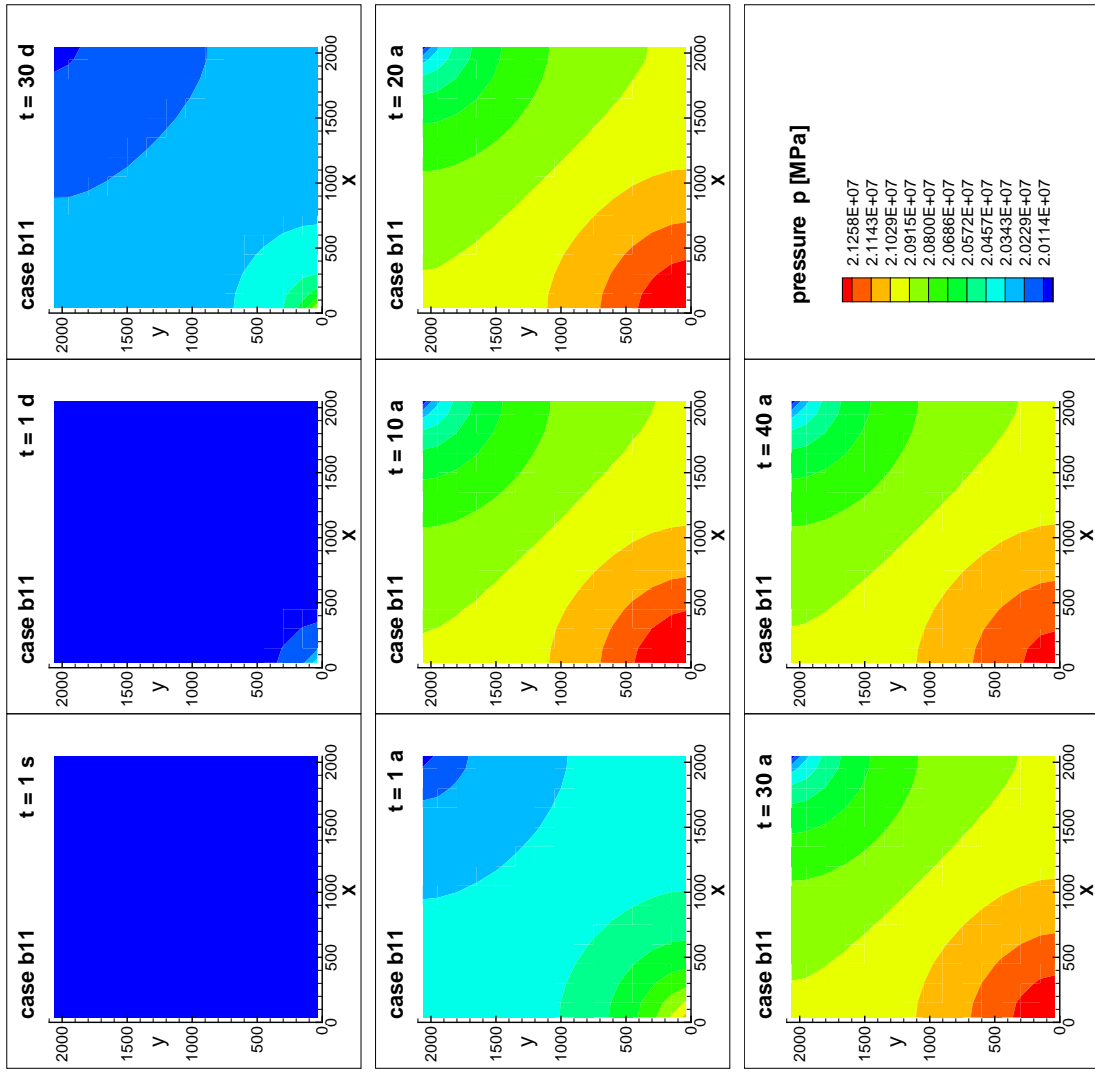


Figure 22: The time-dependent pressure distribution in the 2D simulation of the high-permeability layer Z9–11 presents the increase within the first years of CO<sub>2</sub> injection and the unchanged high distribution till the end of the injection period of 40 years. The total injection rates are 0.0178 kg/s for Case b1 to Case b7 and 2.9091 kg/s for Case b7 to Case b11.

## 2D simulation - CH<sub>4</sub> extraction and CO<sub>2</sub> injection

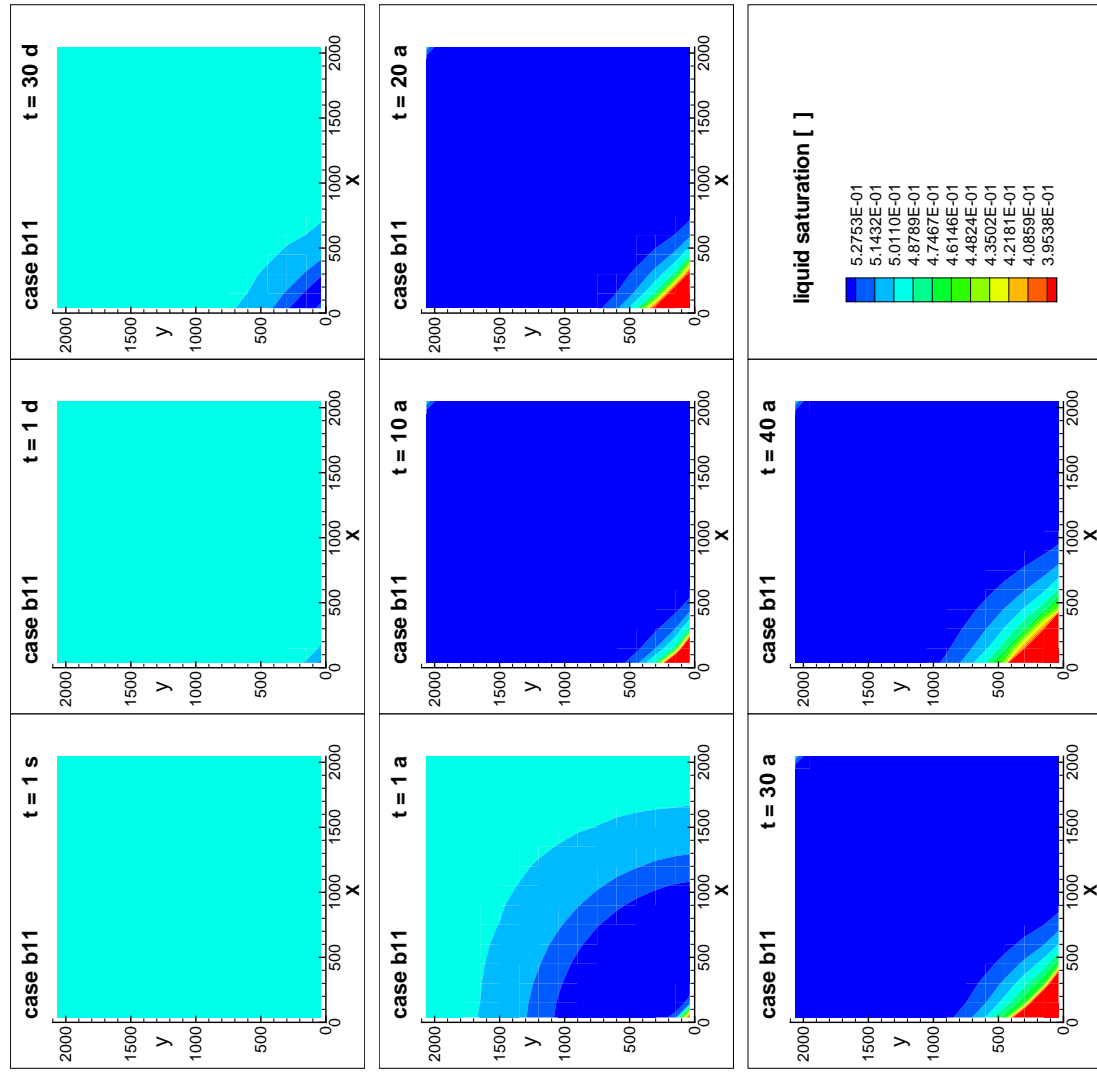


Figure 23: The time-dependent saturation distribution in the 2D simulation of the high-permeability layer Z9–11 illustrates the increase within the first years of CO<sub>2</sub> injection and the reduced saturation around the injection site with time in the last decades of the 40 years injection period. The total injection rates are 0.0178 kg/s for Case b1 to Case b6 and 2.9091 kg/s for Case b7 to Case b11.

## 2D simulation - CH<sub>4</sub> extraction and CO<sub>2</sub> injection

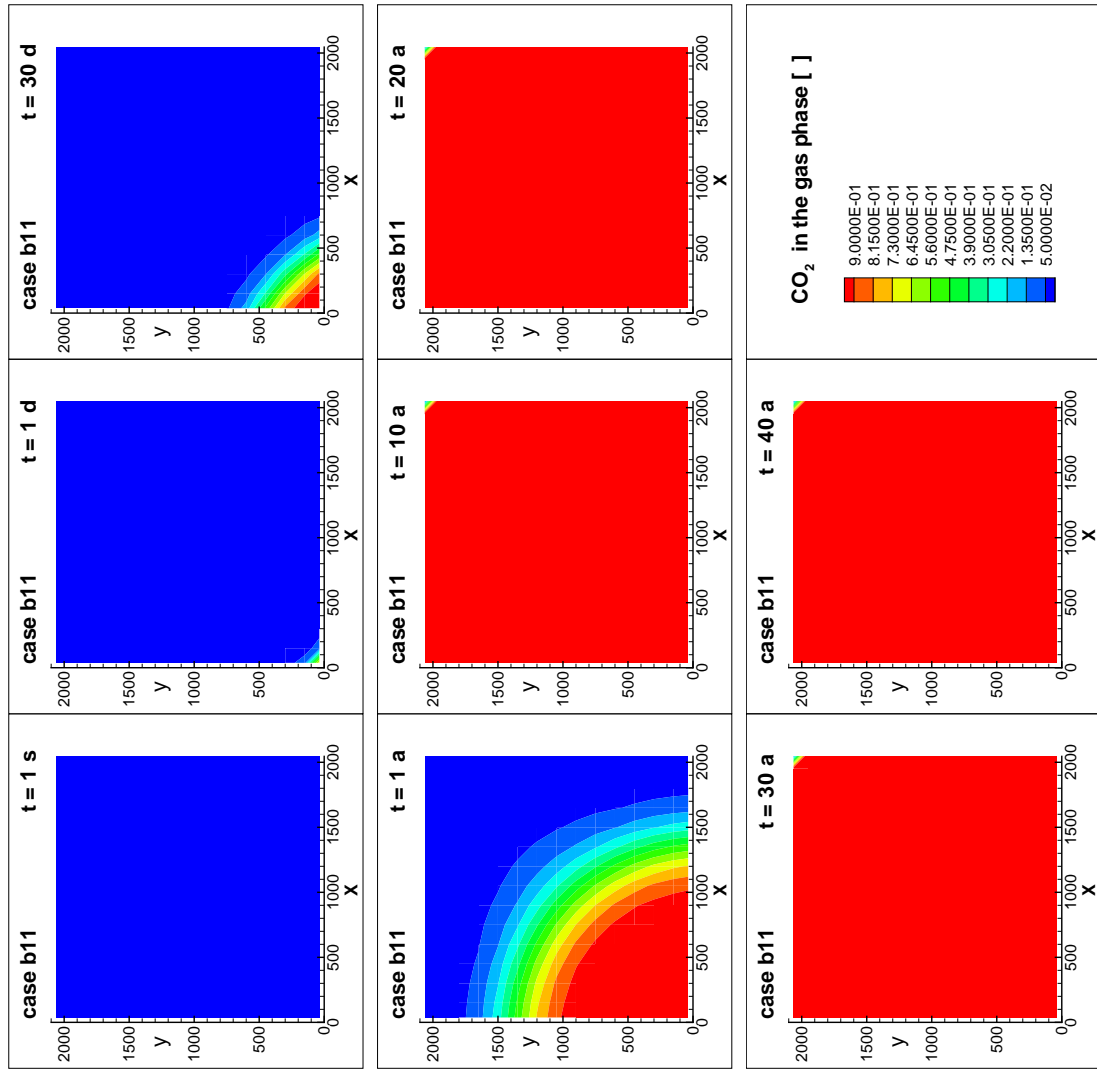


Figure 24: The time-dependent distribution of the CO<sub>2</sub> mass fraction in the gas phase in the 2D simulation of the high-permeability layer Z9–11 documents the radial spreading from the injection site to the production well. The total injection rates are 0.0178 kg/s for Case b1 to Case b6 and 2.9091 kg/s for Case b7 to Case b11.

## 2D simulation - CH<sub>4</sub> extraction and CO<sub>2</sub> injection

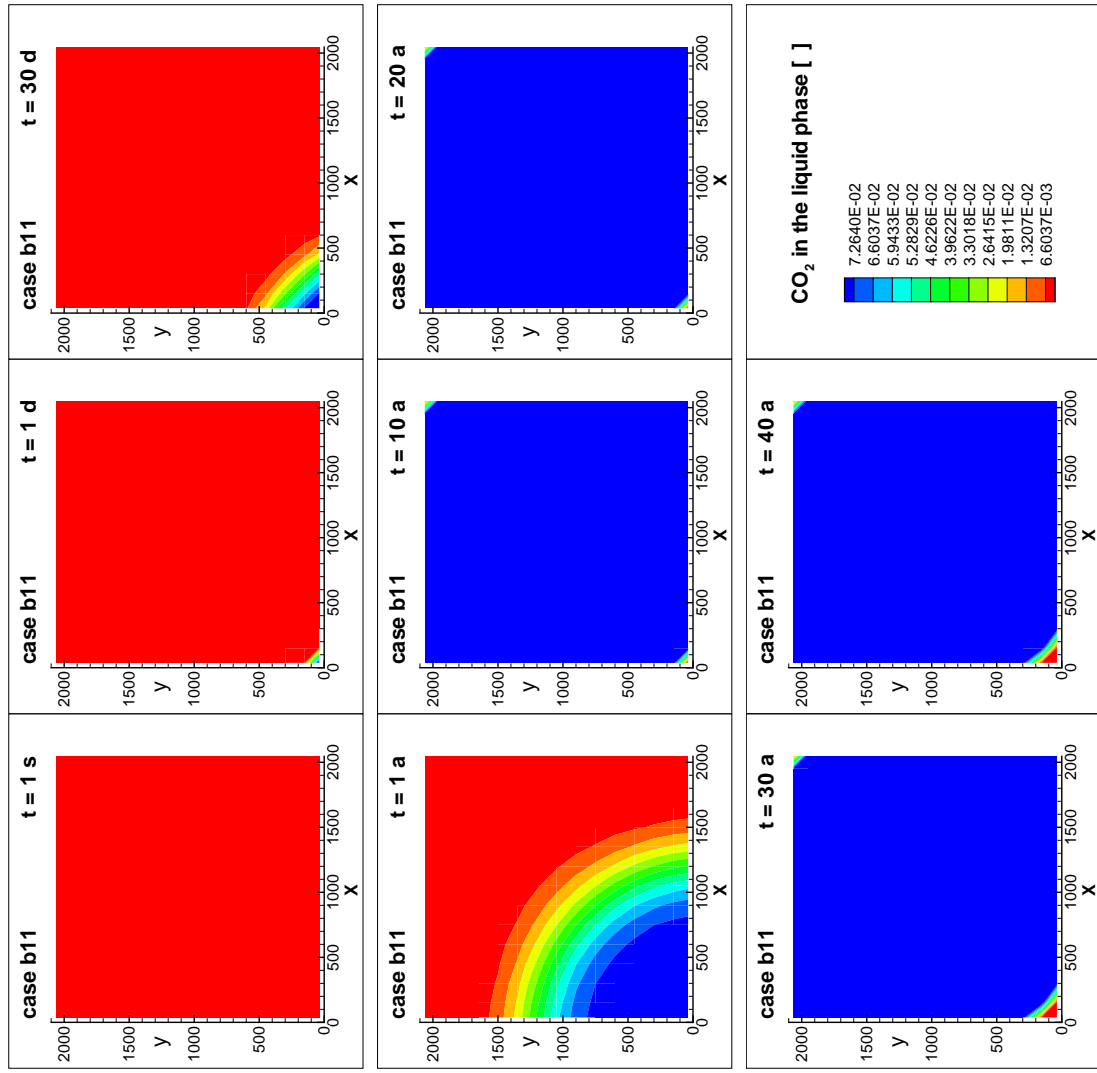


Figure 25: The time-dependent distribution of the CO<sub>2</sub> mass fraction in the liquid phase in the 2D simulation of the high-permeability layer Z9–11 documents the radial spreading from the injection site to the production site to the production well, showing lower values than in the gas phase. The total injection rates are 0.0178 kg/s for Case b6 and 2.9091 kg/s for Case b7 to Case b11.

## 2D simulation - $\text{CH}_4$ extraction and $\text{CO}_2$ injection

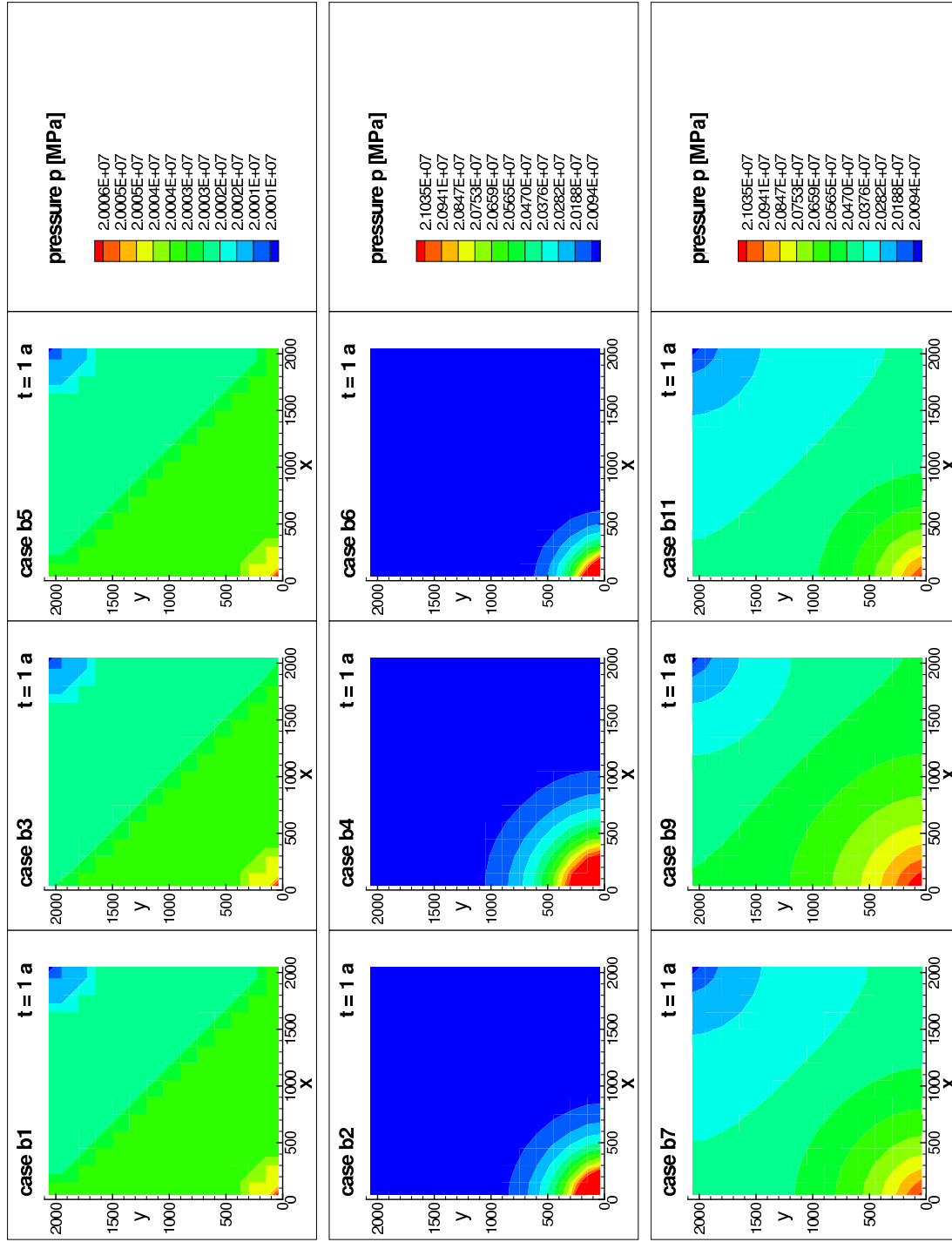


Figure 26: The time-dependent pressure distribution after 1 year in the different 2D simulations documents the higher values for the simulations with smaller porosities or higher injection rates, and the larger radius of influence due to higher permeabilities. The main characteristics of the different cases are listed in the Tables 5 and 6. The total injection rates are 0.0178 kg/s for Case b1 to Case b6 and 2.9091 kg/s for Case b7 to Case b11.

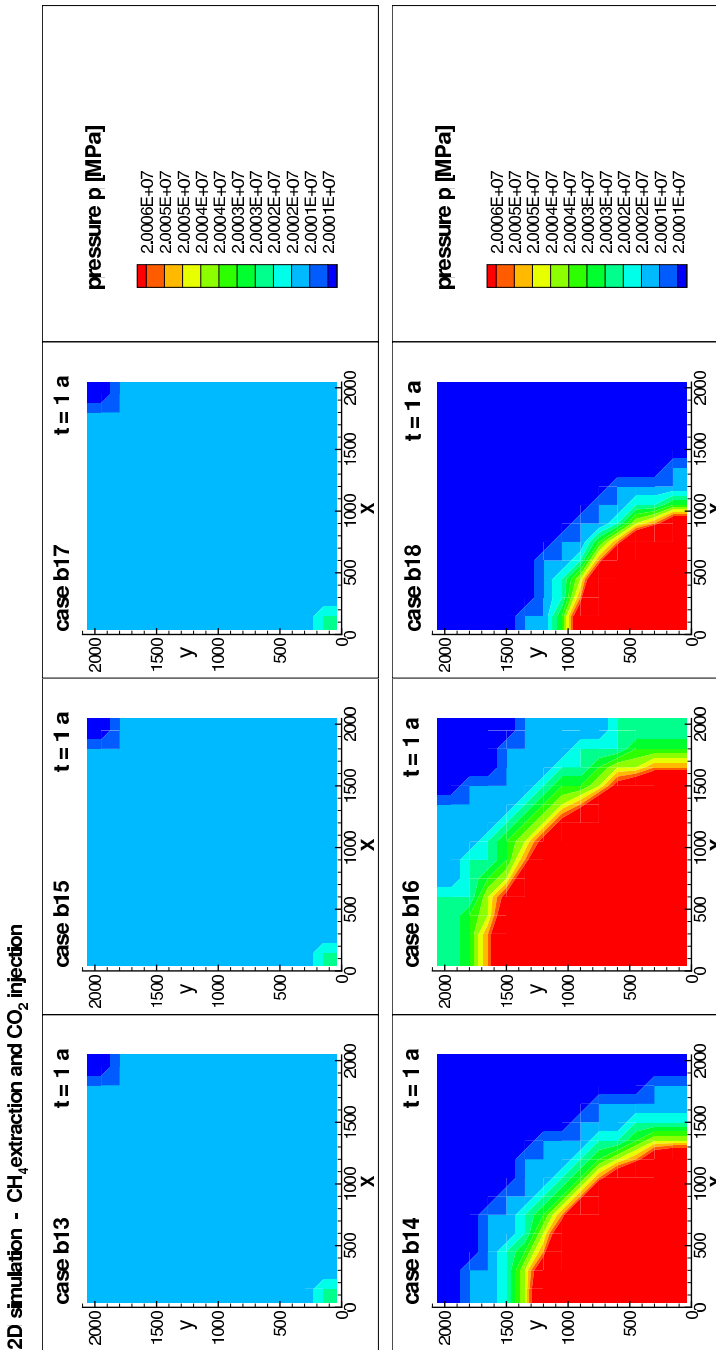


Figure 27: The time-dependent pressure distribution after 1 year in the different 2D simulations documents the higher values for the simulations with smaller porosities, and the larger radius of influence due to higher permeabilities. The main characteristics of the different cases are listed in Table 7. The total injection rates are 0.0068 kg/s for Case b13 to Case b18.

## 2D simulation - $\text{CH}_4$ extraction and $\text{CO}_2$ injection

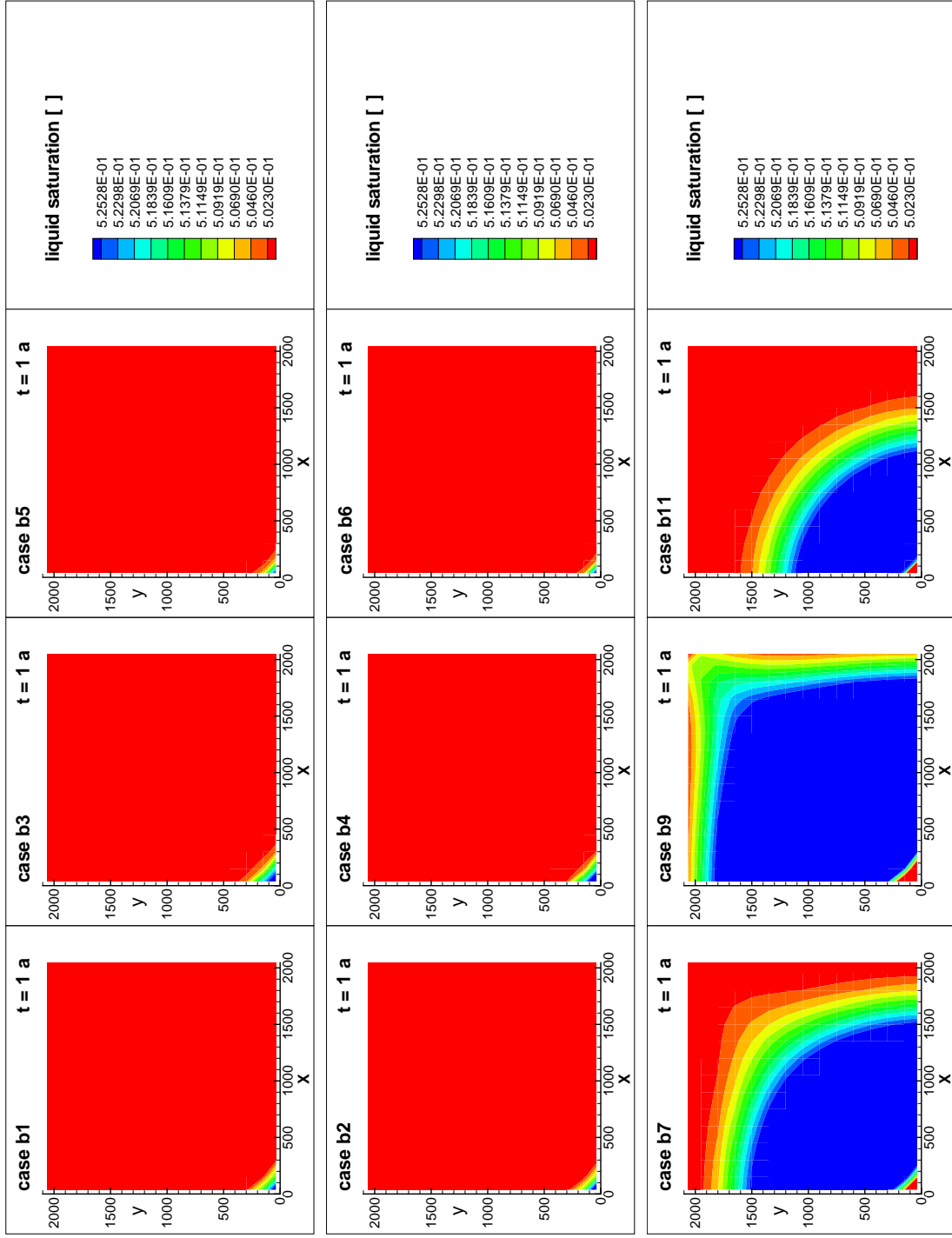
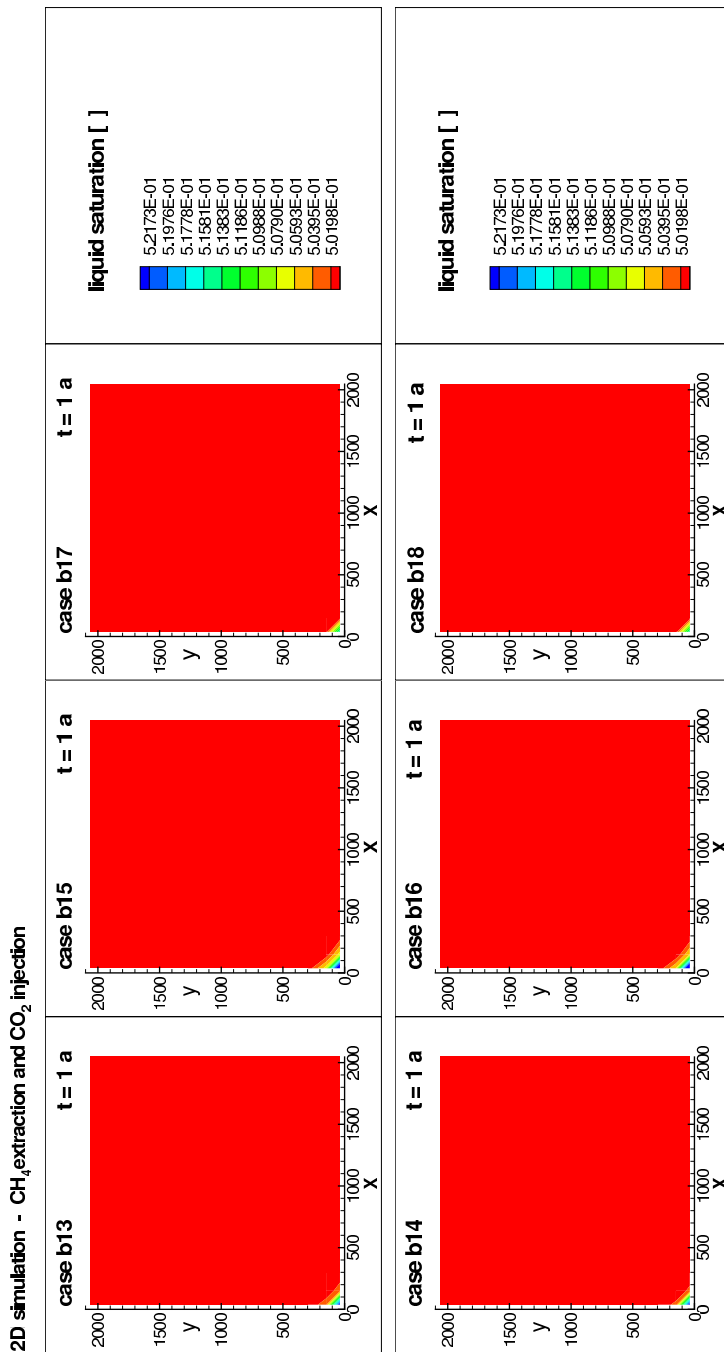


Figure 28: The time-dependent distribution of the liquid saturation after 1 year in the different 2D simulations illustrates the higher values for the simulations with smaller porosities and higher injection rates. The main characteristics of the different cases are listed in the Tables 5 and 6. The total injection rates are 0.0178 kg/s for Case b6 and 2.9091 kg/s for Case b7 to Case b11.



*Figure 29: The time-dependent distribution of the liquid saturation after 1 year in the different 2D simulations illustrates the higher values for the simulations with smaller porosities, compare with Figure 28. The main characteristics of the different cases are listed in Table 7. The total injection rates are 0.0068 kg/s for Case b13 to Case b18.*

## 2D simulation - $\text{CH}_4$ extraction and $\text{CO}_2$ injection

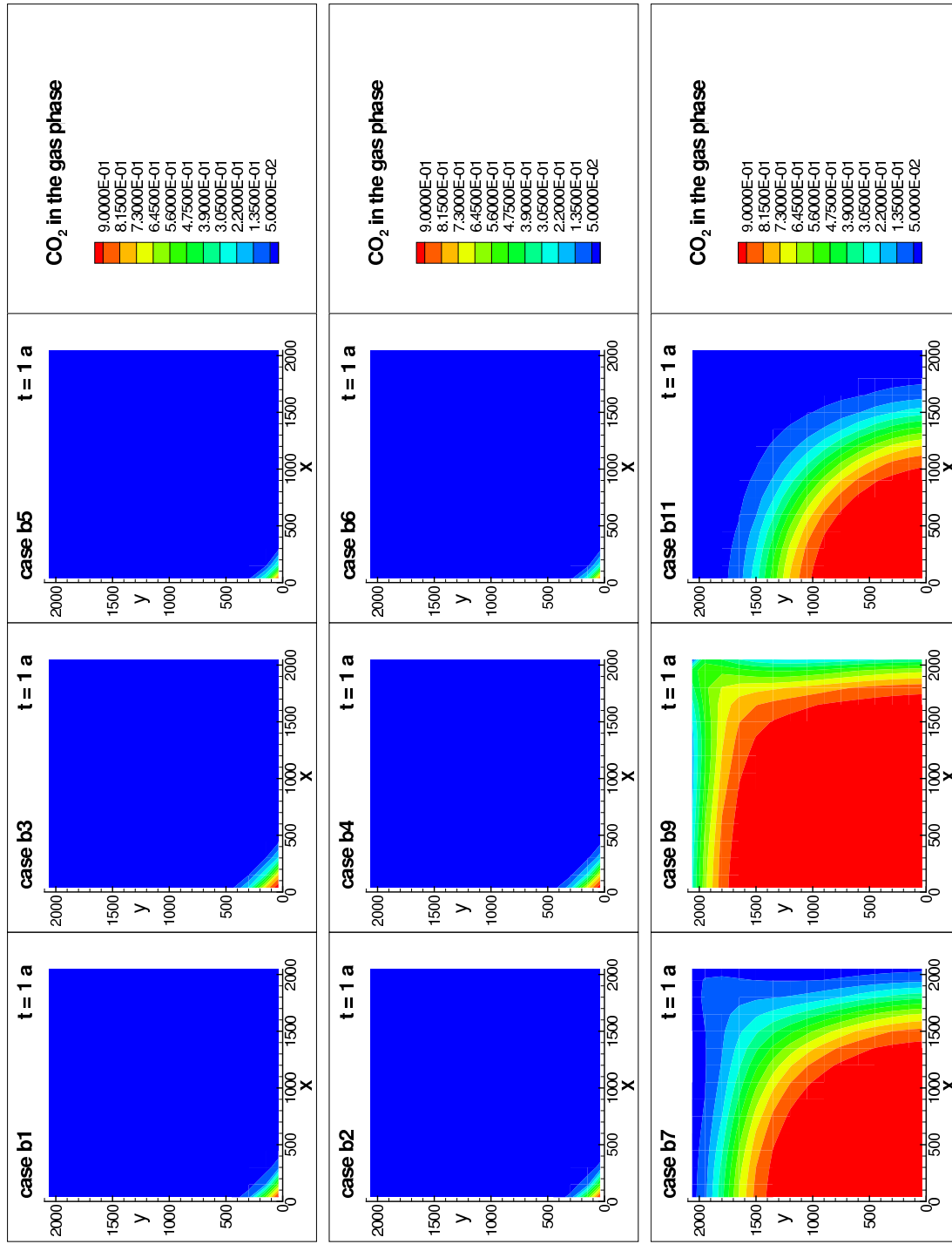


Figure 30: The time-dependent distribution of the  $\text{CO}_2$  mass fraction in the gas phase after 1 year in the different 2D simulations documents the increase in the radius of influence due to higher porosities and higher injection rate, compare with Figure 31. The main characteristics of the different cases are listed in the Tables 5 and 6. The total injection rates are 0.0178 kg/s for Case b1 to Case b6 and 2.9091 kg/s for Case b7 to Case b11.

### 2D simulation - CH<sub>4</sub> extraction and CO<sub>2</sub> injection

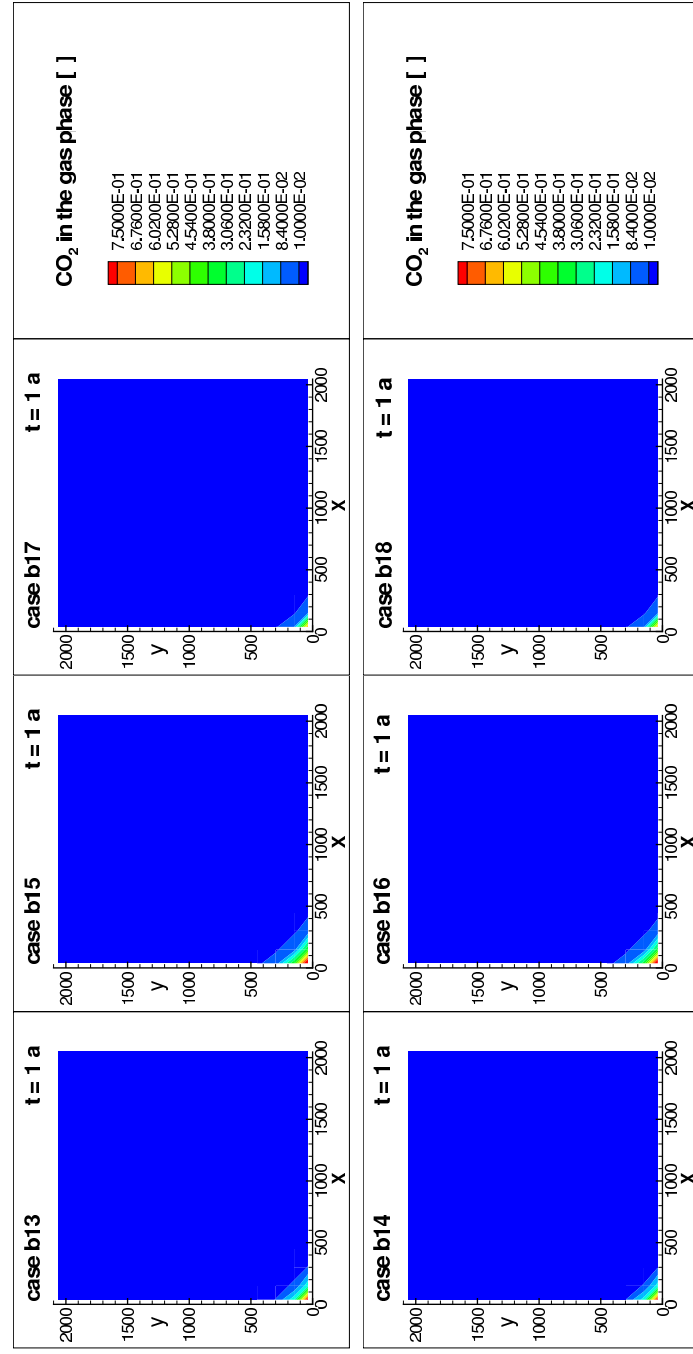


Figure 31: The time-dependent distribution of the CO<sub>2</sub> mass fraction in the gas phase after 1 year in the different 2D simulations documents the increase in the radius of influence due to higher porosities and higher injection rate, compare with Figure 30. The main characteristics of the different cases are listed in Table 7. The total injection rates are 0.0068 kg/s for Case b13 to Case b18.

## 2D simulation - CH<sub>4</sub> extraction and CO<sub>2</sub> injection

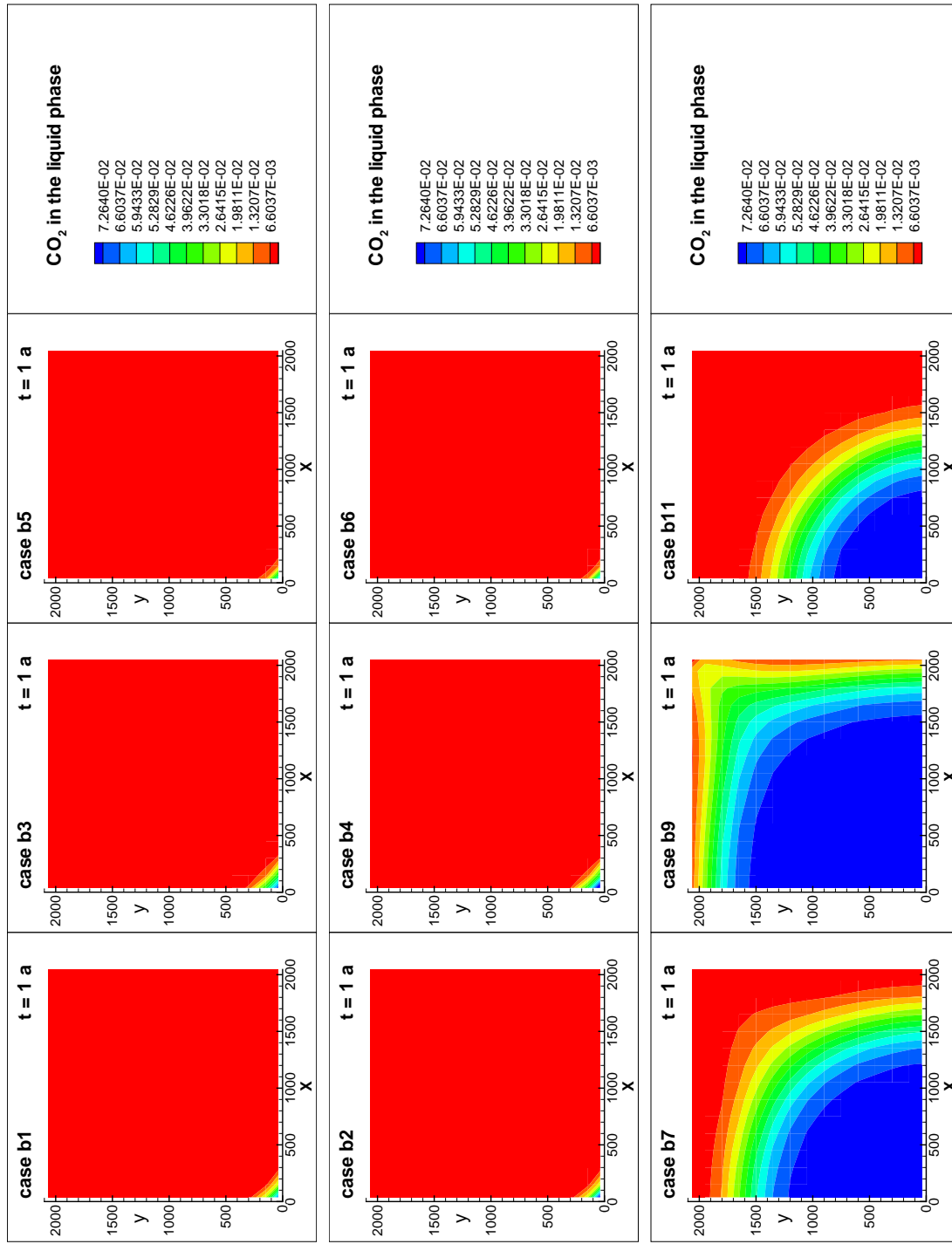


Figure 32: The time-dependent distribution of the CO<sub>2</sub> mass fraction in the liquid phase after 1 year in the different 2D simulations documents the increase in the radius of influence due to higher porosities and higher injection rate, compare with Figure 33. The main characteristics of the different cases are listed in the Tables 5 and 6. The total injection rates are 0.0178 kg/s for Case b1 to Case b6 and 2.9091 kg/s for Case b7 to Case b11.

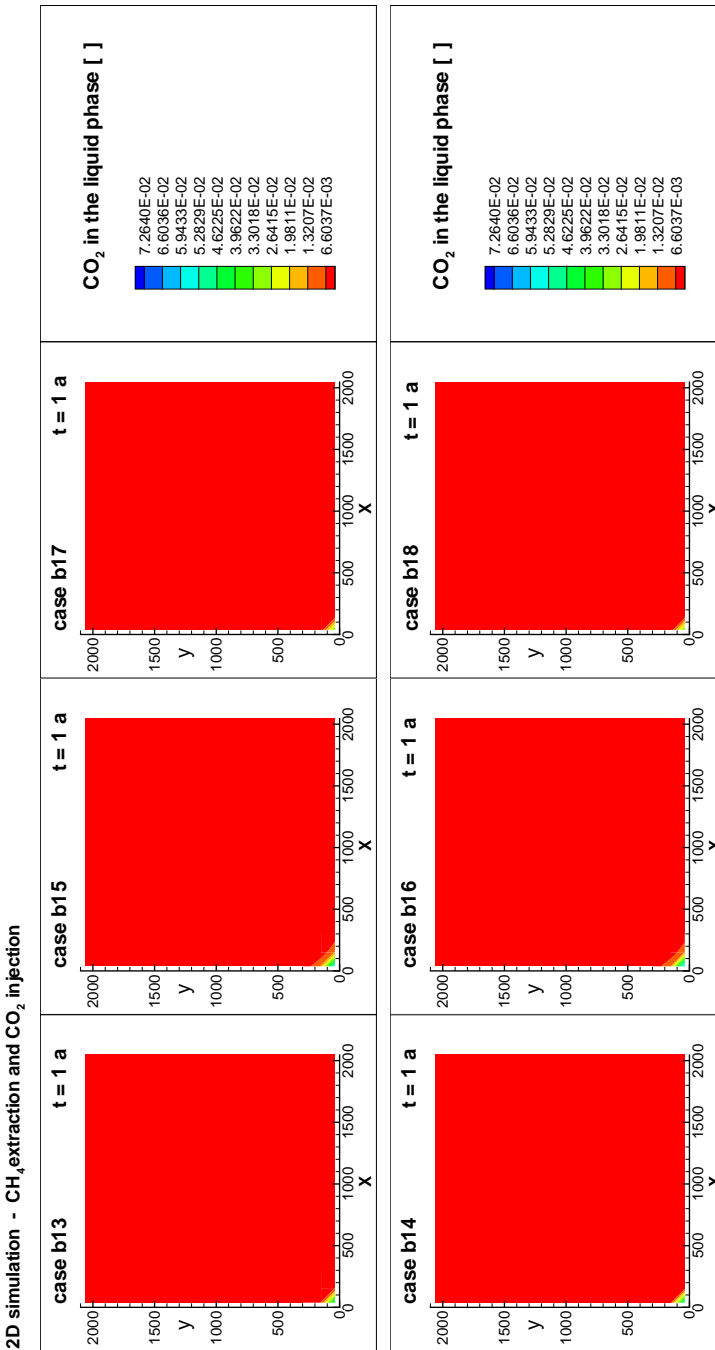


Figure 33: The time-dependent distribution of the  $\text{CO}_2$  mass fraction in the liquid phase after 1 year in the different 2D simulations documents the increase in the radius of influence due to higher porosities and higher injection rate, compare with Figure 32. The main characteristics of the different cases are listed in Table 7. The total injection rates are 0.0068 kg/s for Case b13 to Case b18.

## 2D simulation - CH<sub>4</sub> extraction and CO<sub>2</sub> injection

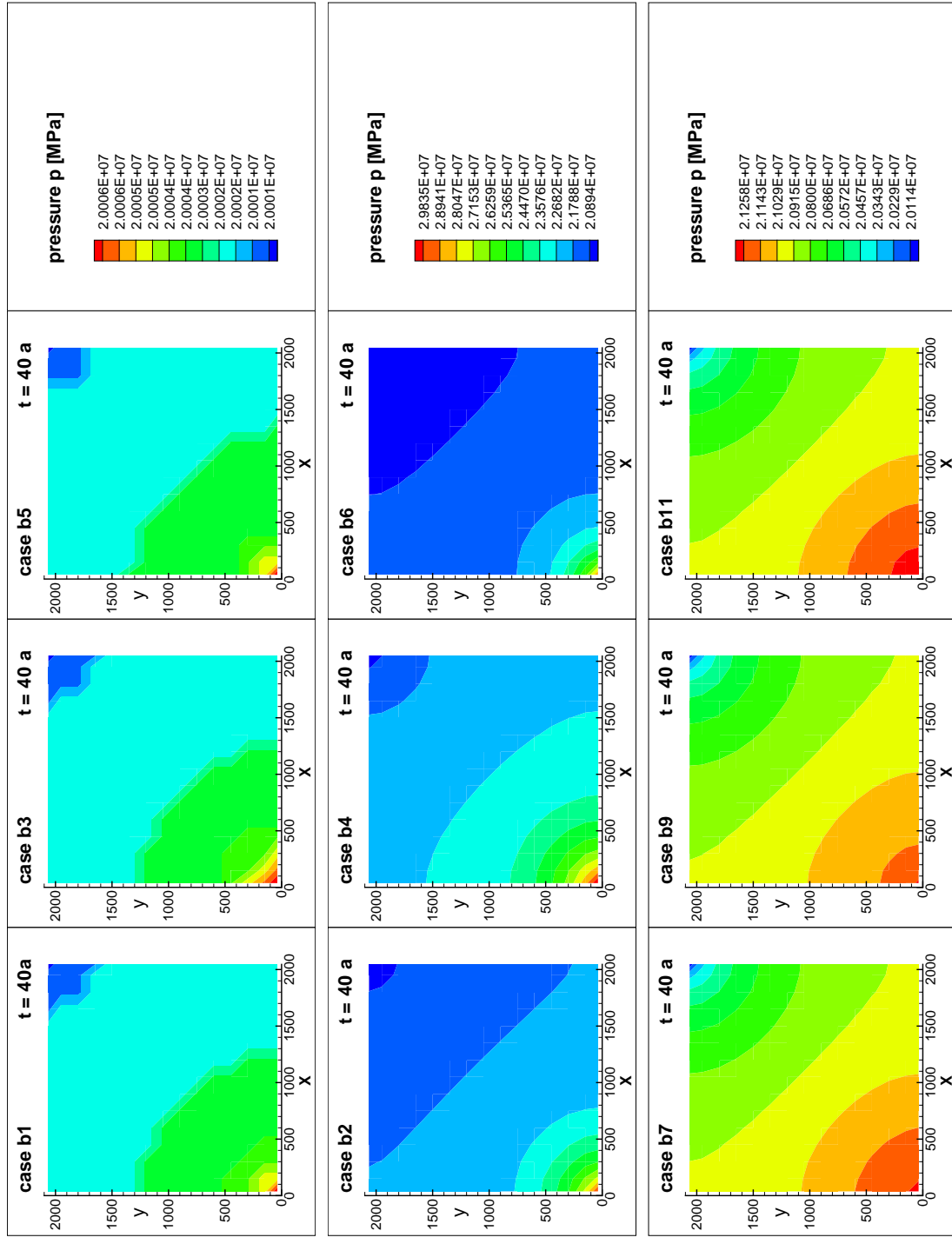


Figure 34: The time-dependent pressure distribution after 40 years in the different 2D simulations documents the higher values for the simulations with smaller porosities or higher injection rates, and the larger radius of influence due to higher permeabilities. The main characteristics of the different cases are listed in the Tables 5 and 6. The total injection rates are 0.0178 kg/s for Case b1 to Case b6 and 2.9091 kg/s for Case b7 to Case b11.

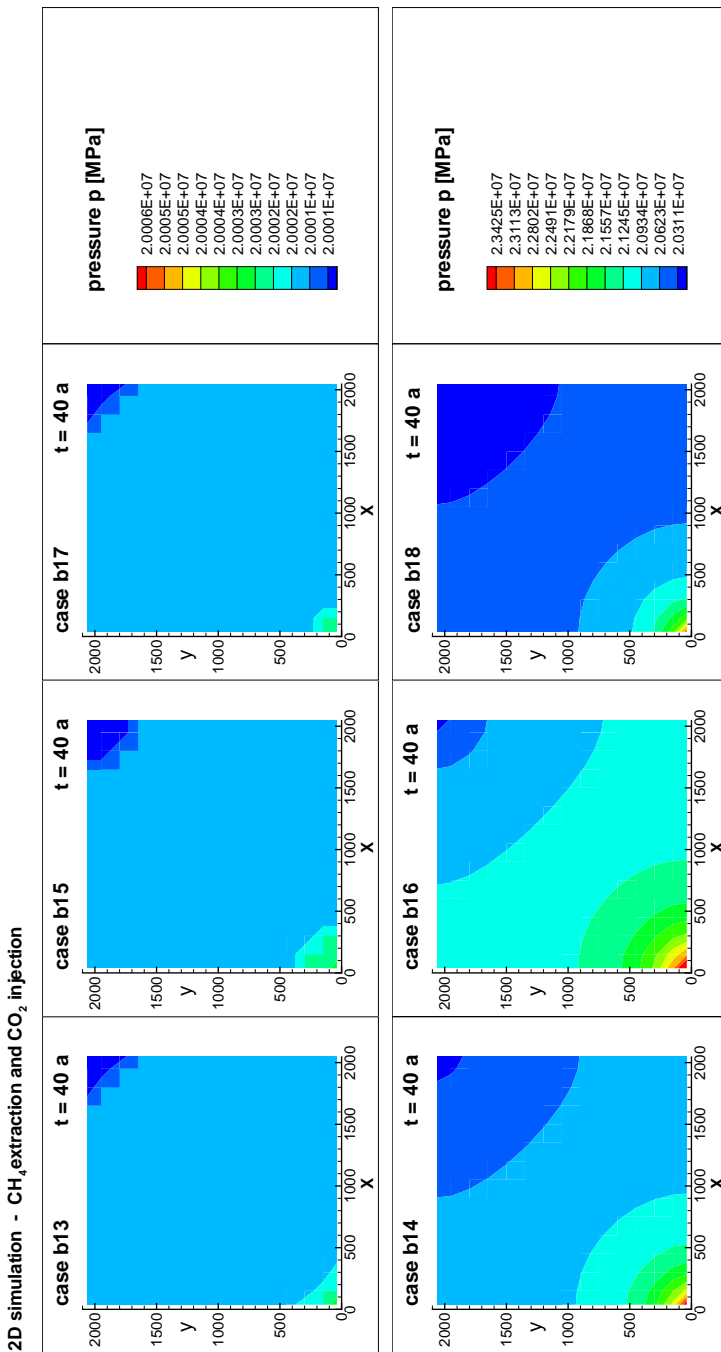


Figure 35: The time-dependent pressure distribution after 40 years in the different 2D simulations documents the higher values for the simulations with smaller porosities, and the larger radius of influence due to higher permeabilities. The main characteristics of the different cases are listed in Table 7. The total injection rates are 0.0068 kg/s for Case b13 to Case b18.

## 2D simulation - $\text{CH}_4$ extraction and $\text{CO}_2$ injection

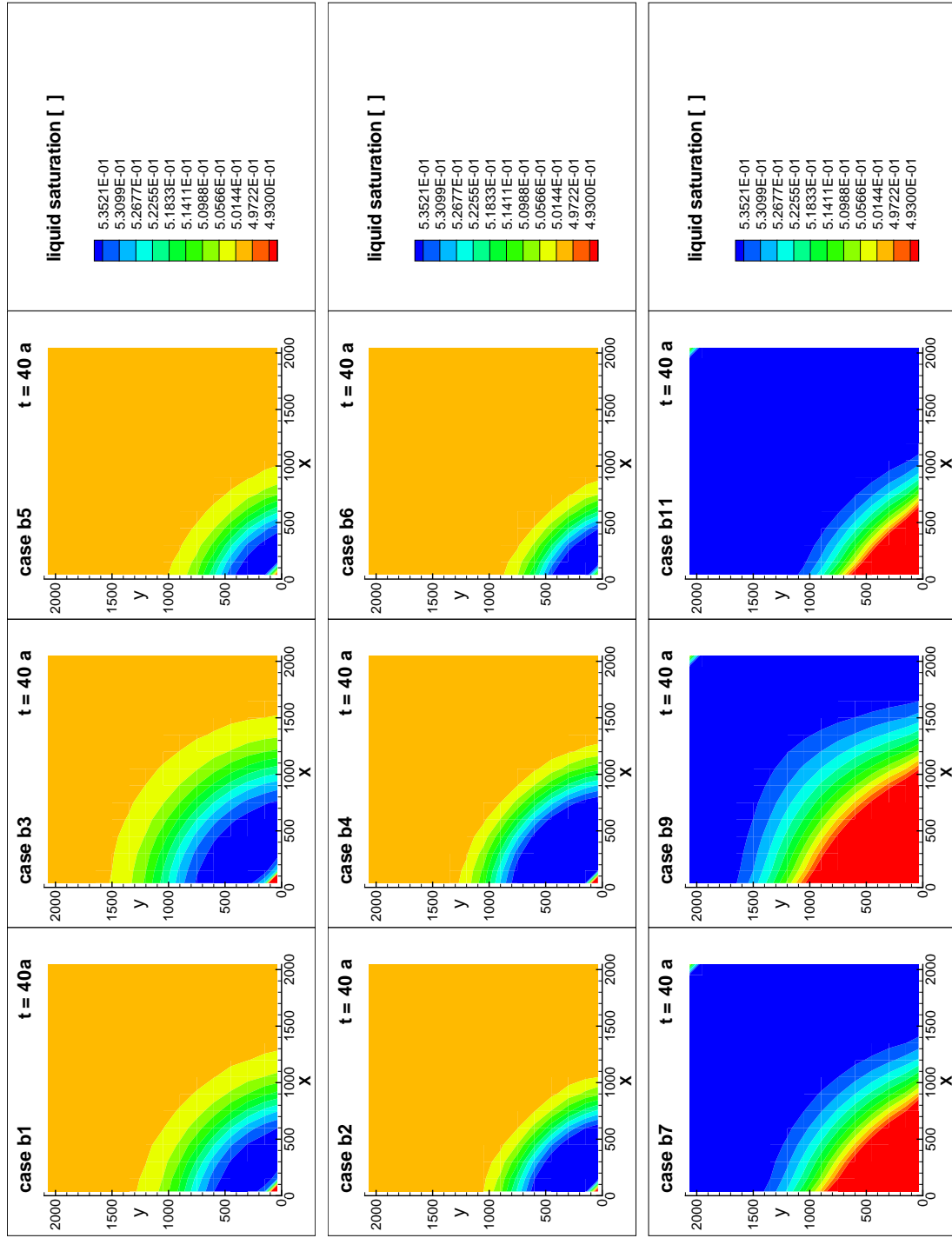


Figure 36: The time-dependent distribution of the liquid saturation after 40 years in the different 2D simulations illustrates the higher values for the simulations with smaller porosities and higher injection rates. The main characteristics of the different cases are listed in the Tables 5 and 6. The total injection rates are 0.0178 kg/s for Case b1 to Case b6 and 2.9091 kg/s for Case b7 to Case b11.

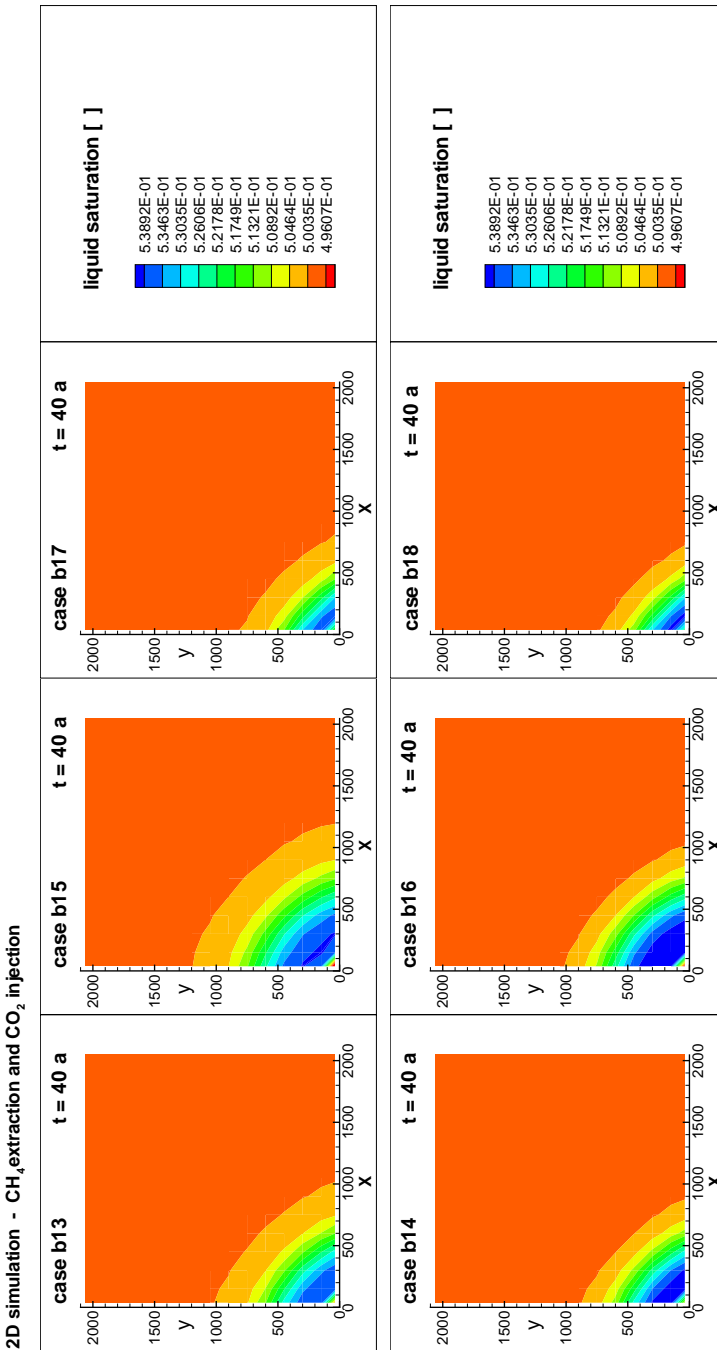


Figure 37: The time-dependent distribution of the liquid saturation after 40 years in the different 2D simulations illustrates the higher values for the simulations with smaller porosities, compare with Figure 36. The main characteristics of the different cases are listed in Table 7. The total injection rates are 0.0068 kg/s for Case b13 to Case b18.

## 2D simulation - CH<sub>4</sub> extraction and CO<sub>2</sub> injection

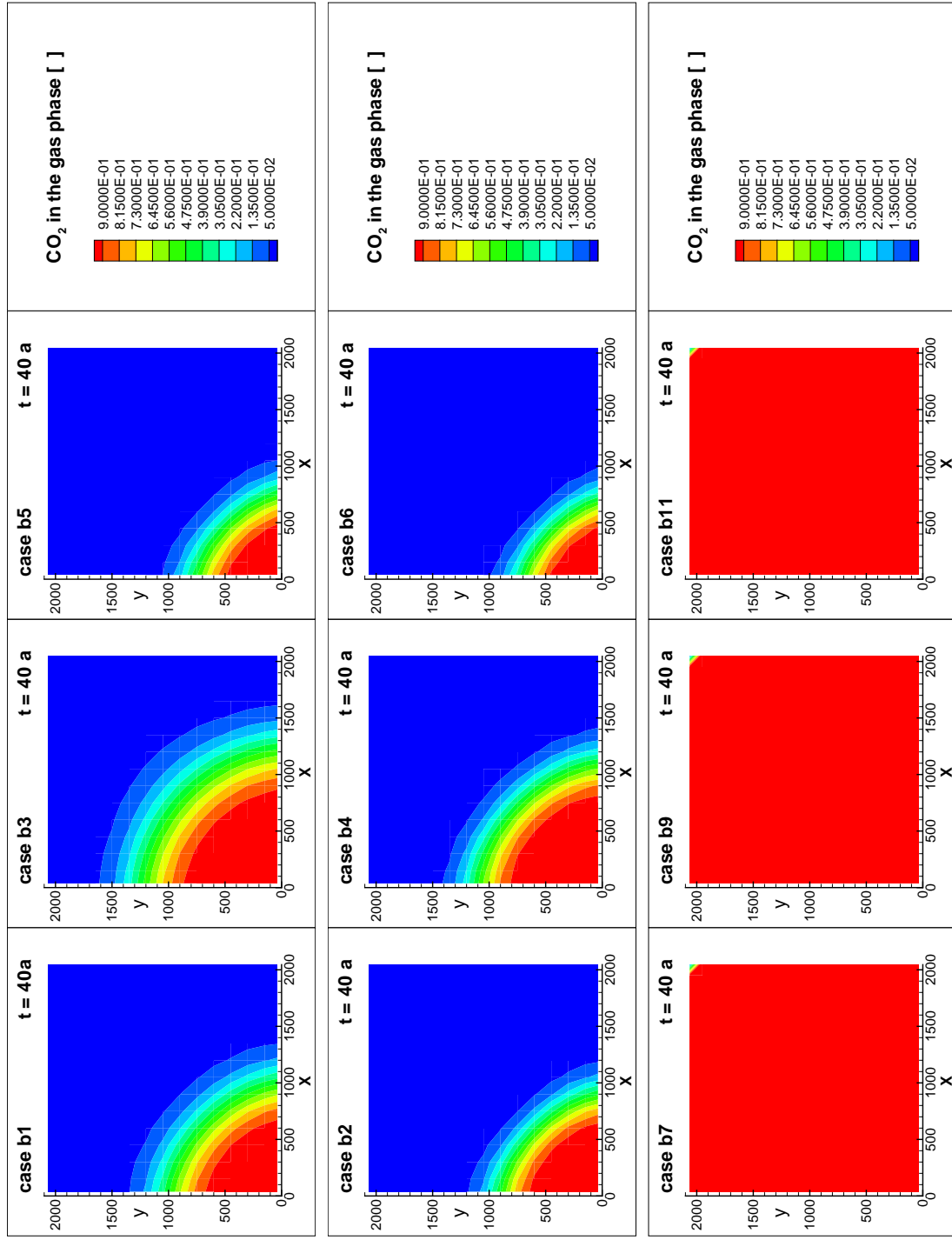


Figure 38: The time-dependent distribution of the CO<sub>2</sub> mass fraction in the gas phase after 40 years in the different 2D simulations documents the increase in the radius of influence due to higher porosities and higher injection rate, compare with Figure 37. The main characteristics of the different cases are listed in the Tables 5 and 6. The total injection rates are 0.0178 kg/s for Case b1 to Case b6 and 2.9091 kg/s for Case b7 to Case b11.

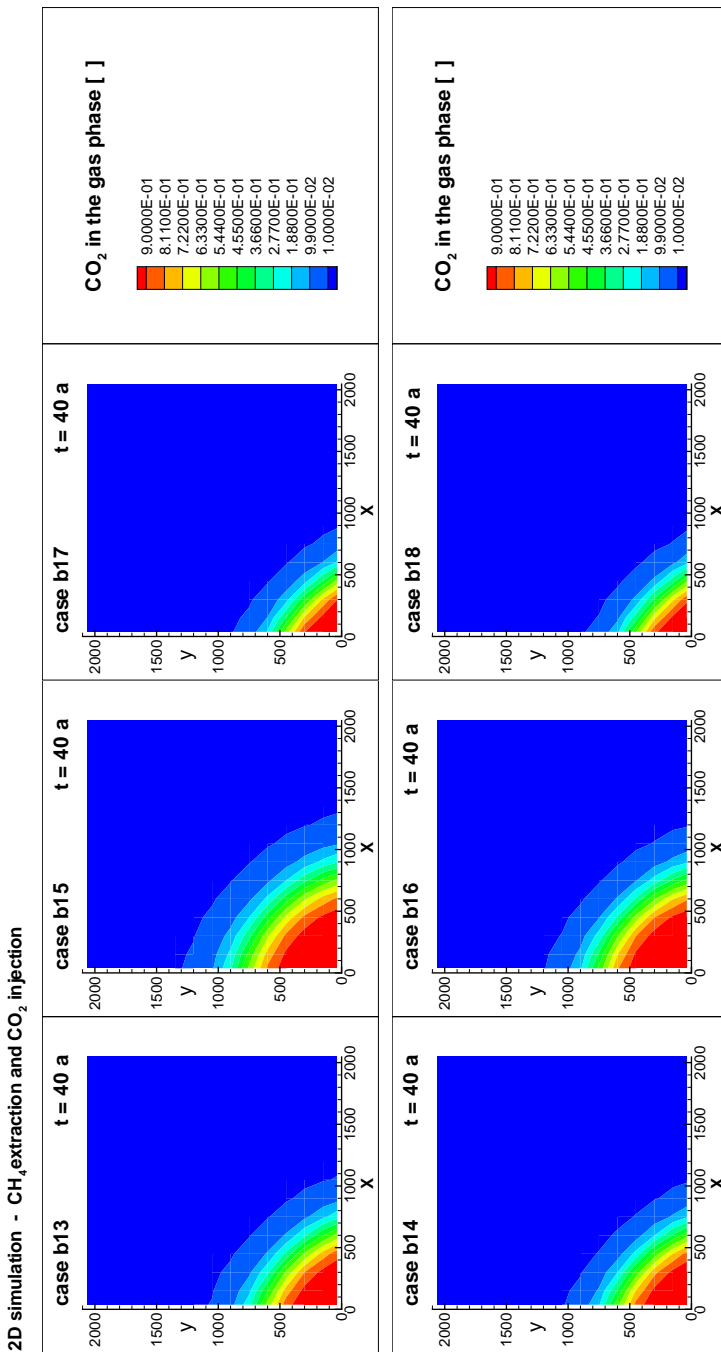


Figure 39: The time-dependent distribution of the  $\text{CO}_2$  mass fraction in the gas phase after 40 years in the different 2D simulations documents the increase in the radius of influence due to higher porosities and higher injection rate, compare with Figure 38. The main characteristics of the different cases are listed in Table 7. The total injection rates are 0.0068 kg/s for Case b13 to Case b18.

## 2D simulation - $\text{CH}_4$ extraction and $\text{CO}_2$ injection

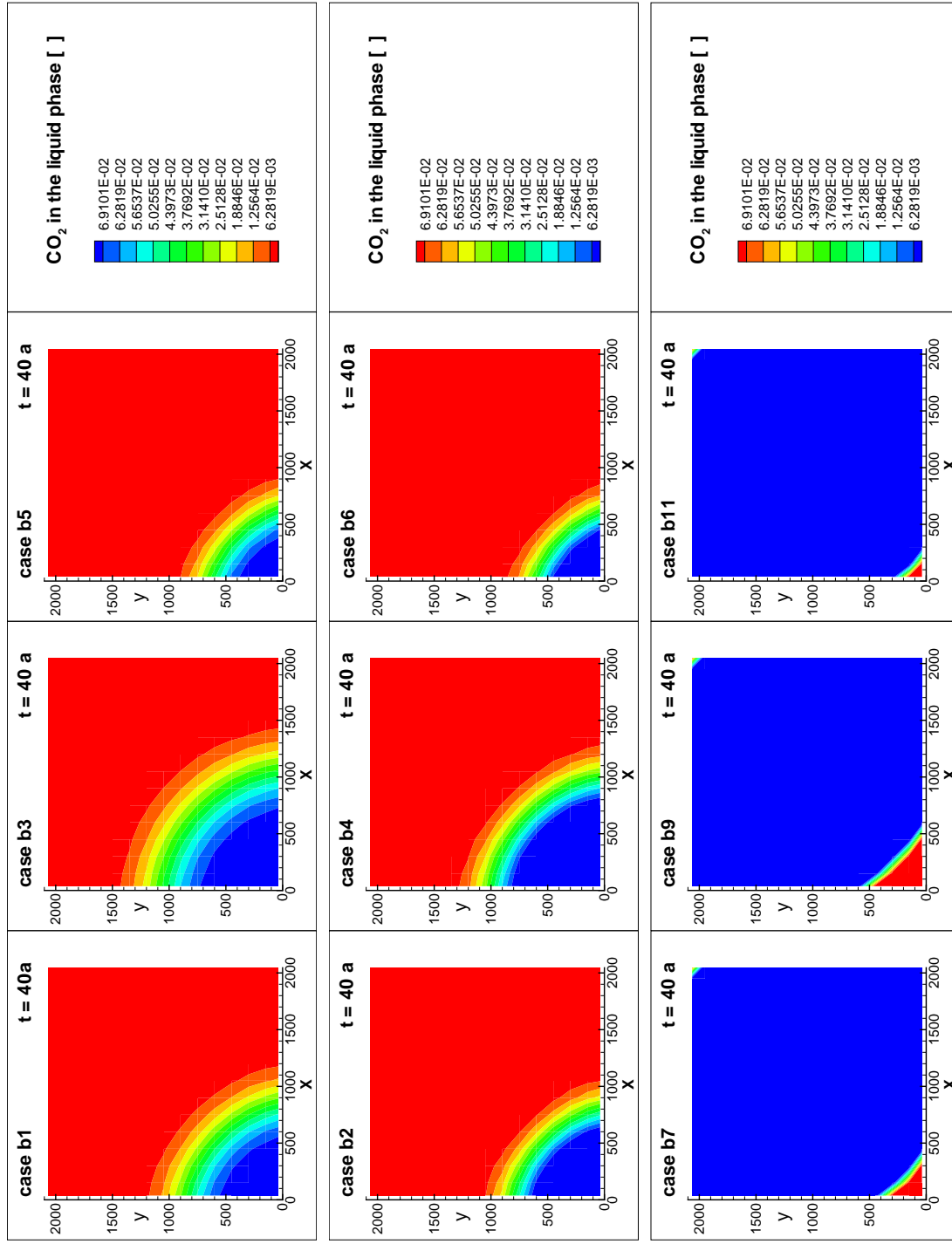
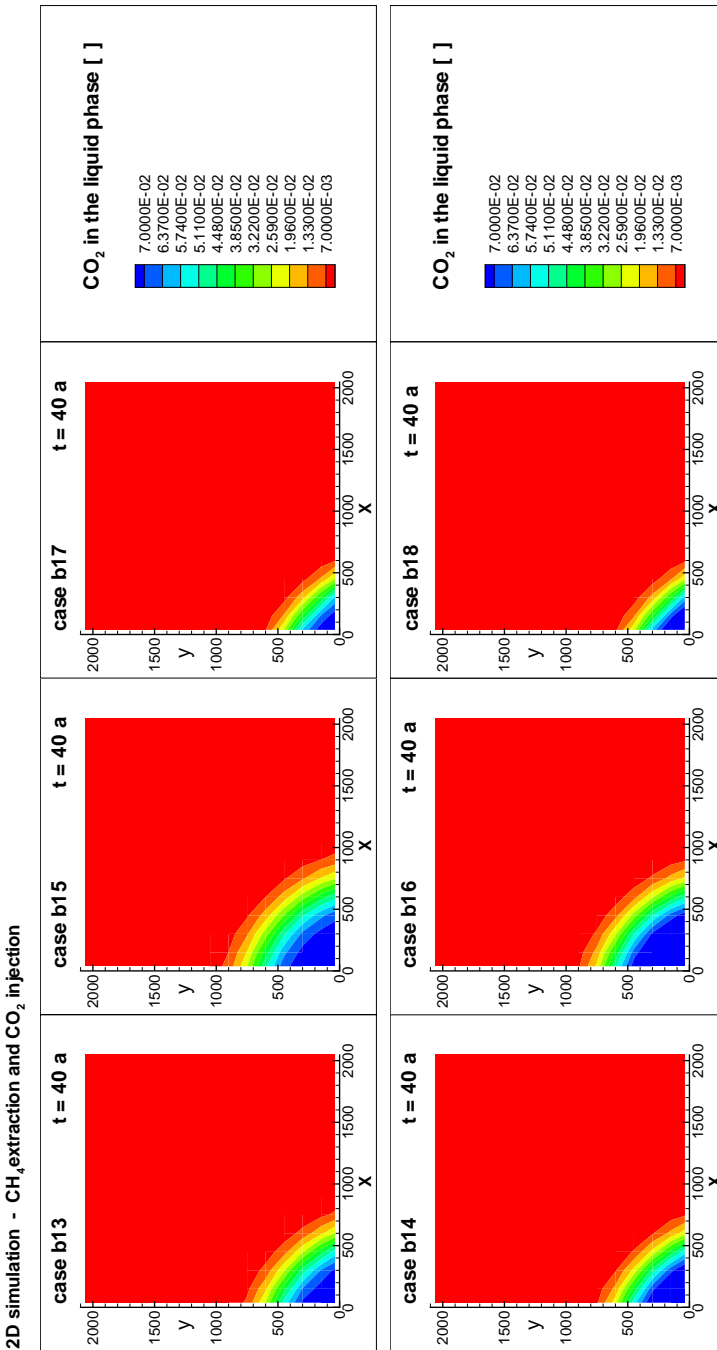
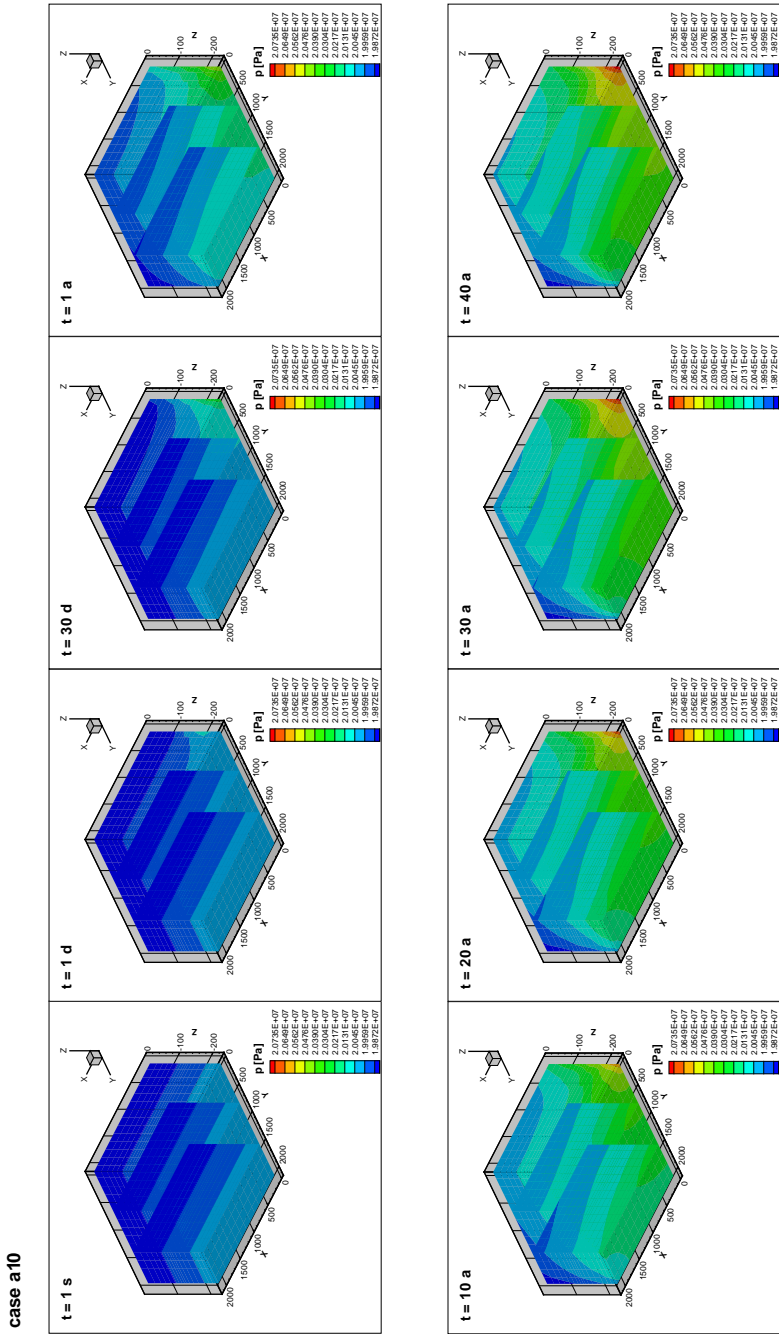


Figure 40: The time-dependent distribution of the  $\text{CO}_2$  mass fraction in the liquid phase after 40 years in the different 2D simulations documents the increase in the radius of influence due to higher porosities and higher injection rate, compare with Figure 41. The main characteristics of the different cases are listed in the Tables 5 and 6. The total injection rates are 0.0178 kg/s for Case b1 to Case b7 to Case b11.



*Figure 41: The time-dependent distribution of the  $\text{CO}_2$  mass fraction in the liquid phase after 40 years in the different 2D simulations documents the increase in the radius of influence due to higher porosities and higher injection rate, compare with Figure 40. The main characteristics of the different cases are listed in Table 7. The total injection rates are 0.0068 kg/s for Case b13 to Case b18.*



**Figure 42:** Simulations of  $\text{CH}_4$  extraction and  $\text{CO}_2$  injection show the development of pressure  $p$  [Pa] in time in the 3D grid. The Units Zyk13 (gridblocks AD1 1, AE1 1), Z9–11 (AD1 1, AE1 1) have isotropic permeabilities of  $1 \times 10^{-12} \text{ m}^2$ , all other layers have isotropic permeabilities of  $5 \times 10^{-16} \text{ m}^2$ . The extraction of  $\text{CH}_4$  in 18 gridblocks in a vertical column is realized with a constant pressure of extraction gridblocks (left corner), the injection of  $\text{CO}_2$  in 18 gridblocks in a vertical column is achieved with injection rates of each gridblock depending on the permeability of the layer (right corner). The total injection rate is  $8 \text{ kg/s}$ , the simulated time is 40 years.

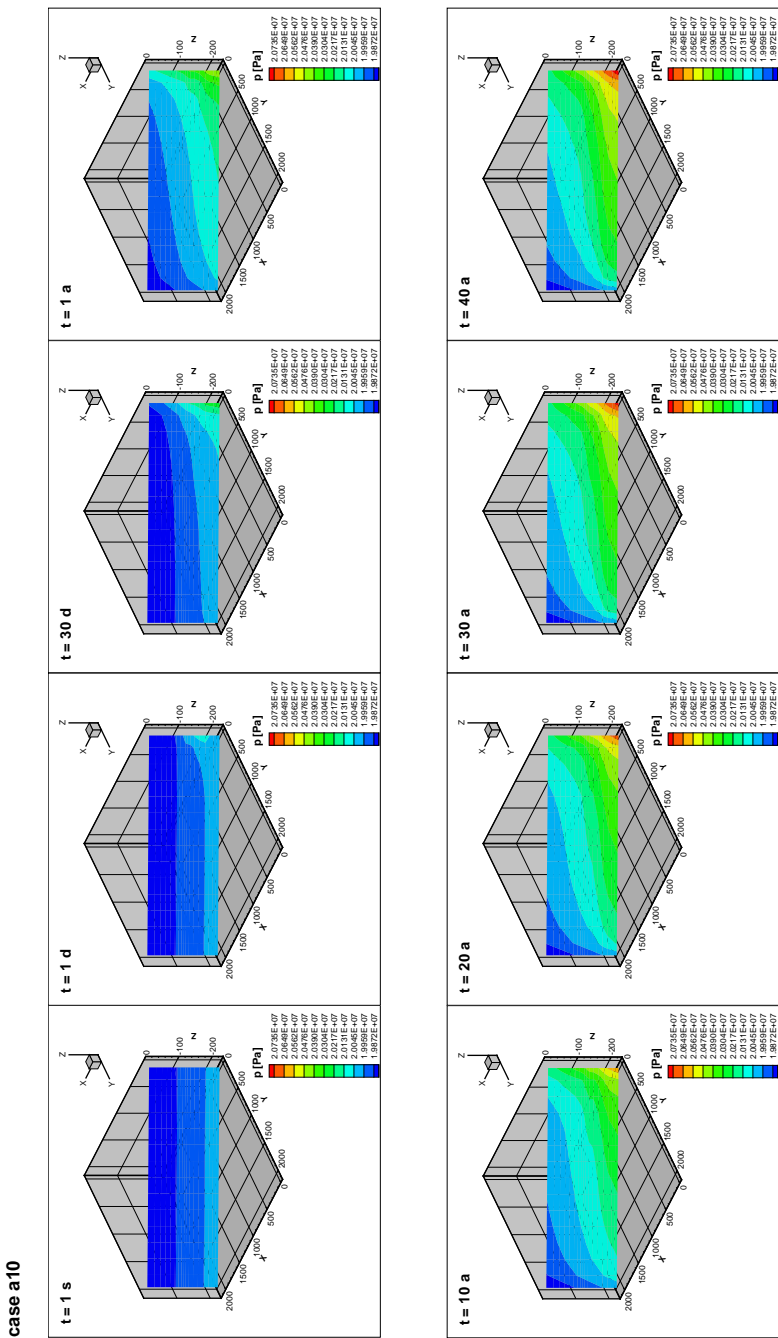


Figure 43: The same data as in Figure 42 is shown in a diagonal slice of the 3D grid.

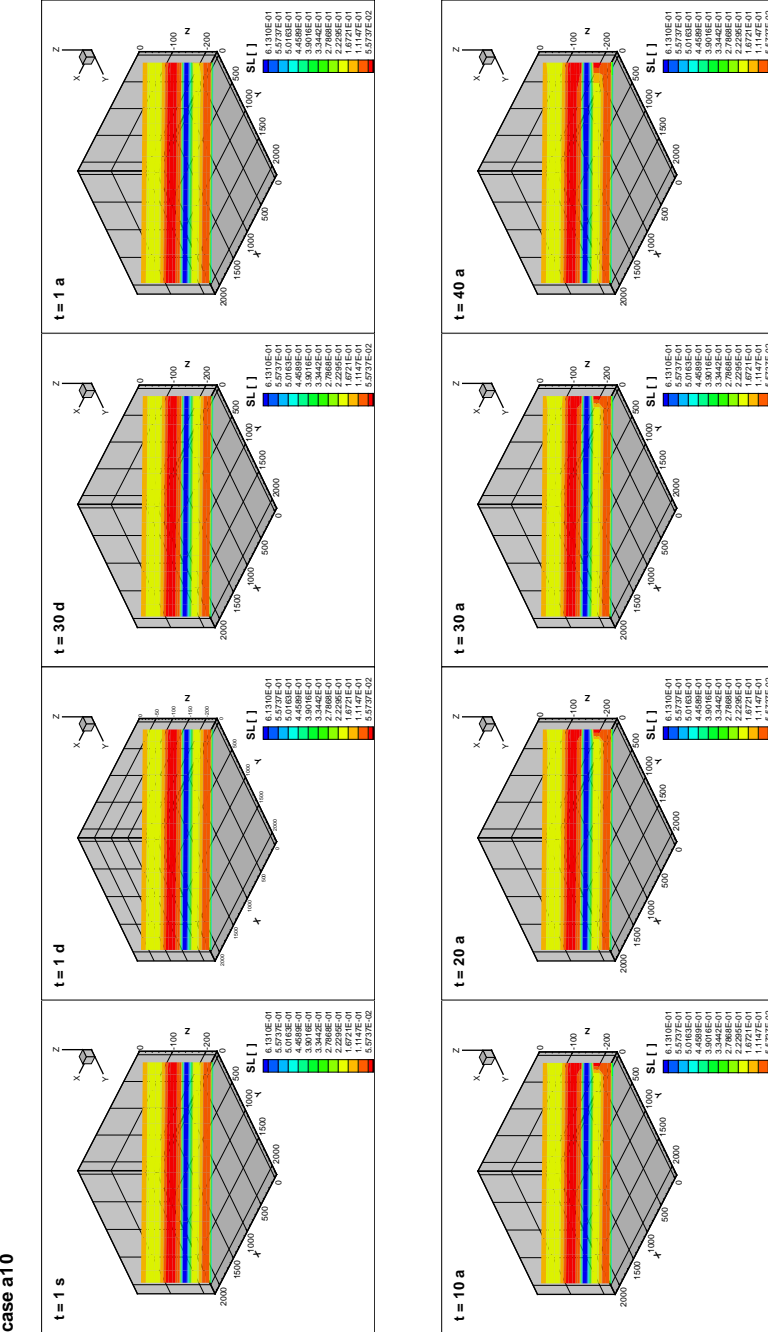
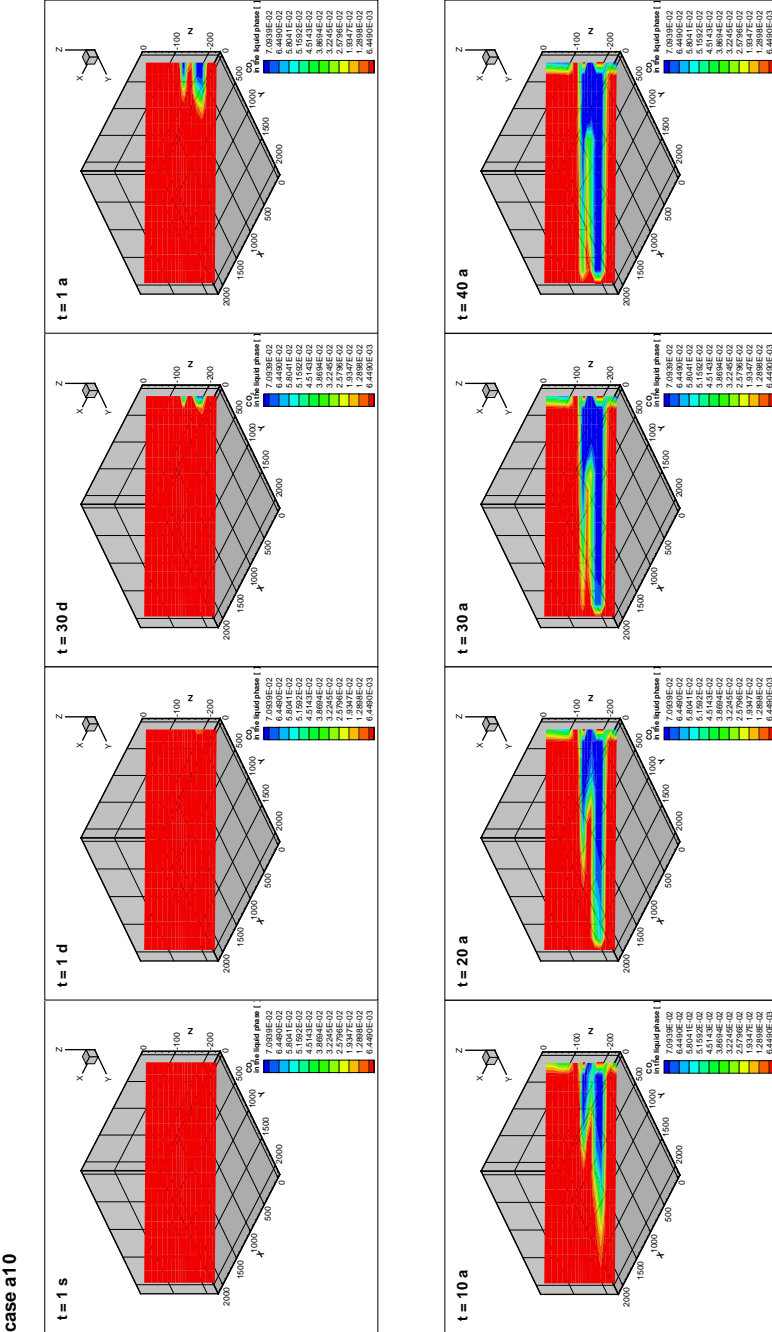
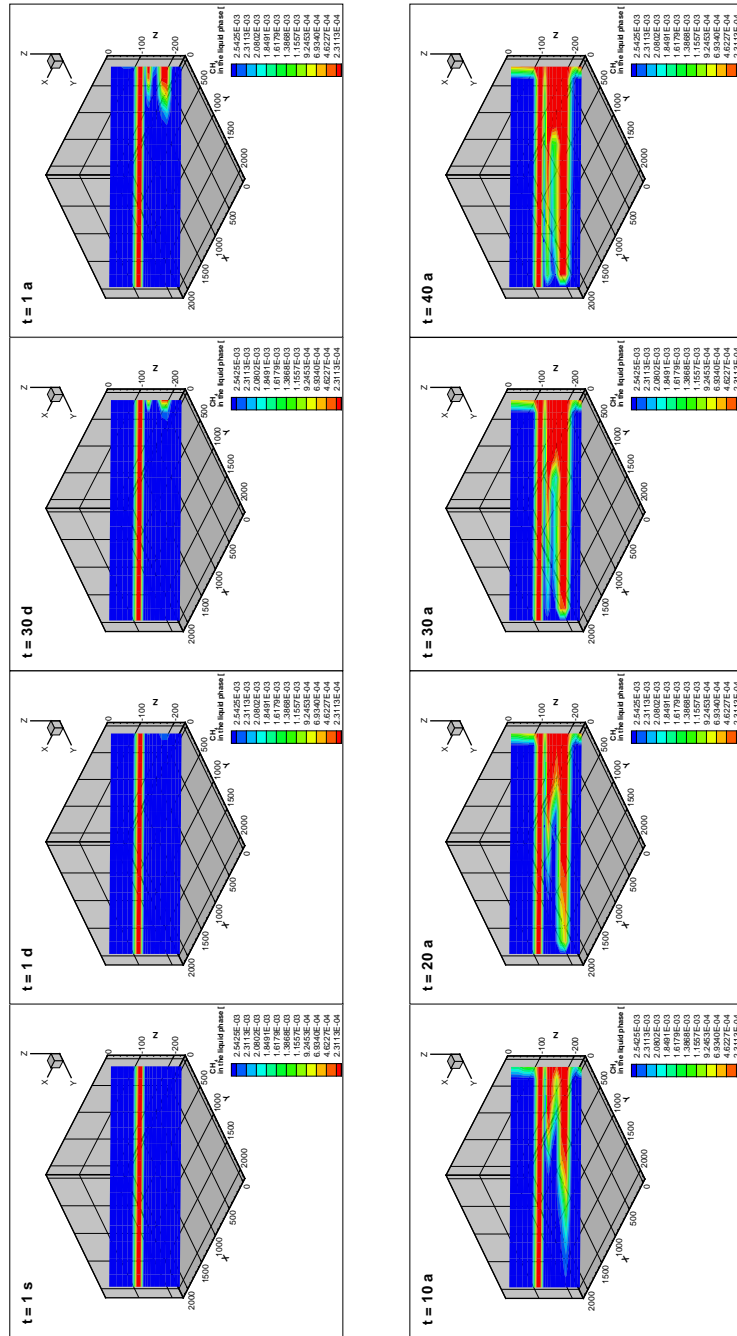


Figure 44: Simulations of  $\text{CH}_4$  extraction and  $\text{CO}_2$  injection show the development of liquid saturation in time in a diagonal slice of the 3D grid. The Units Zyk13 (gridblocks AD1 1, AE1 1), Z9–II (AD1 1, AE1 1) have isotropic permeabilities of  $1 \times 10^{-12} \text{ m}^2$ , all other layers have isotropic permeabilities of  $5 \times 10^{-16} \text{ m}^2$ . The extraction of  $\text{CH}_4$  in 18 gridblocks in a vertical column is realized with a constant pressure of extraction gridblocks (left corner), the injection of  $\text{CO}_2$  in 18 gridblocks in a vertical column is achieved with injection rates of each gridblock depending on the permeability of the layer (right corner). The total injection rate is  $8 \text{ kg/s}$ , the simulated time is 40 years.



*Figure 45: Simulations of  $\text{CH}_4$  extraction and  $\text{CO}_2$  injection show the time development of the  $\text{CO}_2$  mass fraction in the liquid phase in a diagonal slice of the 3D grid. The Units Zyk13 (gridblocks AD1 1, AE1 1), Zg-11 (AD1 1, AE1 1) have isotropic permeabilities of  $1 \times 10^{-12} \text{ m}^2$ , all other layers have isotropic permeabilities of  $5 \times 10^{-16} \text{ m}^2$ . The extraction of  $\text{CH}_4$  in 18 gridblocks in a vertical column is realized with a constant pressure of extraction gridblocks (left corner), the injection of  $\text{CO}_2$  in 18 gridblocks in a vertical column is achieved with injection rates of each gridblock in dependence of the permeability of the layer (right corner). The total injection rate is 8 kg/s, the simulated time is 40 years.*

case a10



*Figure 46: Simulations of  $\text{CH}_4$  extraction and  $\text{CO}_2$  injection show the time development of the  $\text{CH}_4$  mass fraction in the liquid phase in a diagonal slice of the 3D grid. The Units Zyk13 (gridblocks AD1 1, AE1 1), Zg-11 (AD1 1, AE1 1) have isotropic permeabilities of  $1 \times 10^{-12} \text{ m}^2$ , all other layers have isotropic permeabilities of  $5 \times 10^{-16} \text{ m}^2$ . The extraction of  $\text{CH}_4$  in 18 gridblocks in a vertical column is realized with a constant pressure of extraction gridblocks (left corner), the injection of  $\text{CO}_2$  in 18 gridblocks in a vertical column is achieved with injection rates of each gridblock in dependence of the permeability of the layer (right corner). The total injection rate is 8 kg/s, the simulated time is 40 years.*

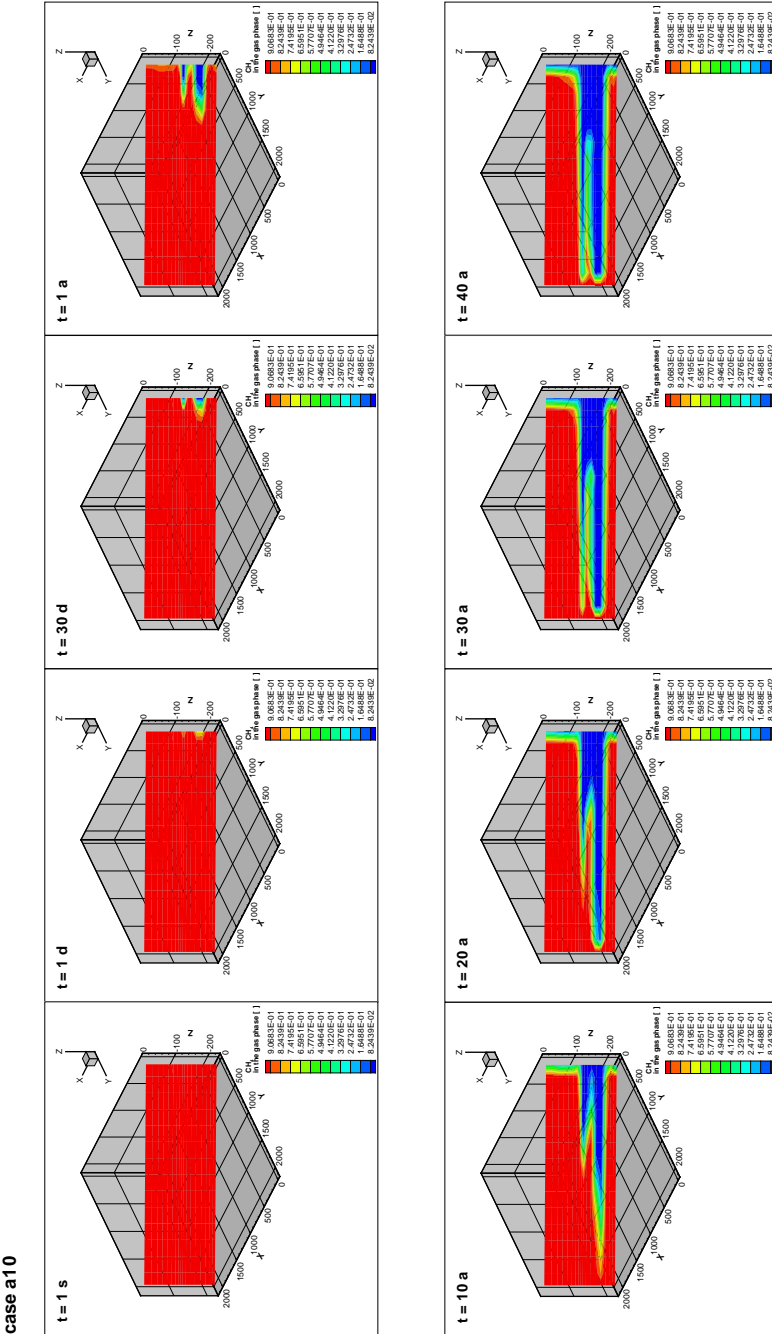


*Figure 47: Simulations of  $\text{CH}_4$  extraction and  $\text{CO}_2$  injection show the time development of the  $\text{CH}_4$  mass fraction in the gas phase in a diagonal slice of the 3D grid. The Units Zyk13 (gridblocks AD1 1, AE1 1), Zg-11 (AD1 1, AE1 1) have isotropic permeabilities of  $1 \times 10^{-12} \text{ m}^2$ , all other layers have isotropic permeabilities of  $5 \times 10^{-16} \text{ m}^2$ . The extraction of  $\text{CH}_4$  in 18 gridblocks in a vertical column is realized with a constant pressure of extraction gridblocks (left corner), the injection of  $\text{CO}_2$  in 18 gridblocks in a vertical column is achieved with injection rates of each gridblock in dependence of the permeability of the layer (right corner). The total injection rate is 8 kg/s, the simulated time is 40 years.*

case a10

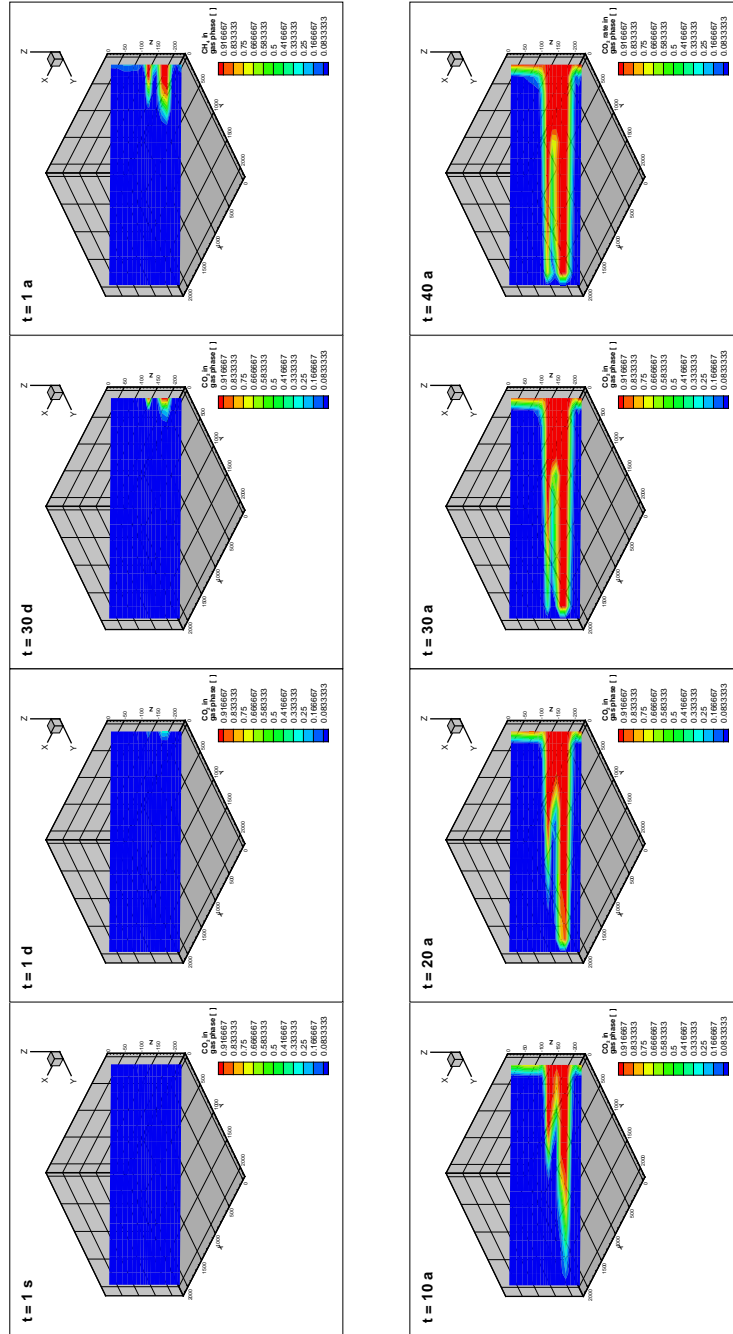


*Figure 48: Simulations of  $\text{CH}_4$  extraction and  $\text{CO}_2$  injection show the time development of the  $\text{CO}_2$  mass fraction in the gas phase in a diagonal slice of the 3D grid. The Units Zyk13 (gridblocks AD1 1, AE1 1), Zg-11 (AD1 1, AE1 1) have isotropic permeabilities of  $1 \times 10^{-12} \text{ m}^2$ , all other layers have isotropic permeabilities of  $5 \times 10^{-16} \text{ m}^2$ . The extraction of  $\text{CH}_4$  in 18 gridblocks in a vertical column is realized with a constant pressure of extraction gridblocks (left corner), the injection of  $\text{CO}_2$  in 18 gridblocks in a vertical column is achieved with injection rates of each gridblock in dependence of the permeability of the layer (right corner). The total injection rate is 8 kg/s, te simulated time is 40 years.*

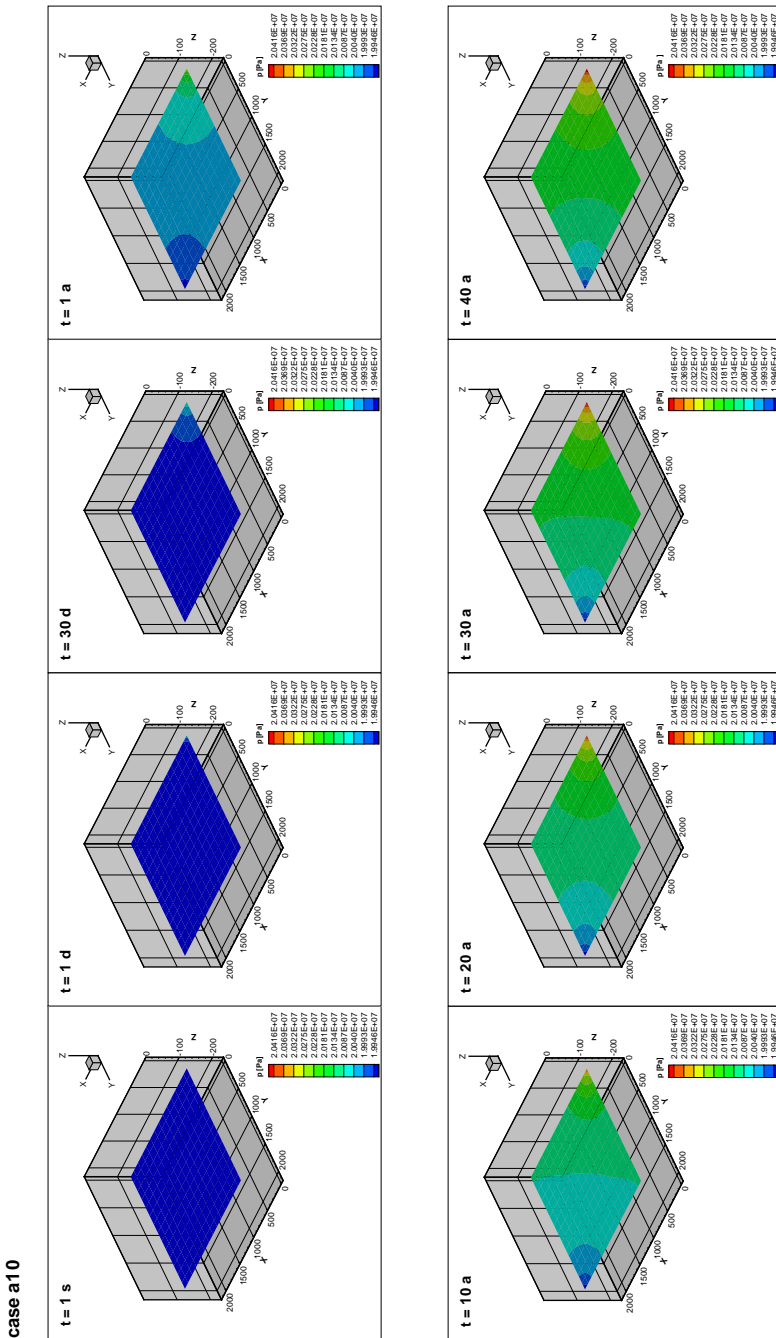
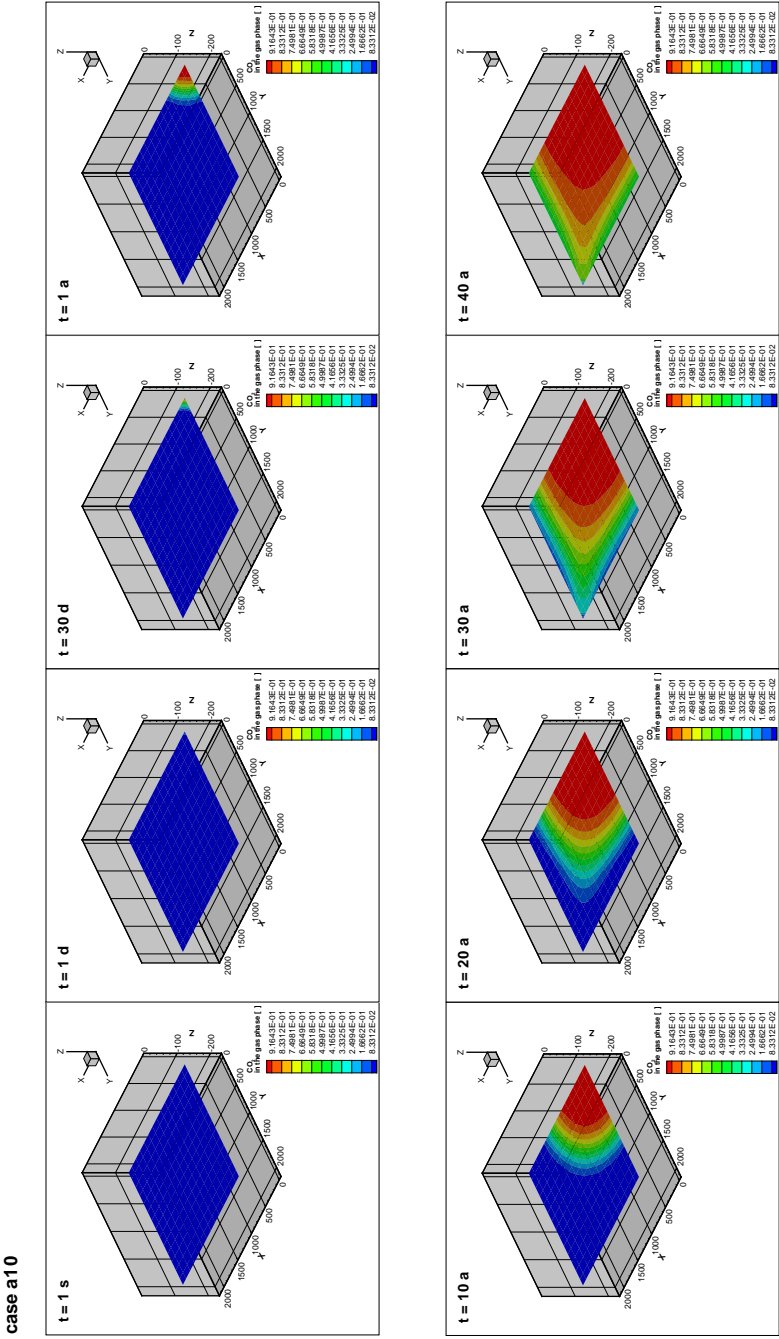


Figure 49: The horizontal slice of the 3D simulation is located within the high-permeability Unit Zyk13. It documents the pressurizing of the reservoir in time due to 40 years of  $\text{CO}_2$  injection. The total injection rate is  $8 \text{ kg/s}$ .



*Figure 50: The horizontal slice of the 3D simulation is located within the low-permeability Unit Zyk13. It documents the development of CO<sub>2</sub> mass fraction in the gas phase due to 40 years of CO<sub>2</sub> injection, illustrating the CO<sub>2</sub> sweeping of CH<sub>4</sub> in the direction of the extraction well. The total injection rate is 8 kg/s.*

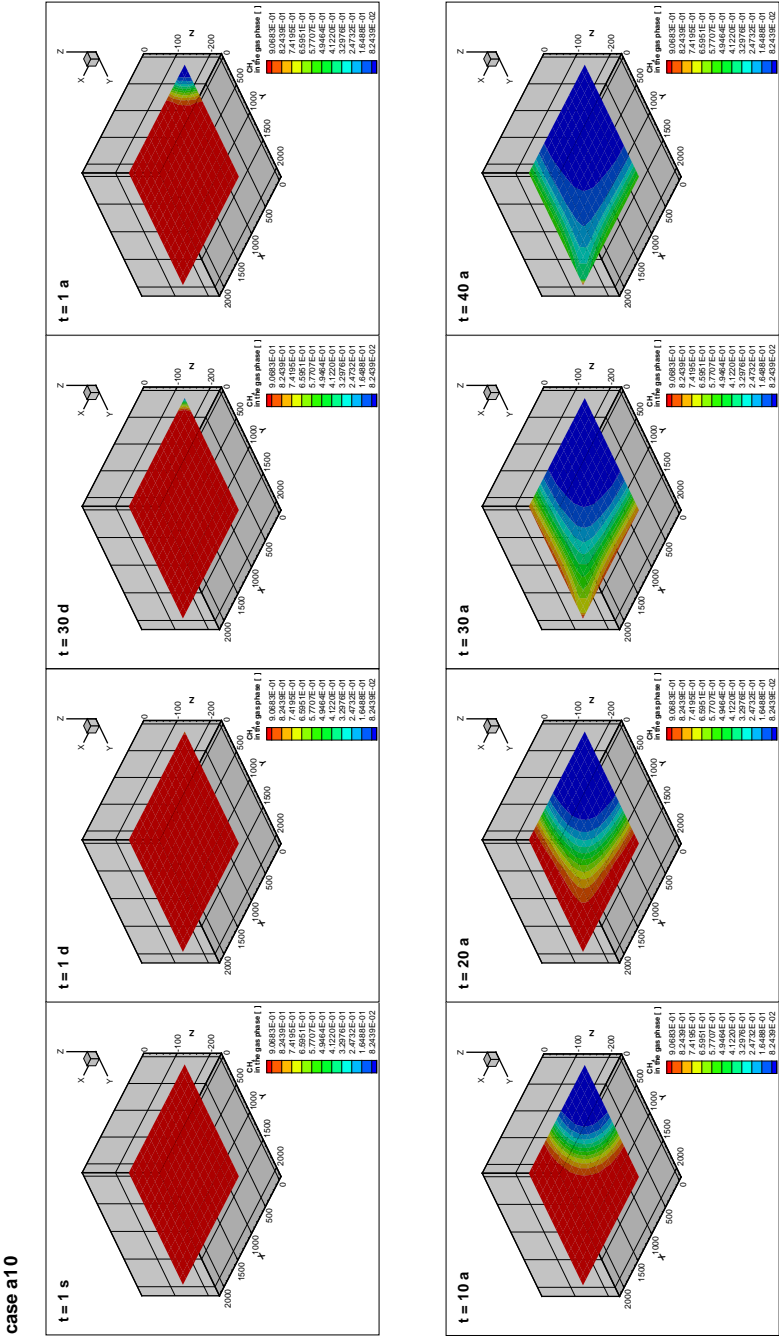


Figure 51: The horizontal slice of the 3D simulation is located within the high-permeability Unit Zyk13. It documents the development of CH<sub>4</sub> mass fraction in the gas phase due to 40 years of CO<sub>2</sub> injection, illustrating the CO<sub>2</sub> sweeping of CH<sub>4</sub> mass fraction in the direction of the extraction well. The total injection rate is 8 kg/s.

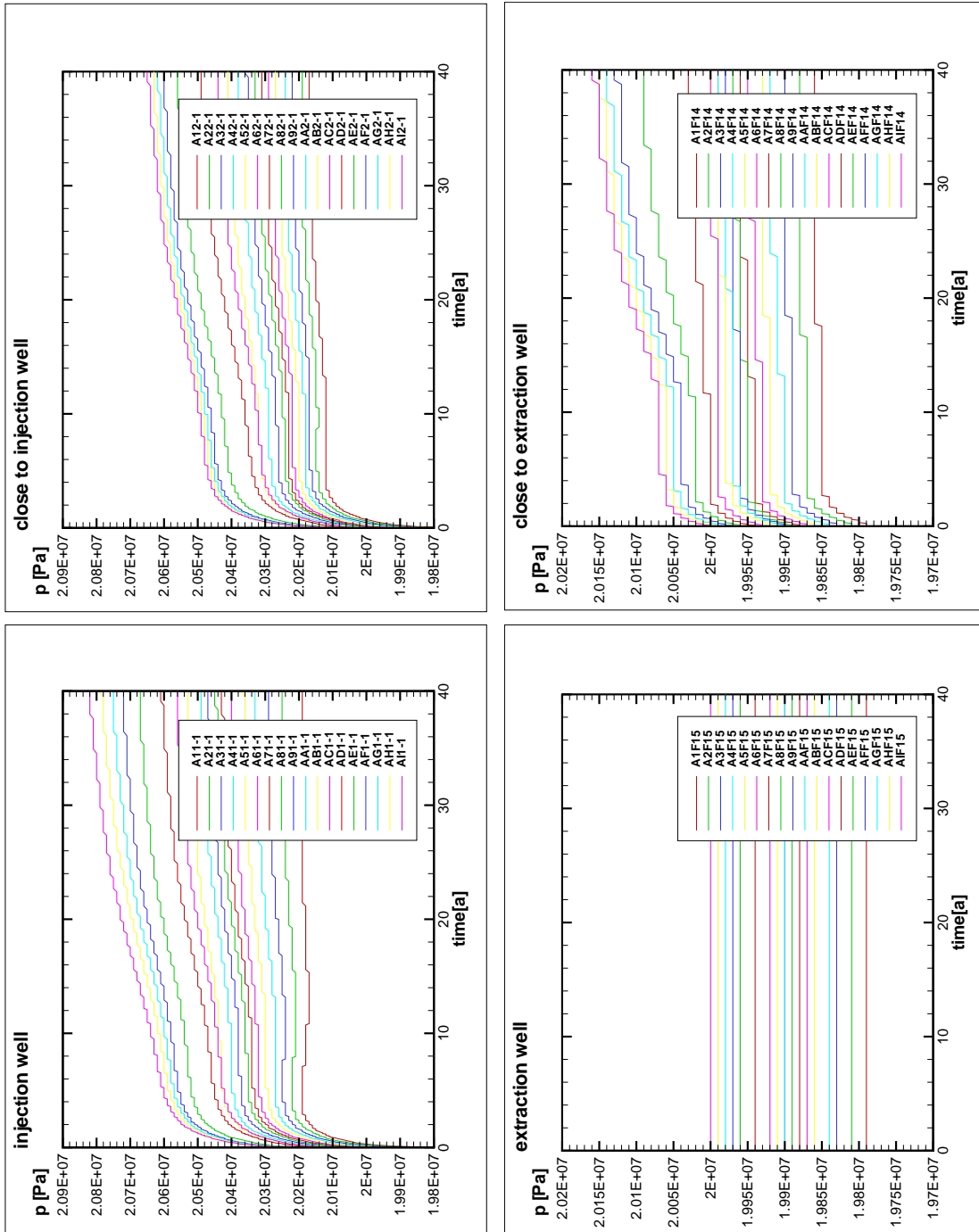


Figure 52: During the extraction and injection phase of the base-case the variation of the pressure in time starts from the staggered hydrostatic levels and progresses up to maximum values in the reservoir of 20.8 MPa.

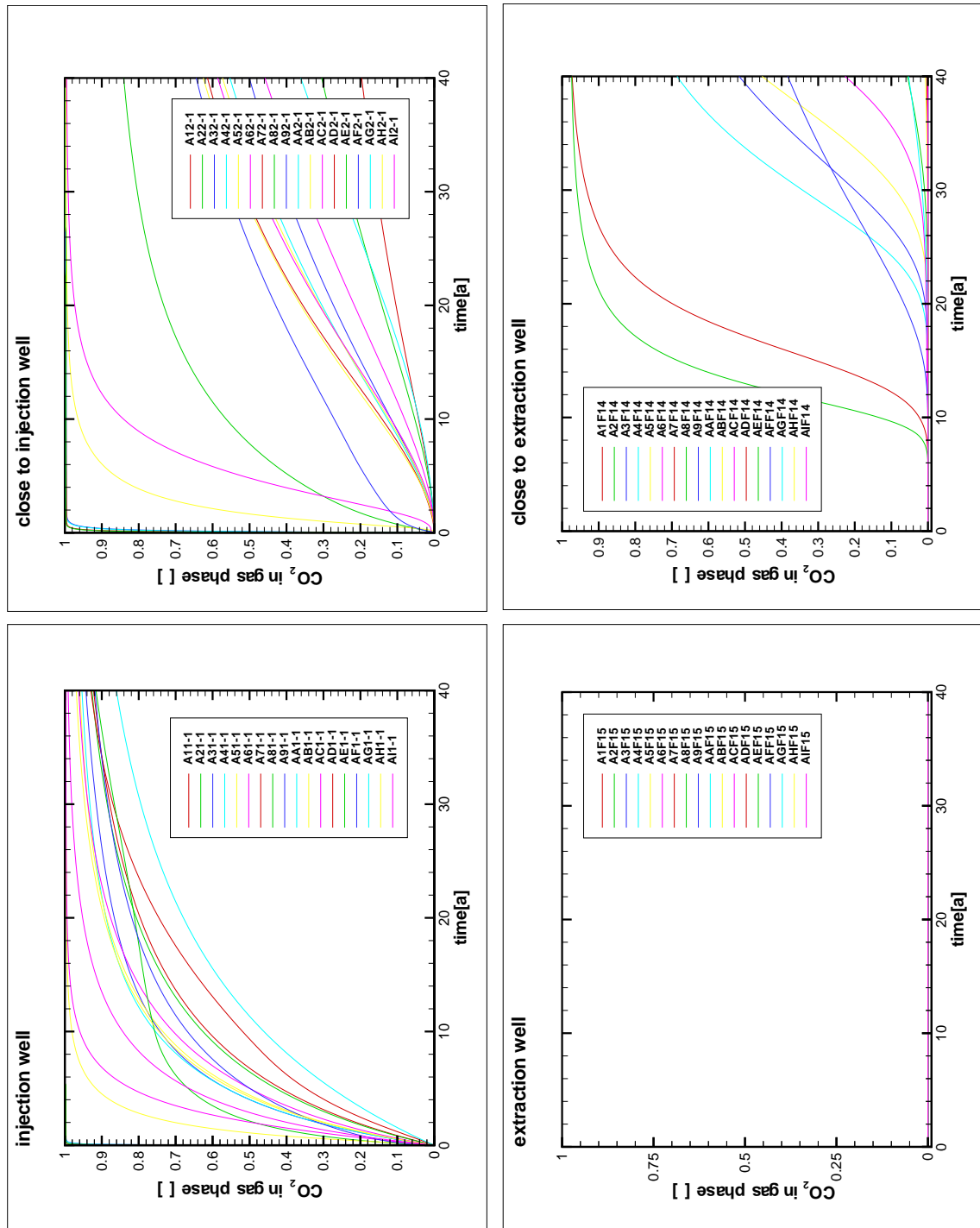


Figure 53: During the extraction and injection phase of the base-case the variation of the  $\text{CO}_2$  mass fraction in the gas phase in time starts at different times and increases with different gradients depending on the distance to the injection site.

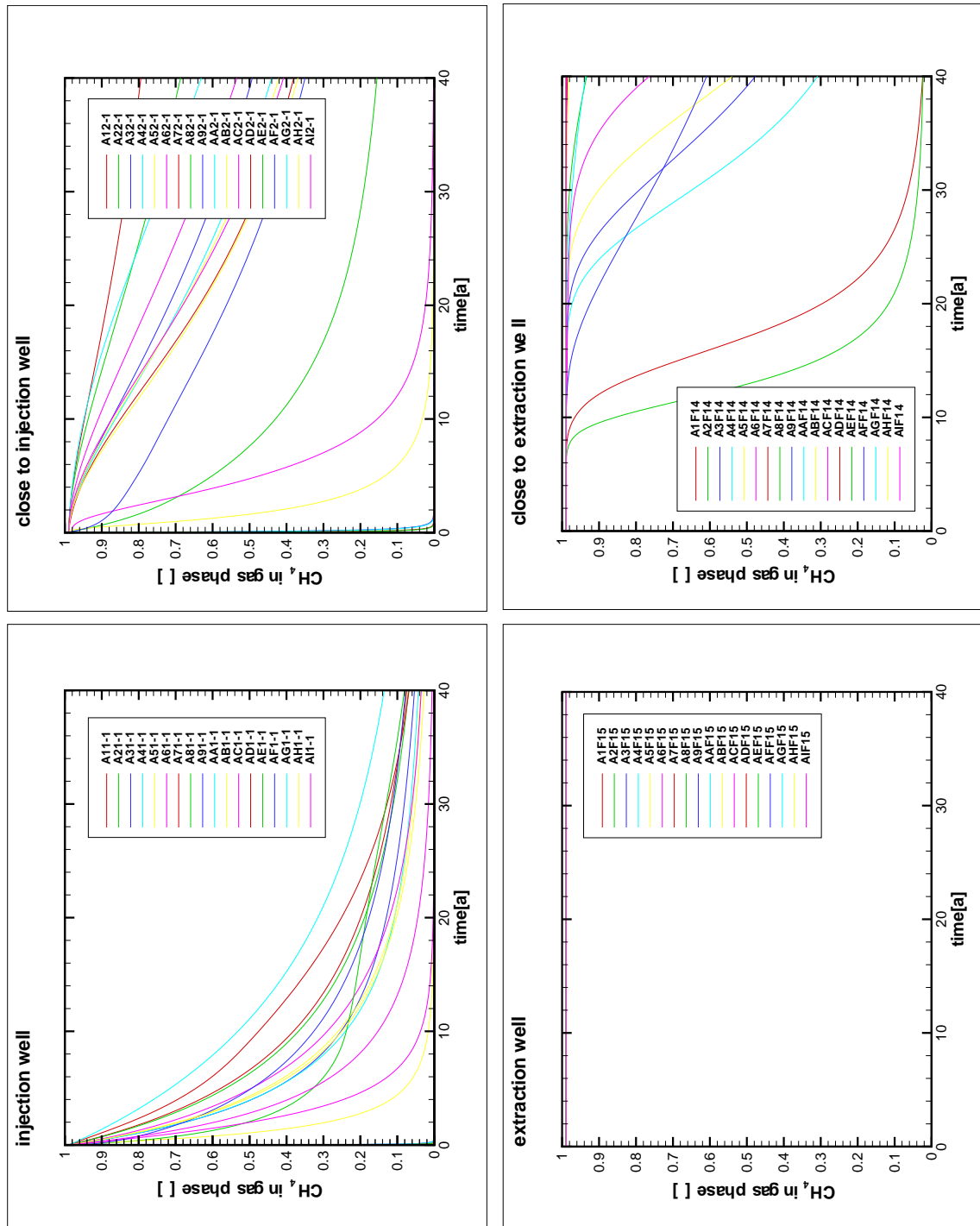


Figure 54: During the extraction and injection phase of the base-case the variation of the  $\text{CH}_4$  mass fraction in the gas phase in time starts at different times and decreases with different gradients depending on the distance to the injection site.

case a10, relaxation phase

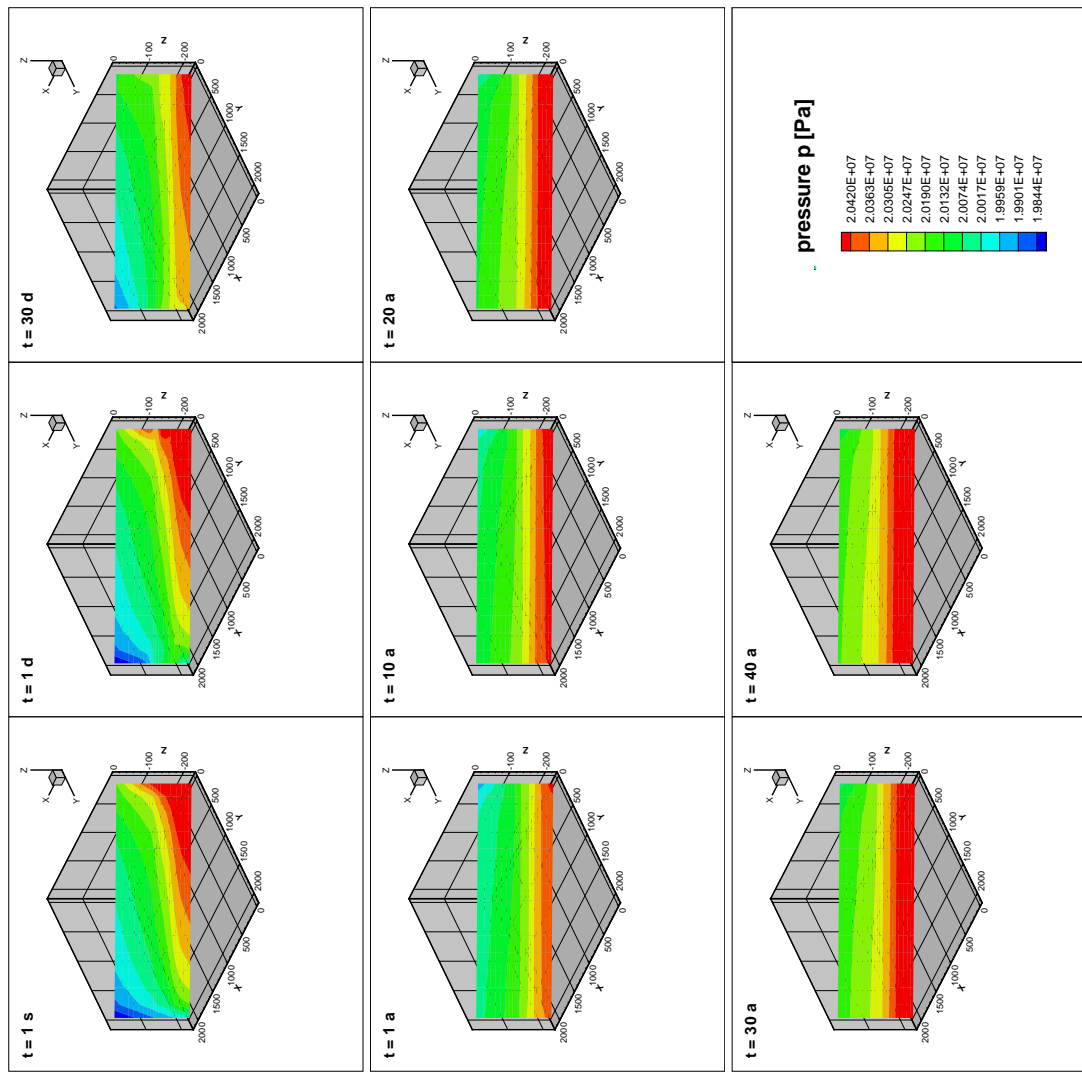


Figure 55: Simulations of the relaxation phase after  $CH_4$  extraction and  $CO_2$  injection for 40 years show the development in time of the pressure in a diagonal slice of the 3D grid.

case a10, relaxation phase

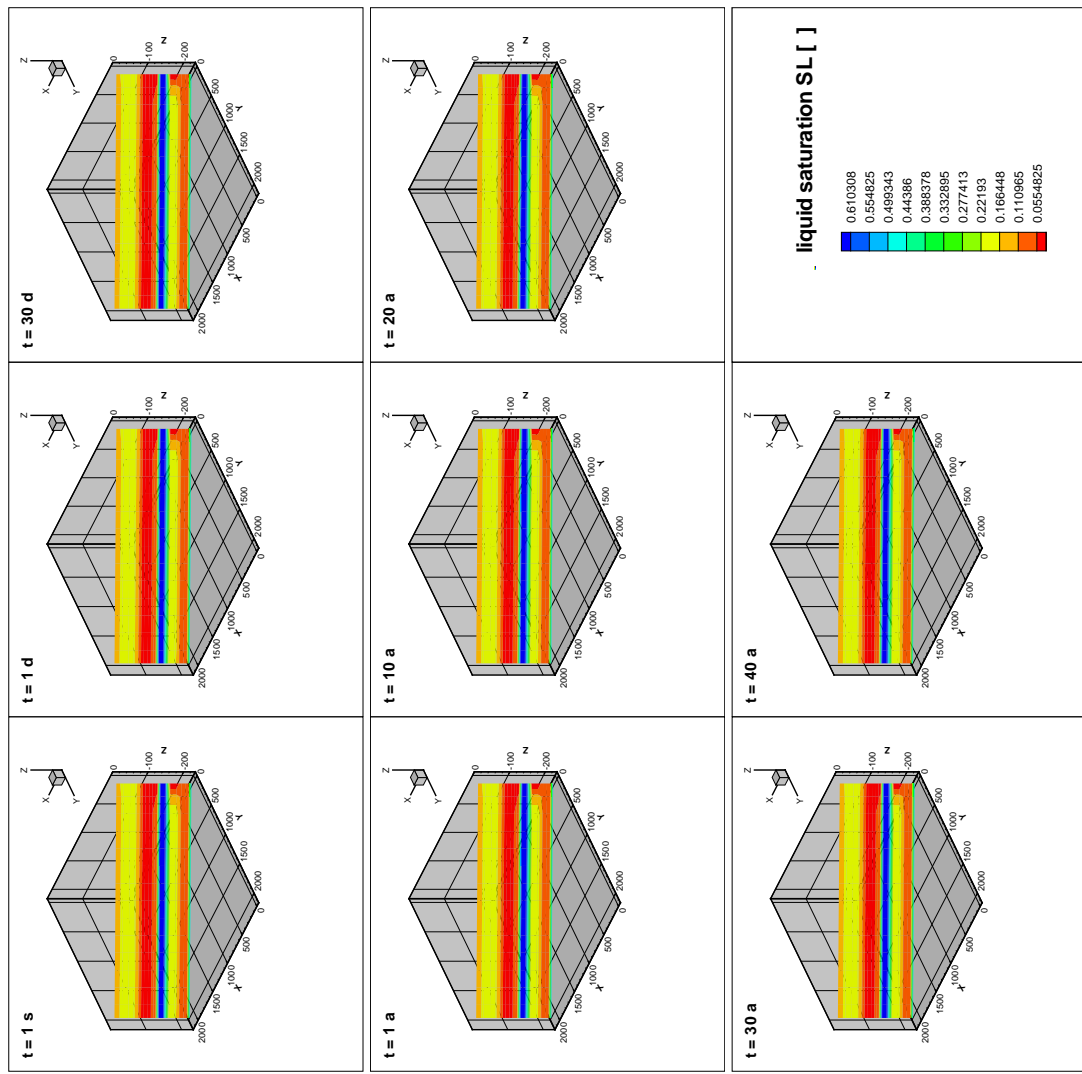


Figure 56: Simulations of the relaxation phase after  $CH_4$  extraction and  $CO_2$  injection for 40 years show the development in time of the liquid saturation in a diagonal slice of the 3D grid.

case a10, relaxation phase

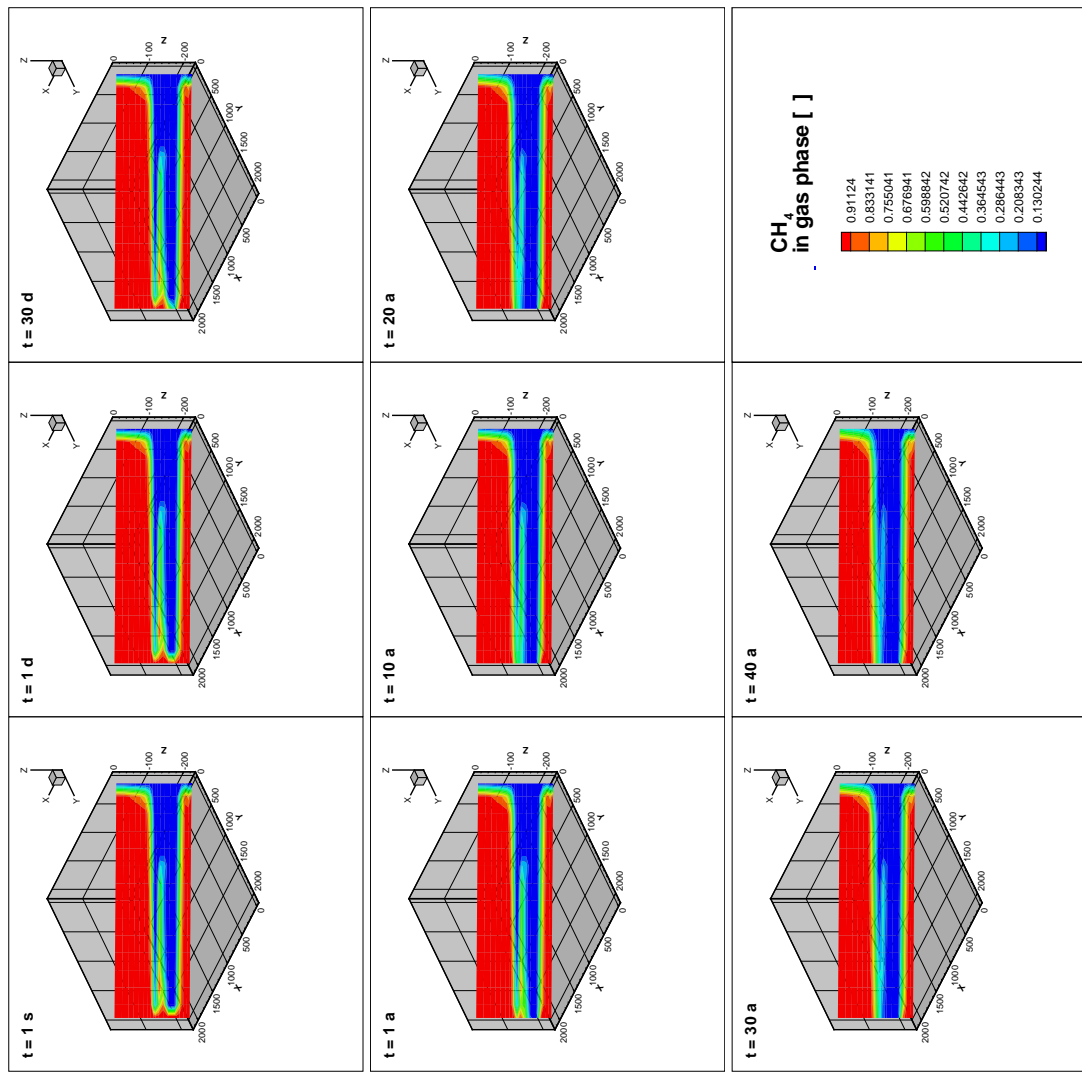


Figure 57: Simulations of the relaxation phase after  $\text{CH}_4$  extraction and  $\text{CO}_2$  injection for 40 years show the development in time of the  $\text{CH}_4$  mass fraction in the gas phase in a diagonal slice of the 3D grid.

case a10, relaxation phase

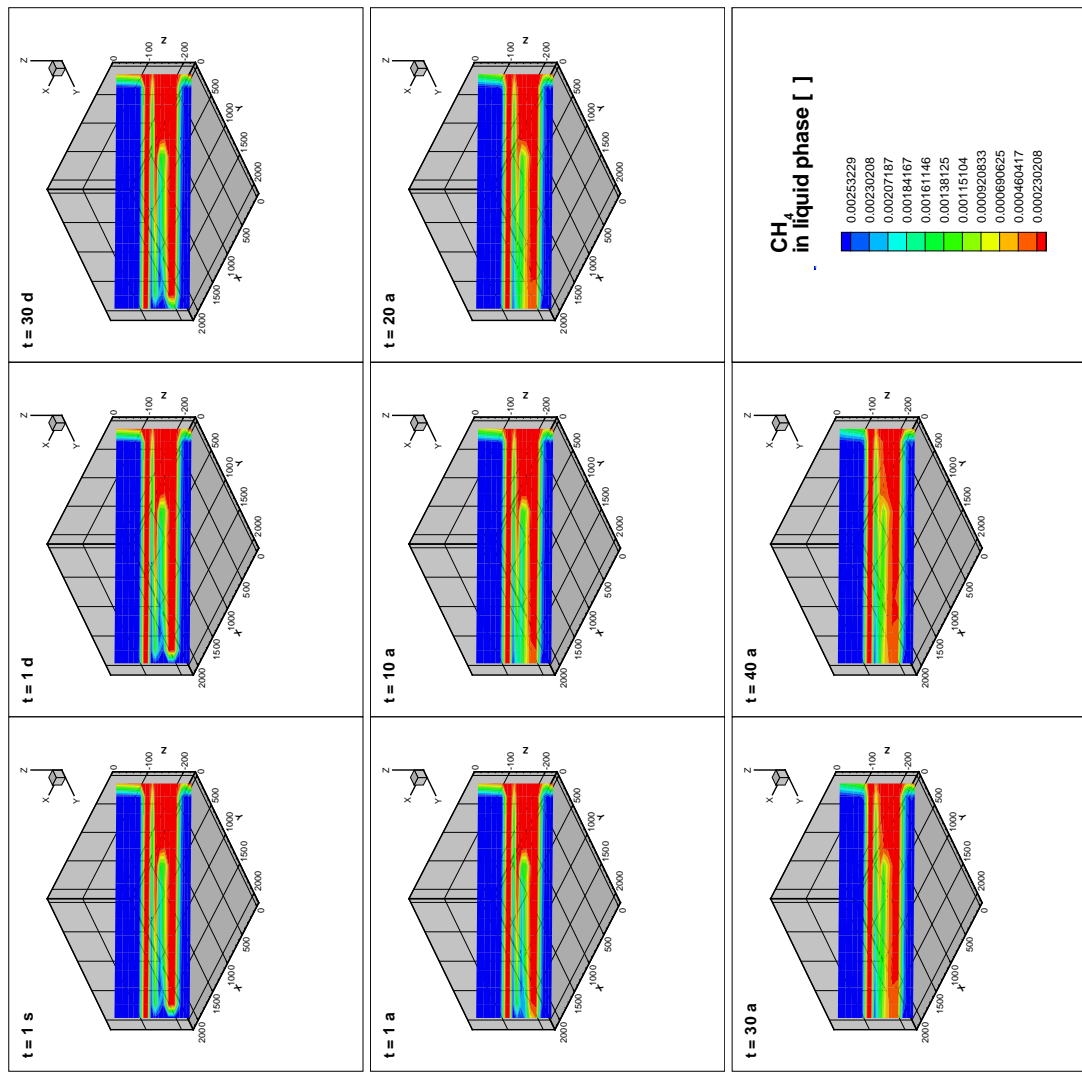


Figure 58: Simulations of the relaxation phase after CH<sub>4</sub> extraction and CO<sub>2</sub> injection for 40 years show the development in time of the CH<sub>4</sub> mass fraction in the liquid phase in a diagonal slice of the 3D grid.

case a10, relaxation phase

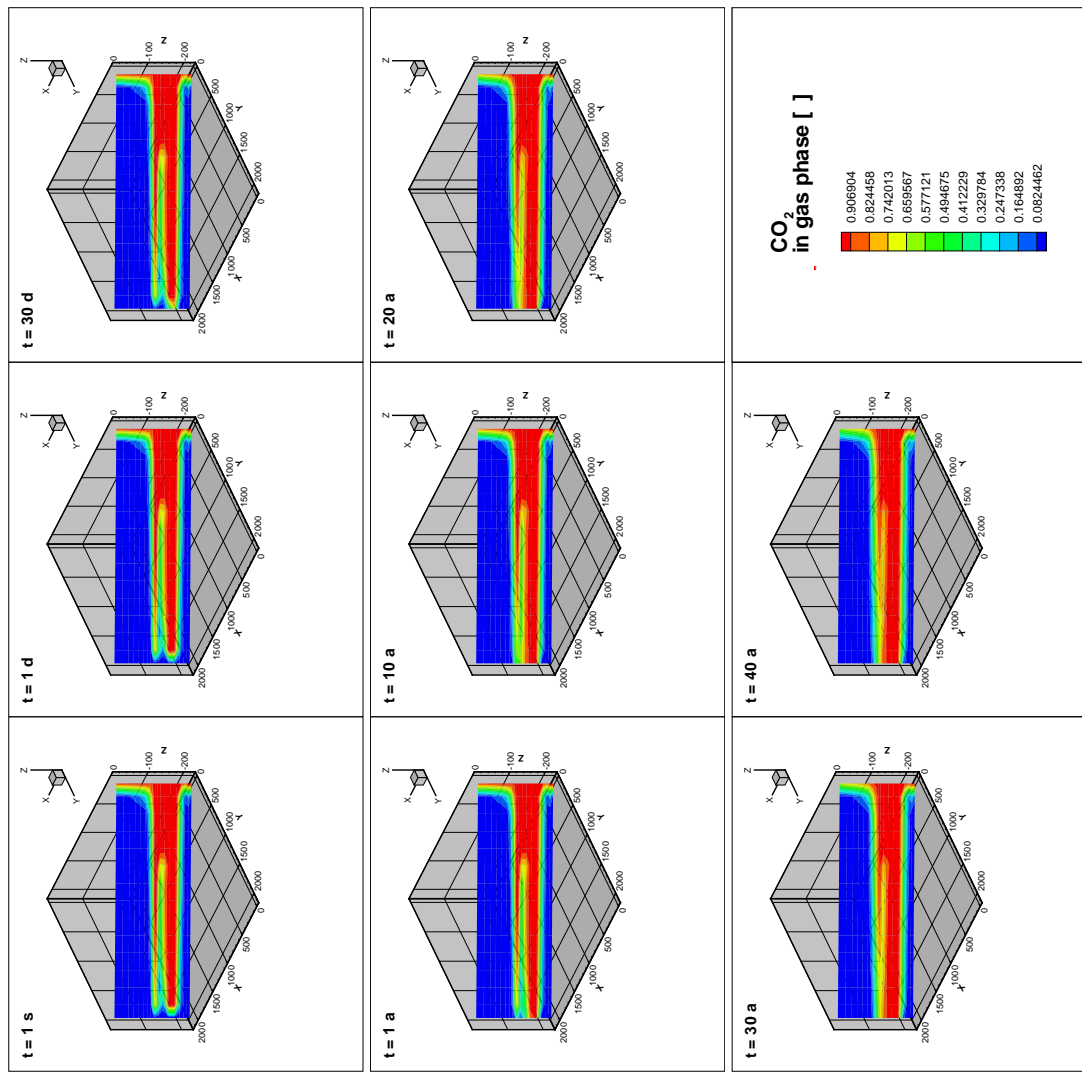


Figure 59: Simulations of the relaxation phase after  $\text{CH}_4$  extraction and  $\text{CO}_2$  injection for 40 years show the development in time of the  $\text{CO}_2$  mass fraction in the gas phase in a diagonal slice of the 3D grid.

case a10, relaxation phase

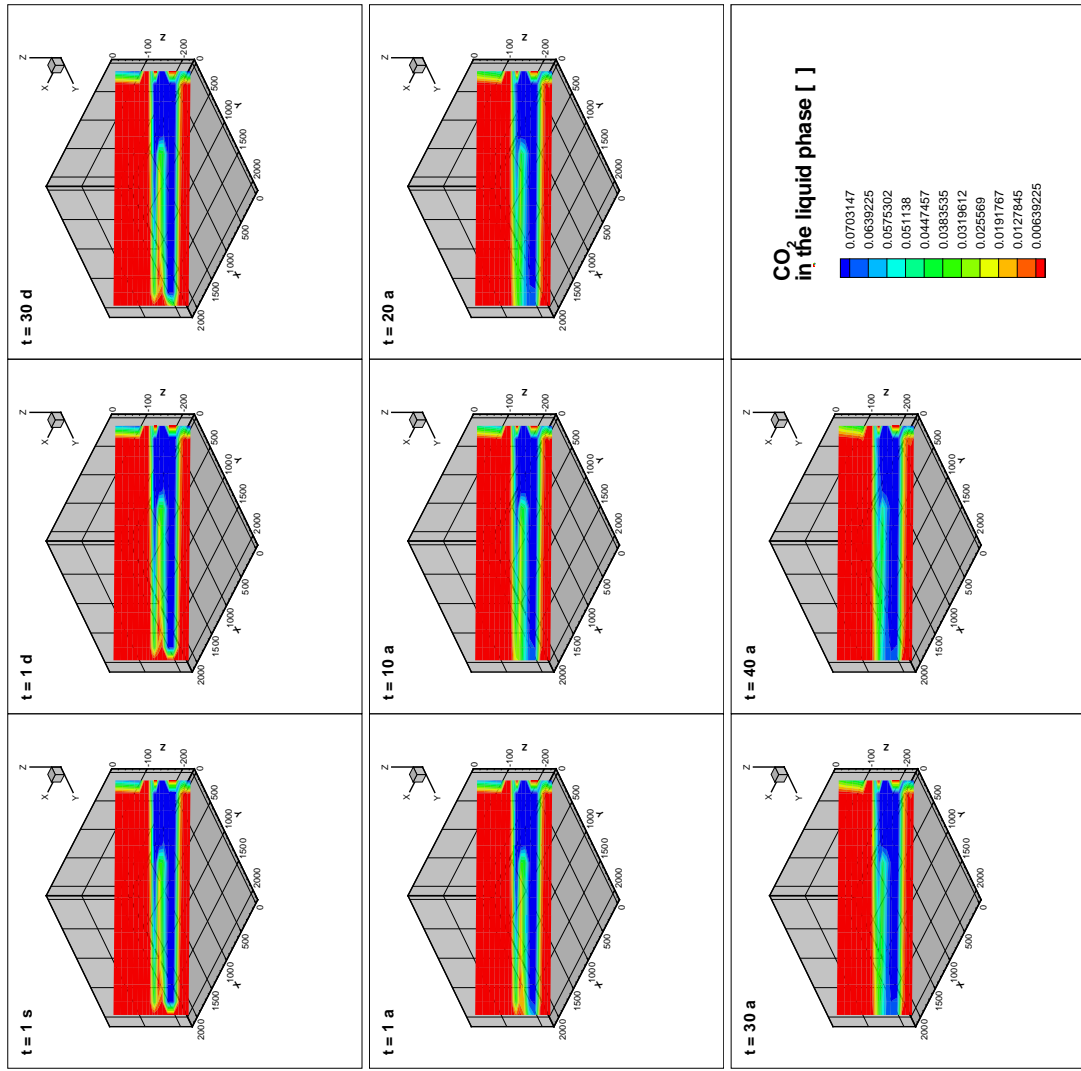


Figure 60: Simulations of the relaxation phase after  $\text{CH}_4$  extraction and  $\text{CO}_2$  injection for 40 years show the development in time of the  $\text{CO}_2$  mass fraction in the liquid phase in a diagonal slice of the 3D grid.

**t = 1 a**

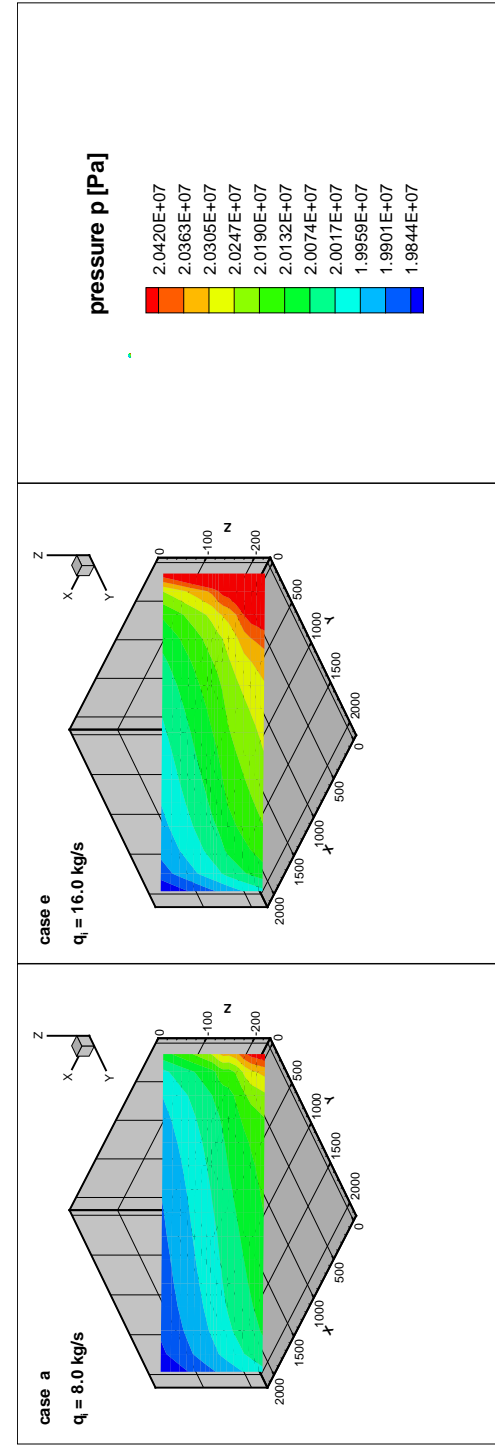
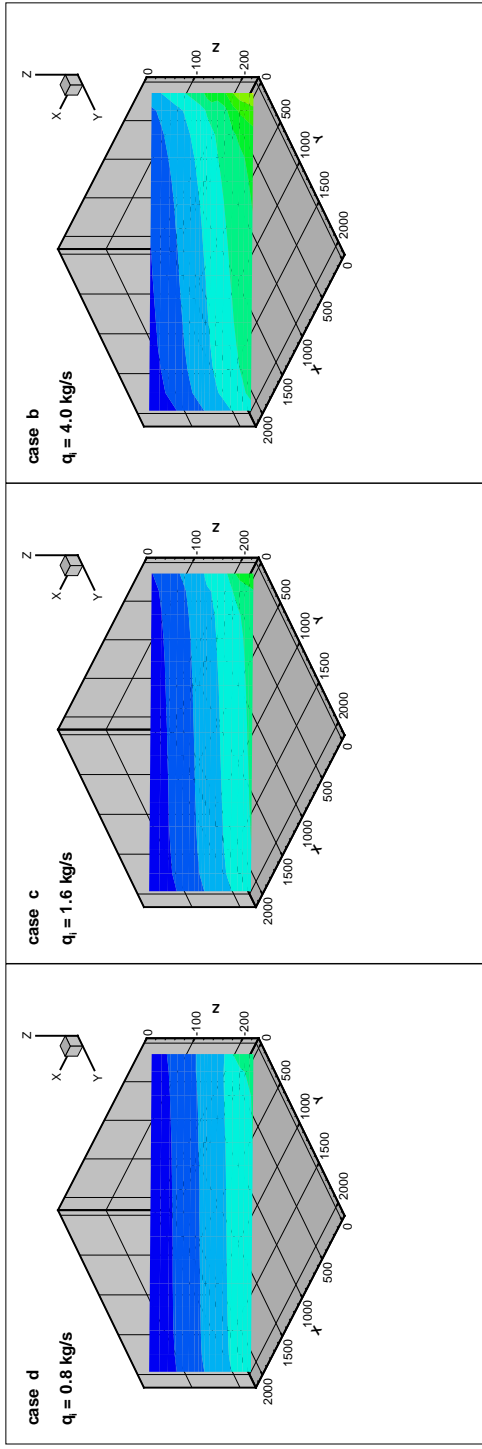


Figure 61: For the analysis of the effect of the injection rate  $Q$ ,  $Q$  is varied, ranging from  $0.8 \text{ kg/s}$  to  $16.0 \text{ kg/s}$ . The simulations of  $\text{CH}_4$  extraction and  $\text{CO}_2$  injection over 1 year show the development of pressure  $p$  in time in the 3D grid.

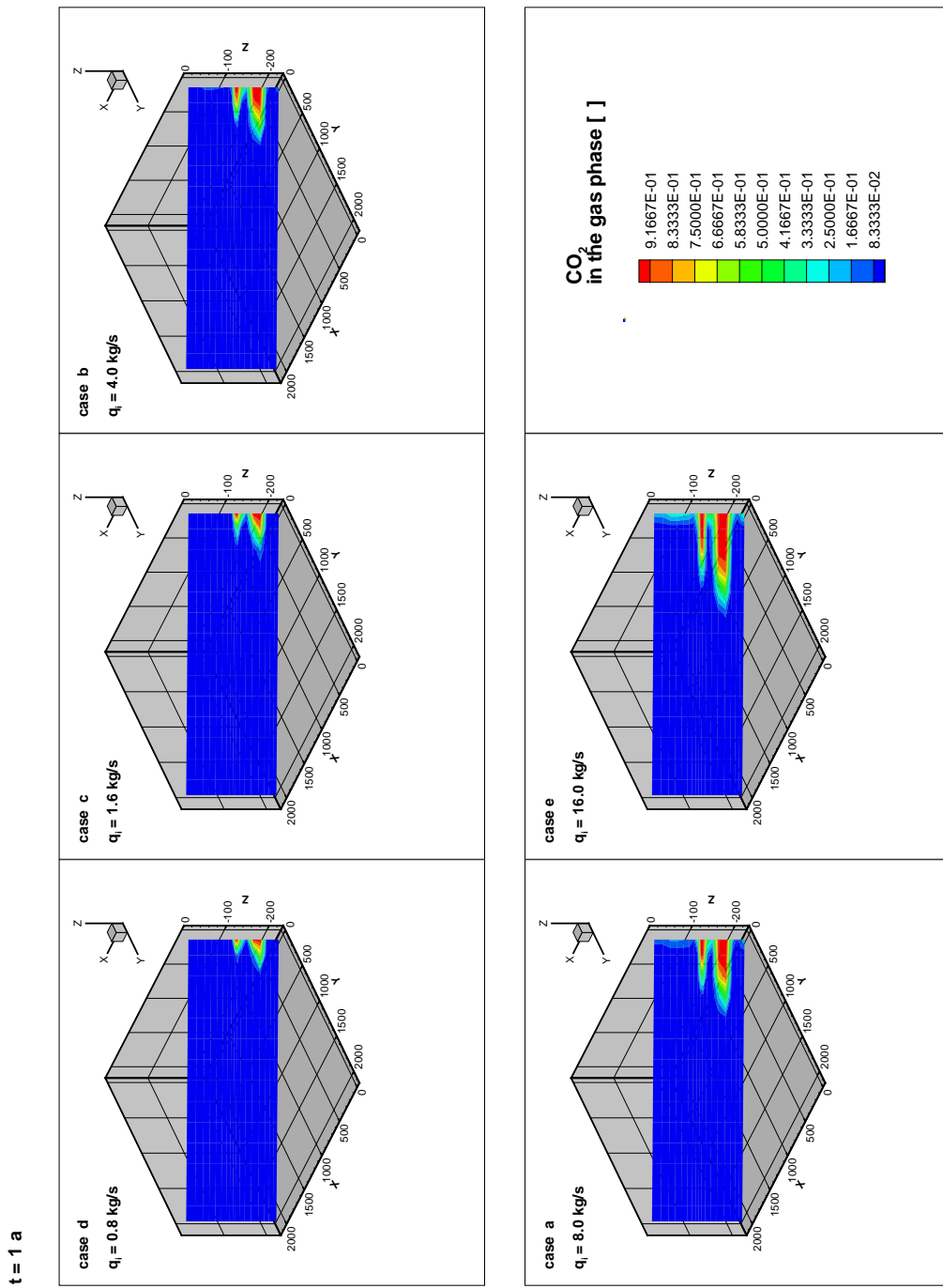


Figure 62: For the analysis of the effect of the injection rate  $Q$ ,  $Q$  was varied, ranging from 0.8 kg/s to 16.0 kg/s. The simulations of CH<sub>4</sub> extraction and CO<sub>2</sub> injection over 1 year show the development of CO<sub>2</sub> mass fraction in the gas phase in time in the 3D grid.

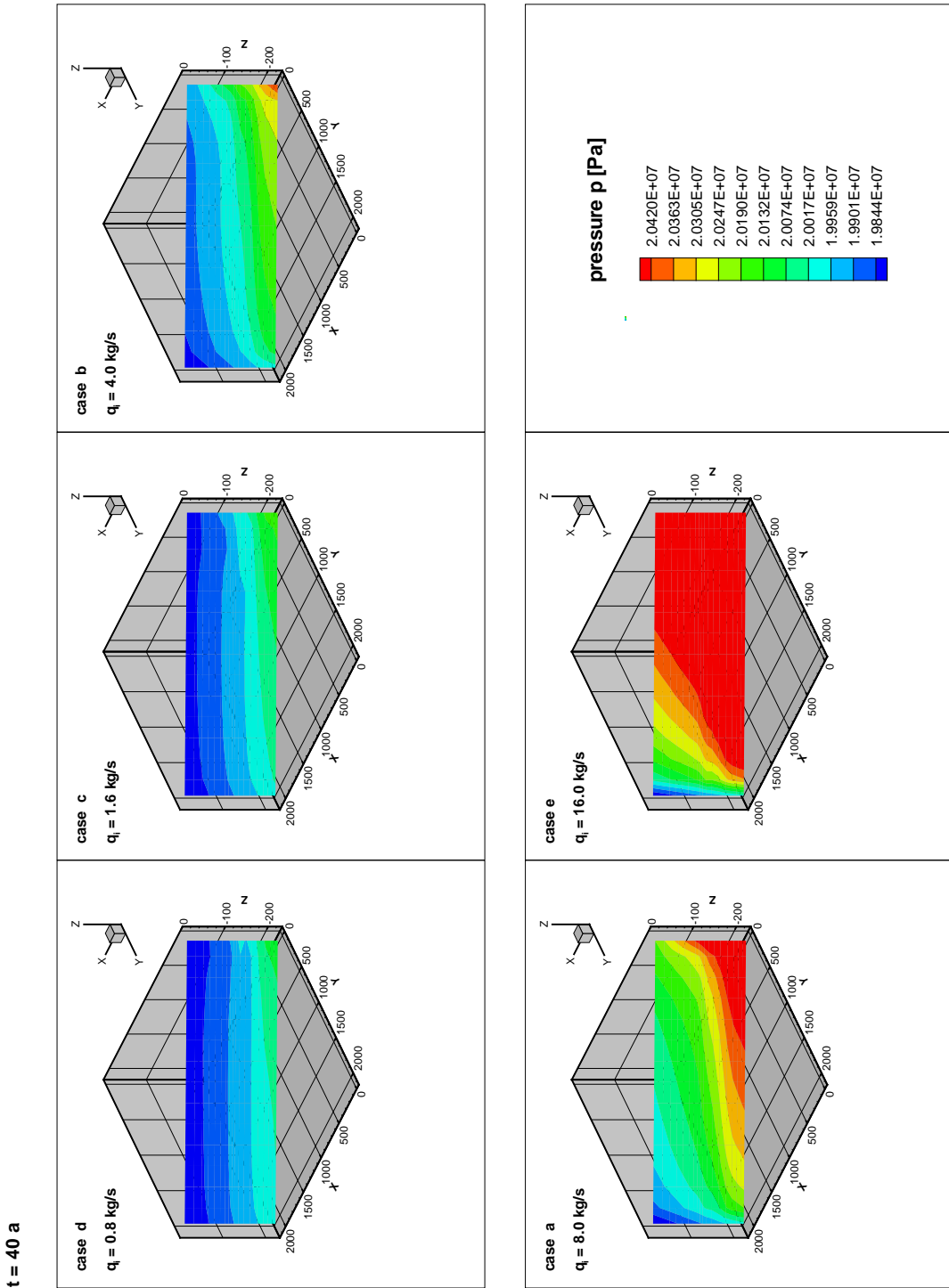


Figure 63: For the analysis of the effect of the injection rate  $Q$ ,  $Q$  was varied, ranging from  $0.8 \text{ kg/s}$  to  $16.0 \text{ kg/s}$ . The simulations of  $\text{CH}_4$  extraction and  $\text{CO}_2$  injection over 40 years show the development of pressure  $p$  [Pa] in time in the 3D grid.

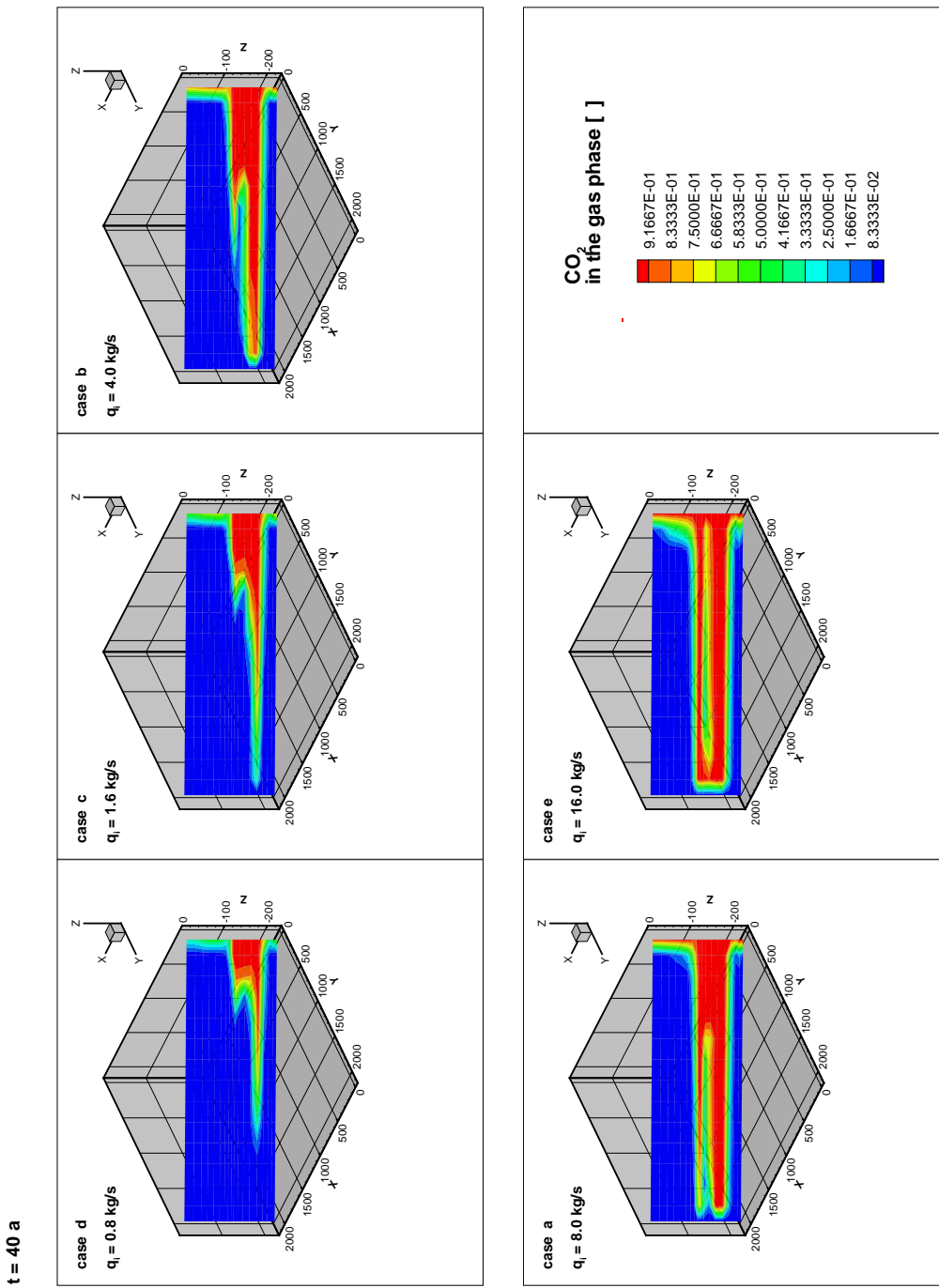


Figure 64: For the analysis of the effect of the injection rate  $Q$ ,  $Q$  was varied, ranging from  $0.8 \text{ kg/s}$  to  $16.0 \text{ kg/s}$ . The simulations of  $\text{CH}_4$  extraction and  $\text{CO}_2$  injection over 40 years show the development of  $\text{CO}_2$  mass fraction in the gas phase in time in the 3D grid.

**t = 1 a**

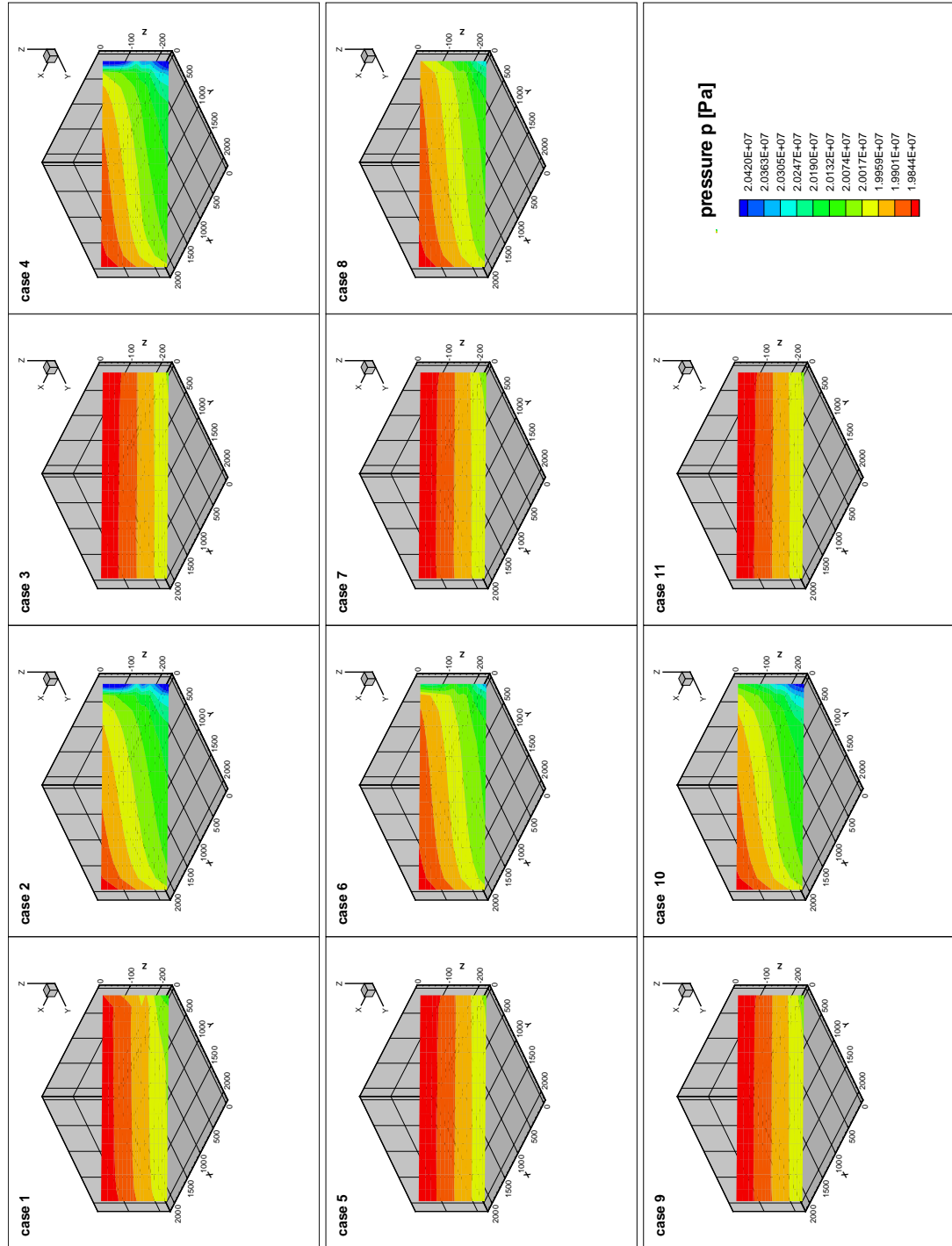


Figure 65: The vertical diagonal slice of the 3D simulations after 1 year of the Cases a1 to a11 shows the dependence of the spatial pressure evolution due to different values of high and low permeabilities in the units.

**t = 1 a**

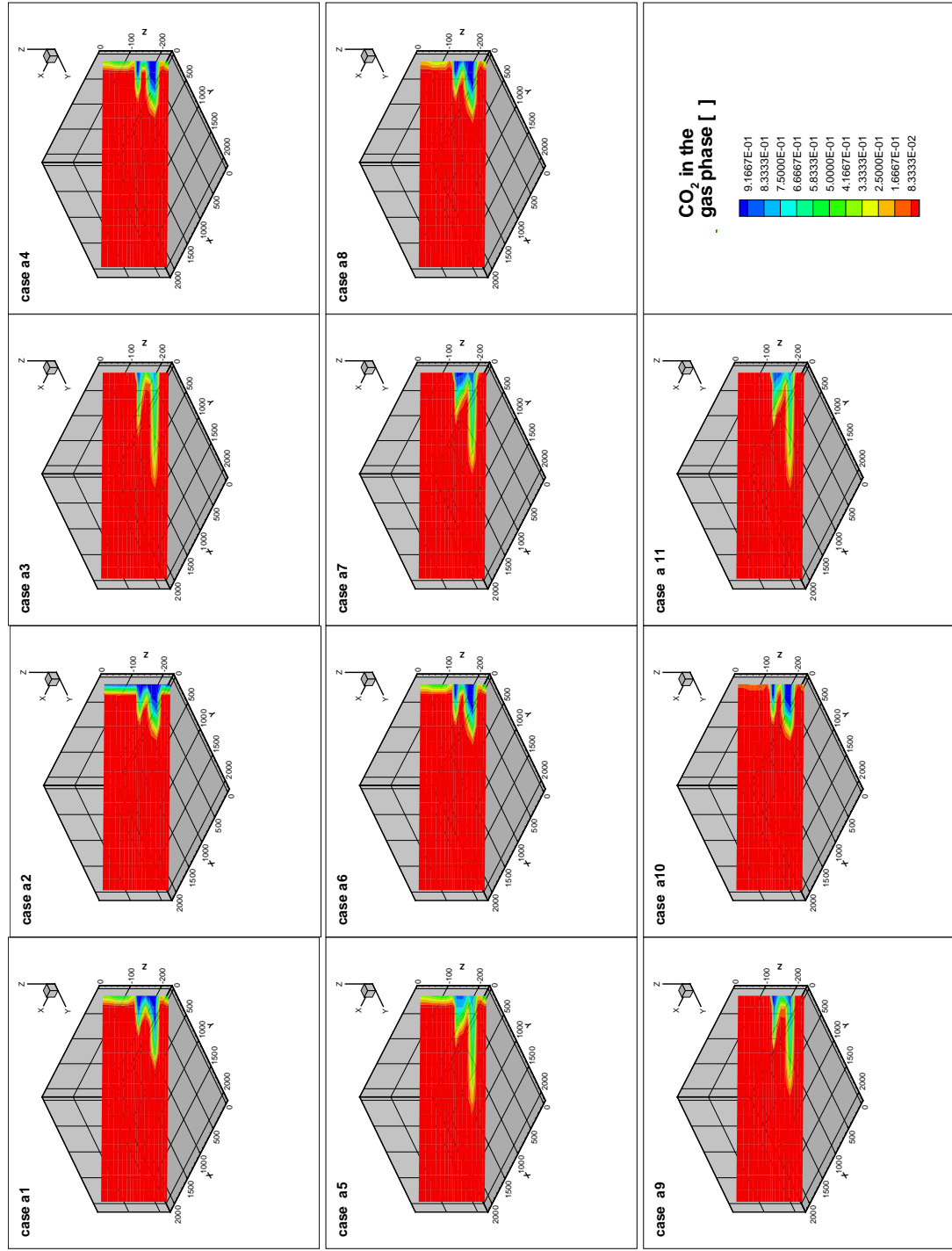


Figure 66: The vertical diagonal slice of the 3D simulations after 1 year of the Cases a1 to a11 shows the dependence of the spatial evolution of the CO<sub>2</sub> mass fraction in the gas phase due to different values of high and low permeabilities in the units.

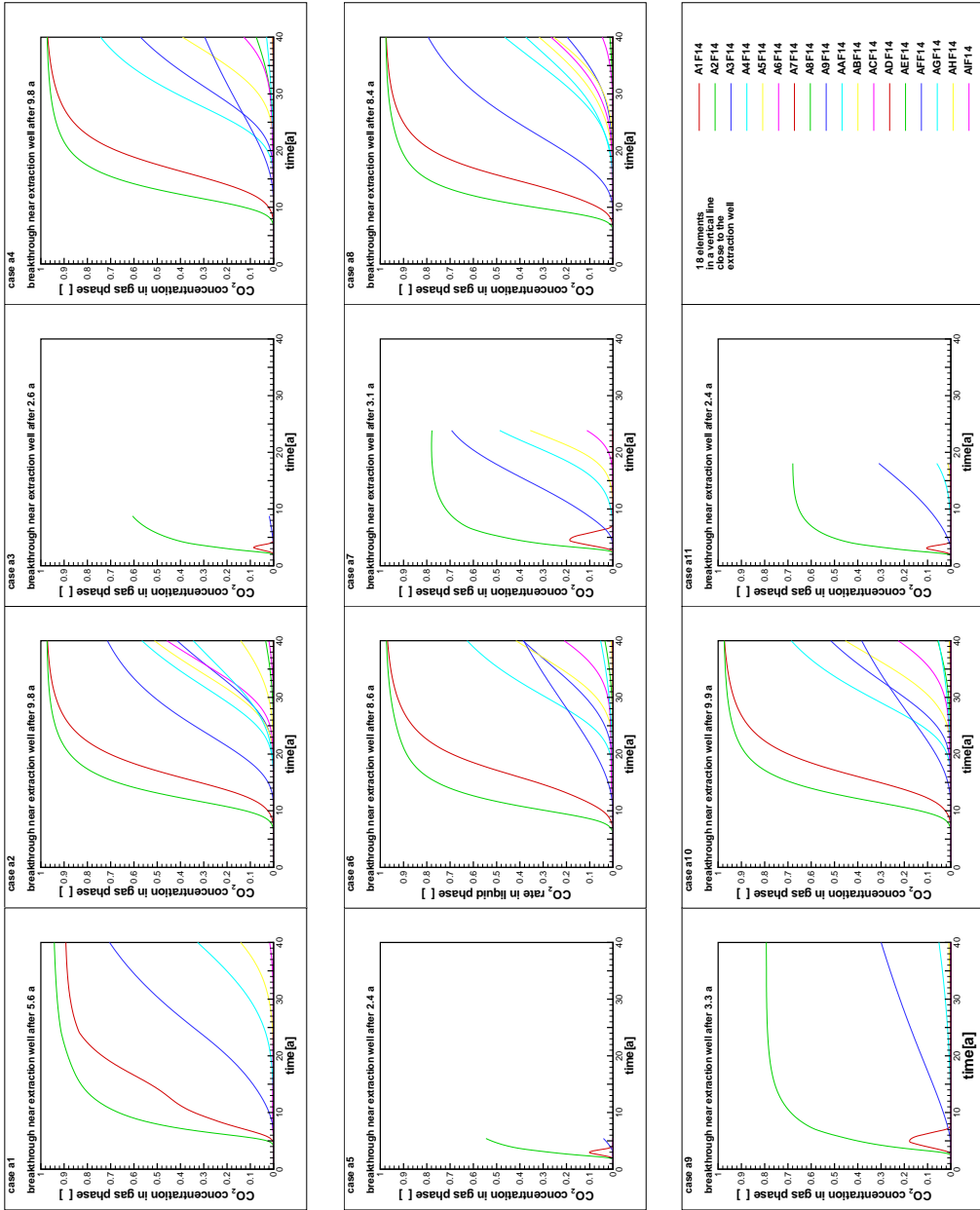


Figure 67: The breakthrough is studied in the 3D simulation cases a1 to a11 by determining the  $\text{CO}_2$  mass fraction in the gas phase in 18 gridblocks in a vertical column, neighboring the production well. The blocks A9F14 and AAF14 (upper and lower gridblock of Zyk13) and ADF14 and AEF14 (upper and lower gridblock of Z9–11) shows the highest and fastest  $\text{CO}_2$  contamination.

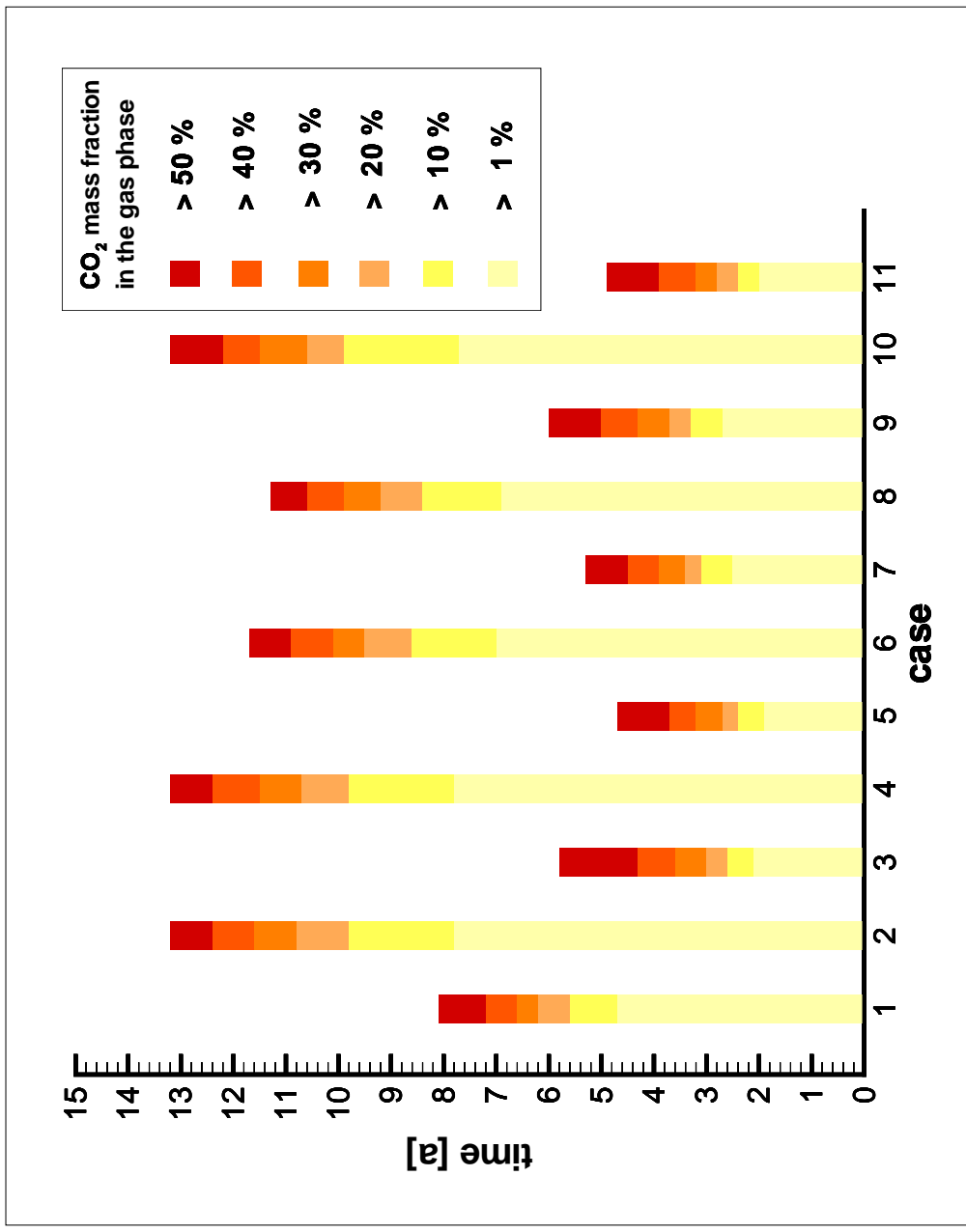


Figure 68: The CO<sub>2</sub> arrival in the neighboring gridblock of the production well is first observed in the bottom layer of the high-permeability layer Z9–11. Different colors show the development of the increasing amount of CO<sub>2</sub> mass fraction in the gas phase. The 11 cases differ in the permeabilities of the layers (see Table 8). In the simulated cases the breakthroughs occur between a few years and more than ten years. The increase from obtaining 1 % to reaching 50 % takes place within about 2 a to 5 a.

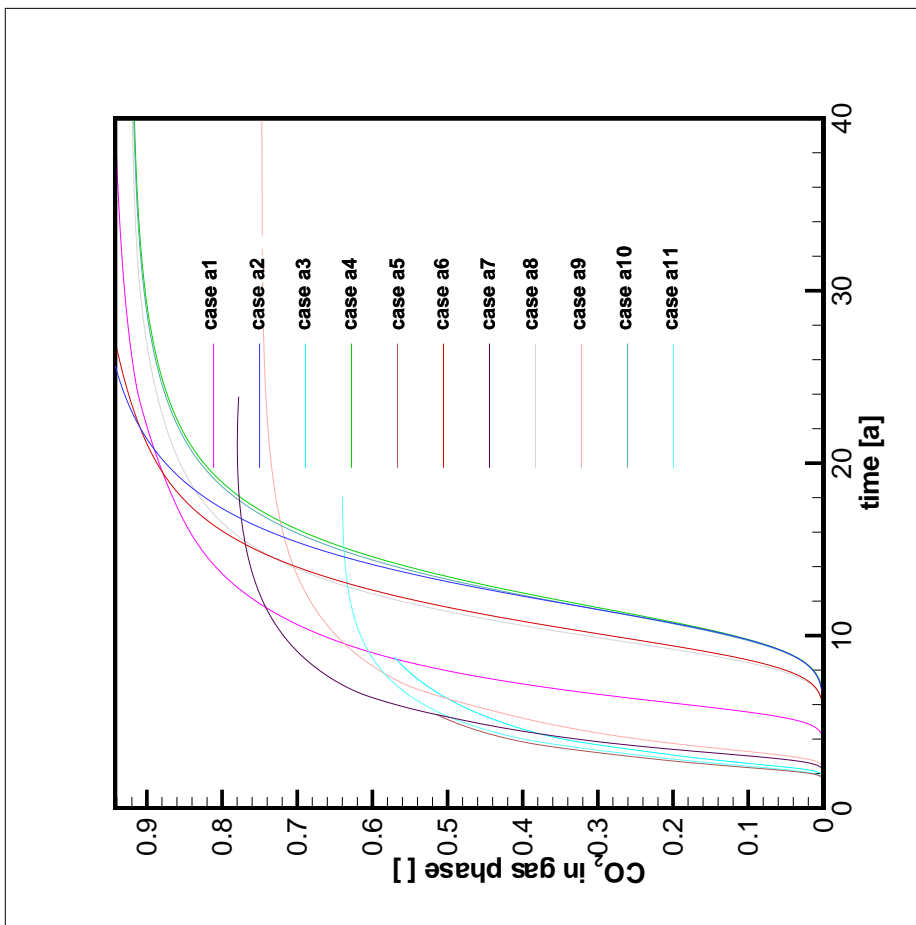


Figure 69: The CO<sub>2</sub> mass fraction in the gas phase of the bottom gridblock AEF14 of the high-permeability layer Z9–11 reaches the 10 % limit in the simulated cases within about 2 a to 10 a. The 11 cases differ in the permeabilities of the layers (see Table 8).

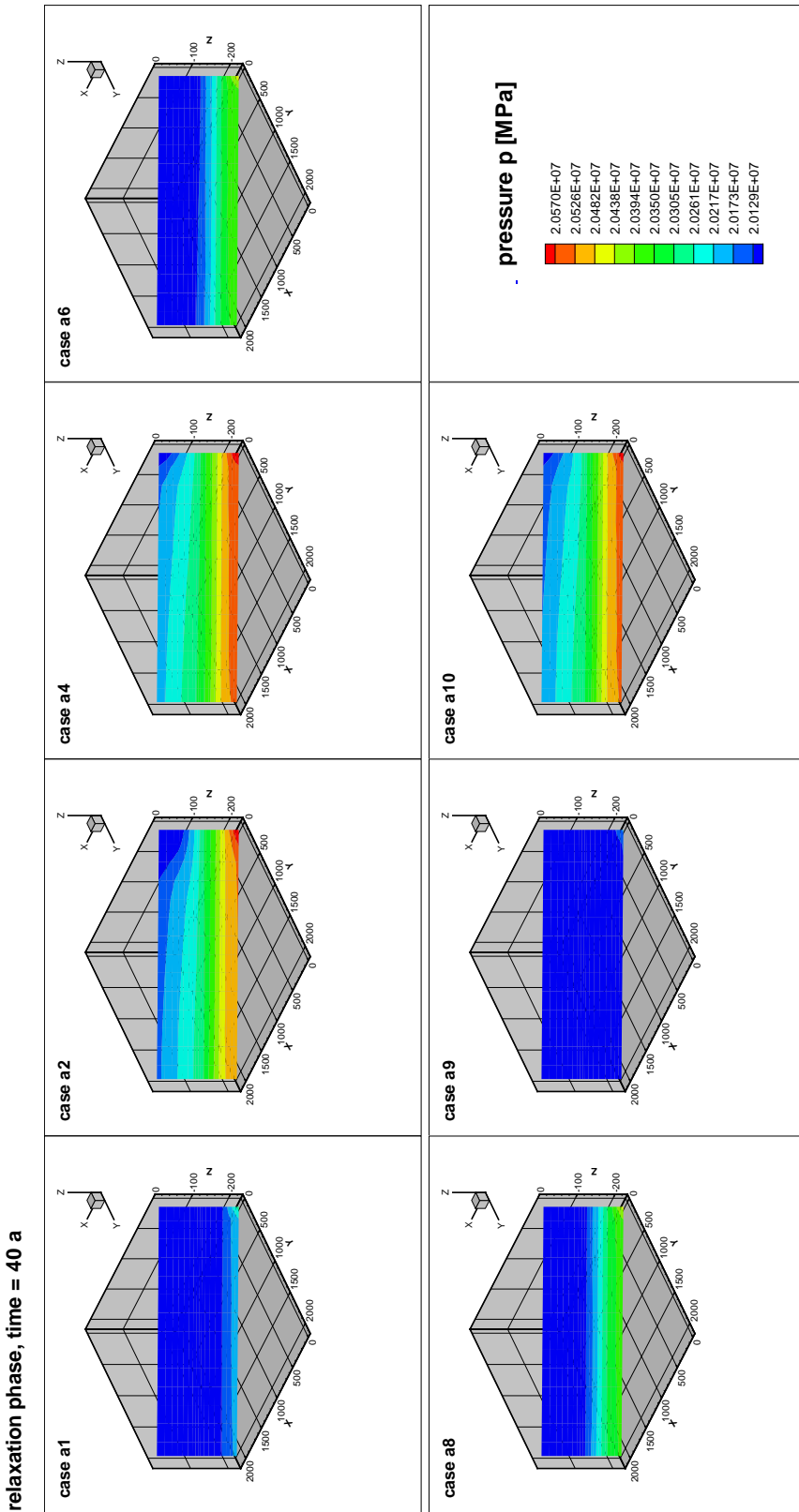


Figure 70: A 40 years long relaxation phase after CH<sub>4</sub> extraction and CO<sub>2</sub> injection shows the pressure distribution in a diagonal slice of the 3D grid for seven cases.

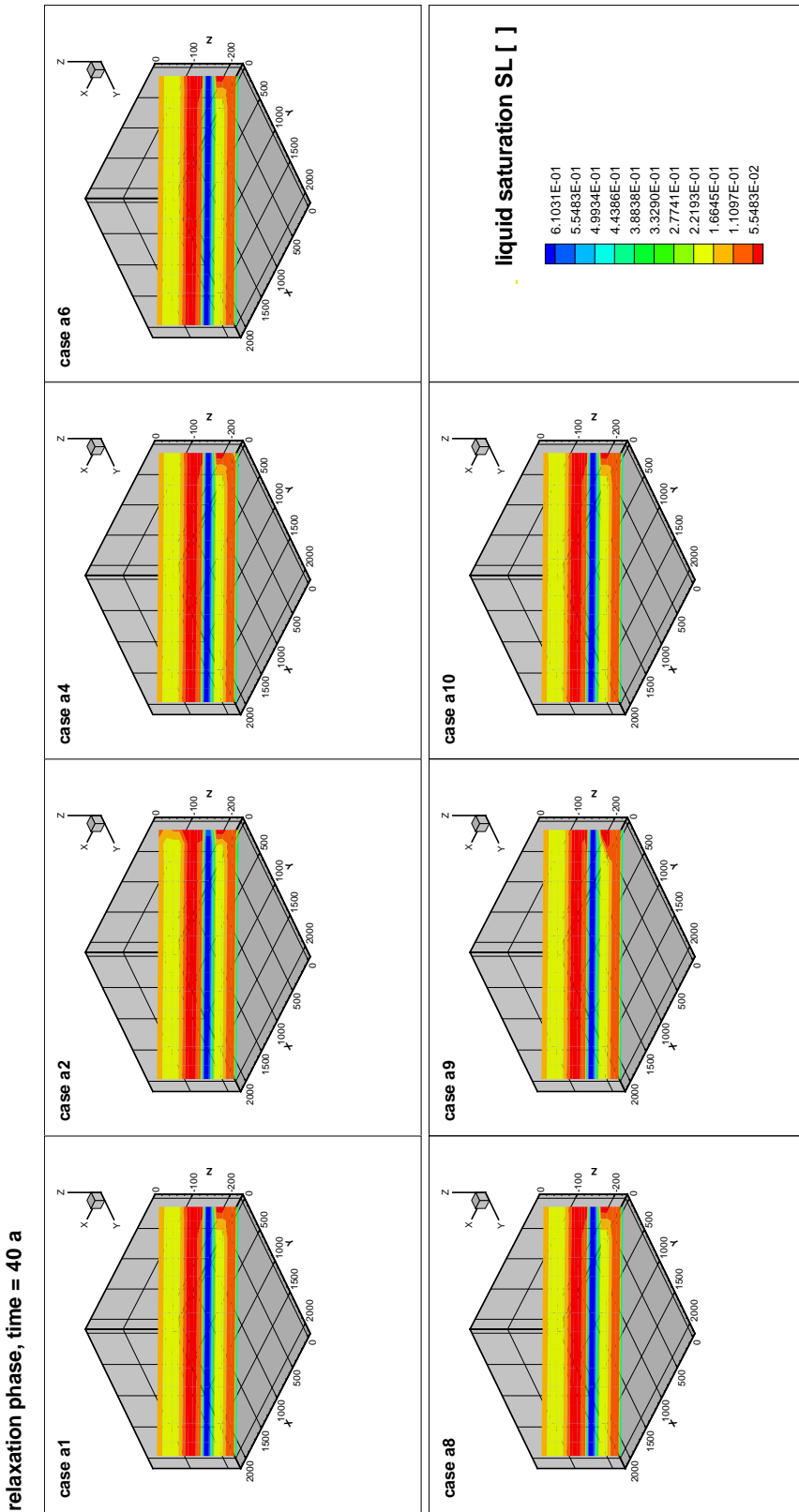


Figure 71: A 40 years long relaxation phase after  $CH_4$  extraction and  $CO_2$  injection shows the distribution of the liquid saturation  $SL$  in a diagonal slice of the 3D grid for seven cases.

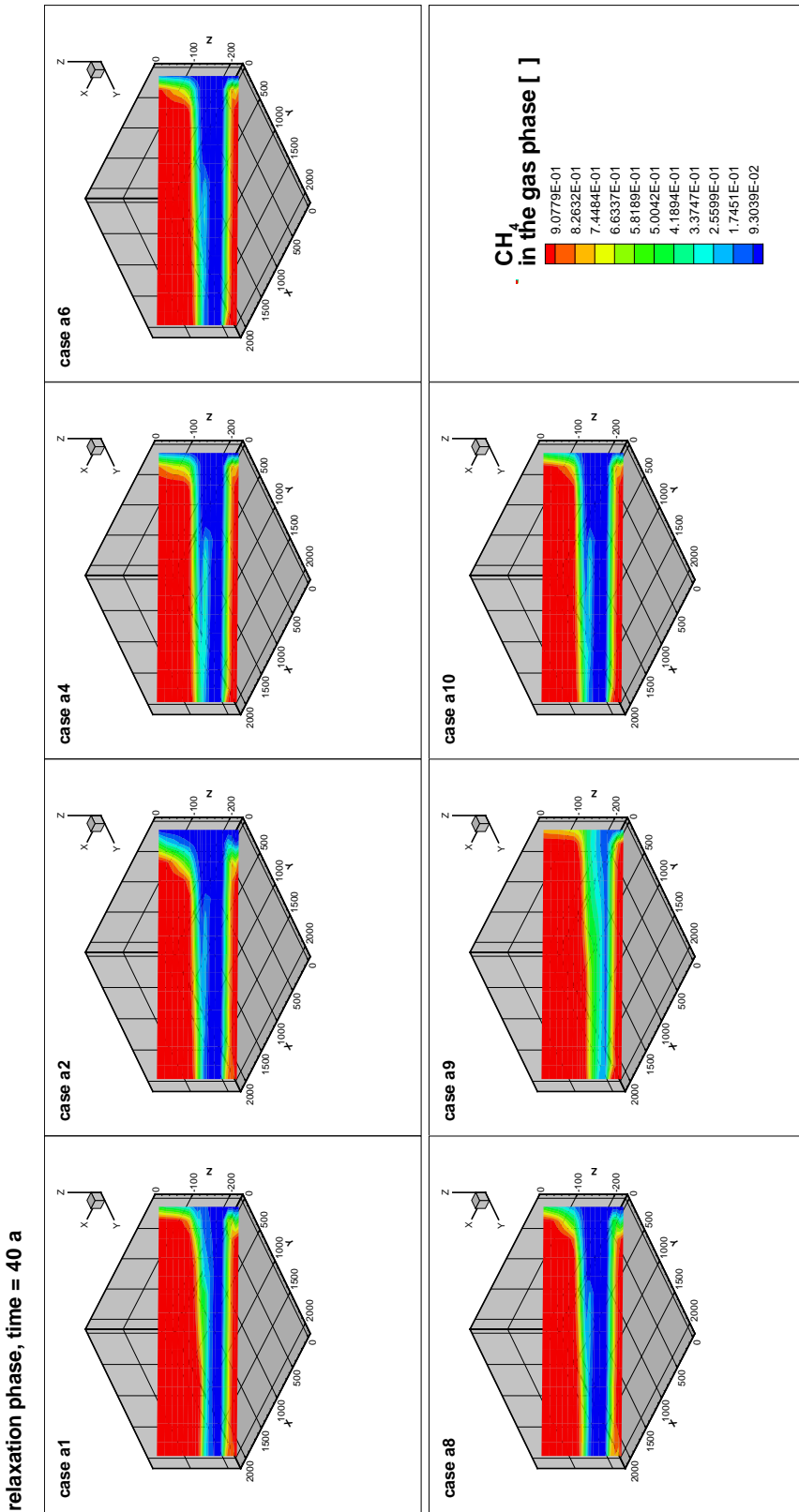


Figure 72: A 40 years long relaxation phase after CH<sub>4</sub> extraction and CO<sub>2</sub> injection shows the distribution of the CH<sub>4</sub> mass fraction in the gas phase in a diagonal slice of the 3D grid for seven cases.

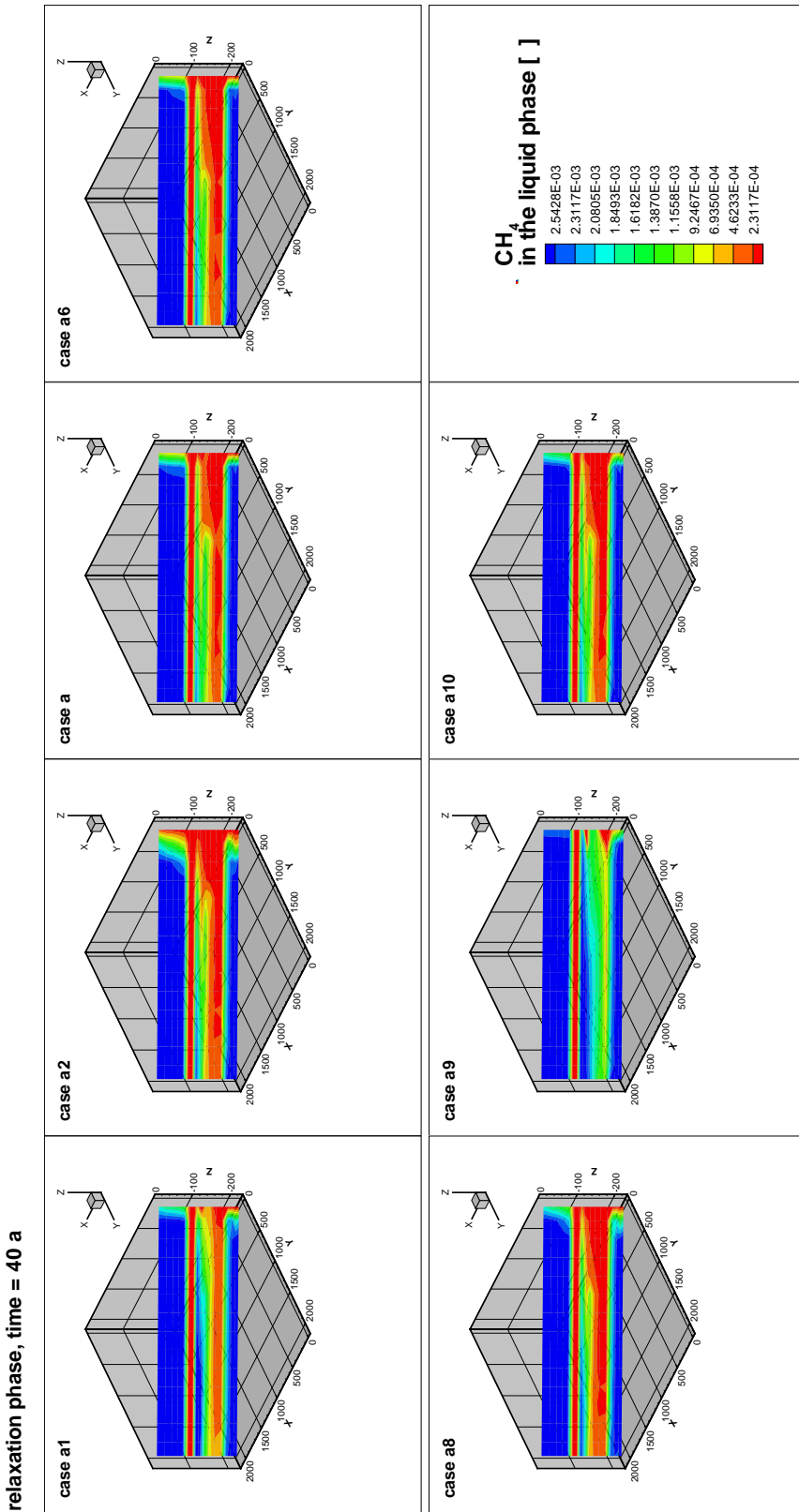


Figure 73: A 40 years long relaxation phase after CH<sub>4</sub> mass fraction and CO<sub>2</sub> injection shows the distribution of the CH<sub>4</sub> mass fraction in the liquid phase in a diagonal slice of the 3D grid for seven cases.

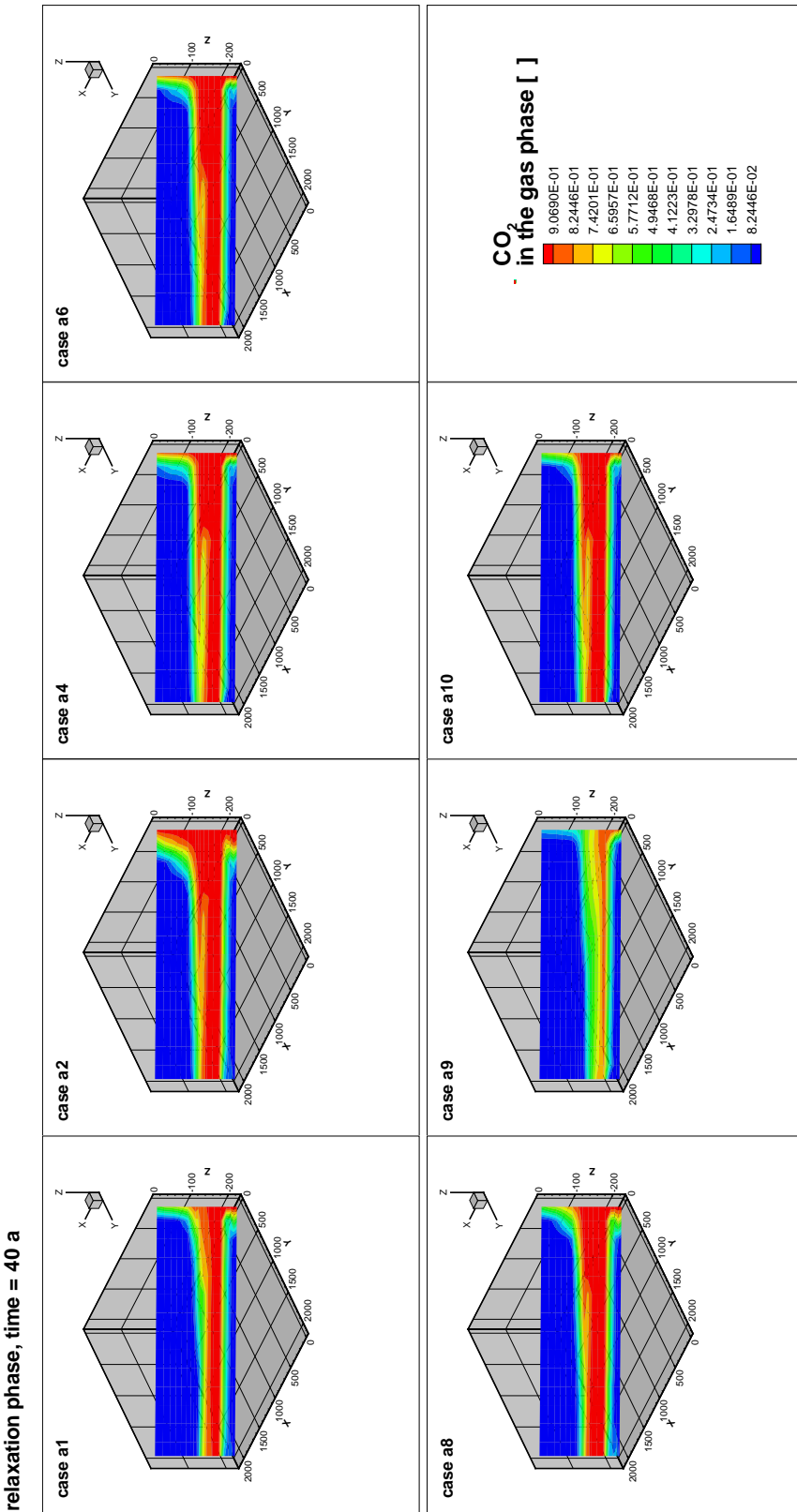


Figure 74: A 40 years long relaxation phase after CH<sub>4</sub> mass fraction and CO<sub>2</sub> injection shows the distribution of the CO<sub>2</sub> mass fraction in the gas phase in a diagonal slice of the 3D grid for seven cases.

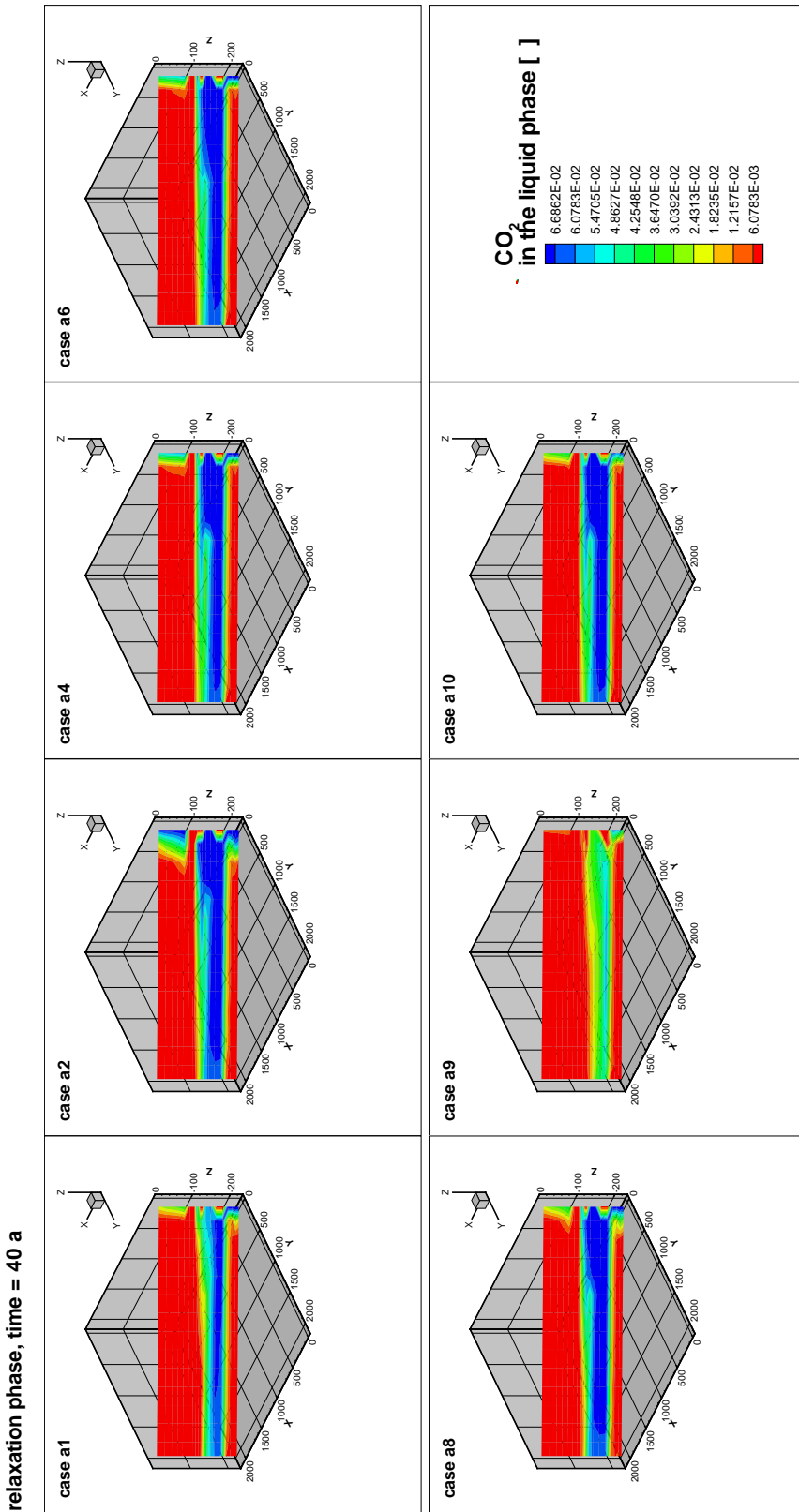


Figure 75: A 40 years long relaxation phase after CH<sub>4</sub> extraction and CO<sub>2</sub> injection shows the distribution of the CO<sub>2</sub> mass fraction in the liquid phase in a diagonal slice of the 3D grid for seven cases.

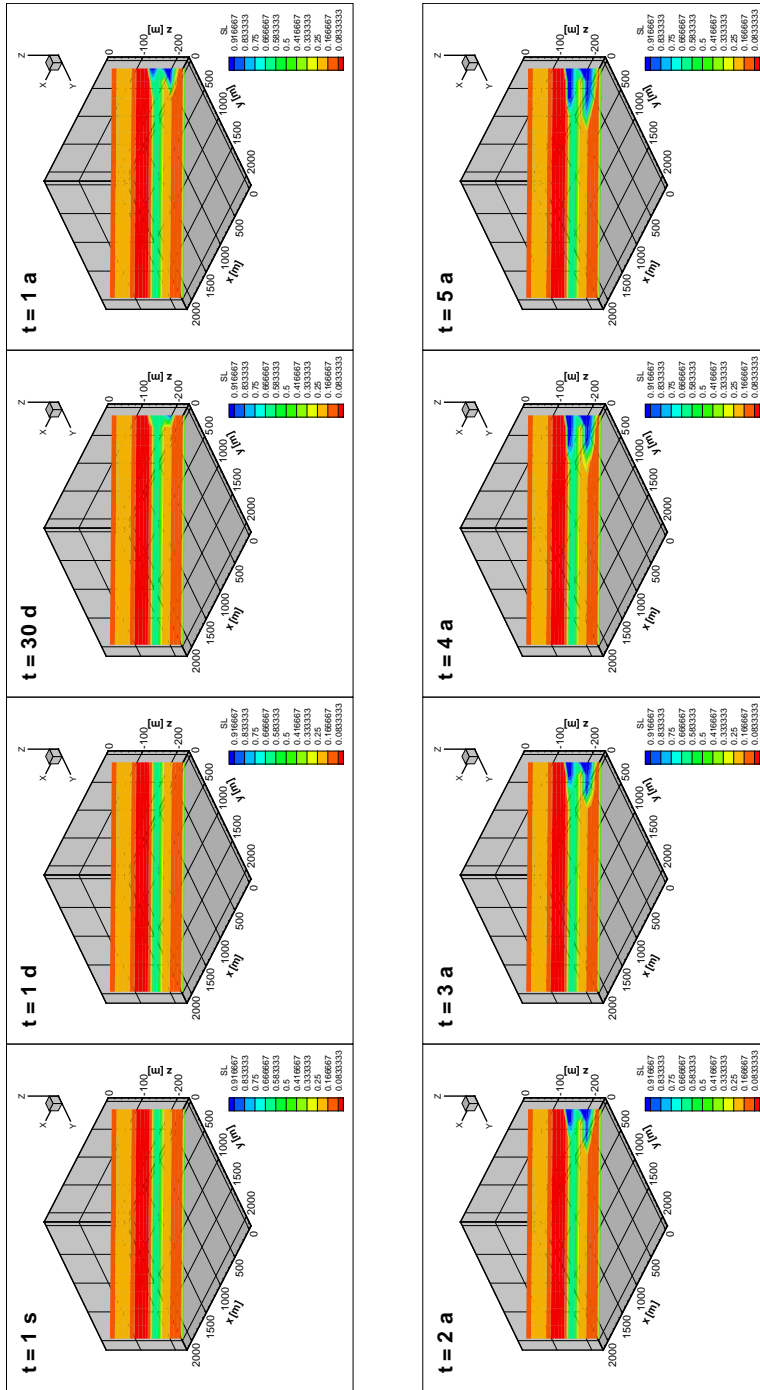


Figure 76: In Case f the layers Zyk13 and Zyk9-11 are blocked with a  $H_2O$  injection rate of 0.7523 kg/s and 2.1567 kg/s, (for each gridblock) (see Table 10). The development of the liquid saturation SL in this case is shown for 8 different time periods.

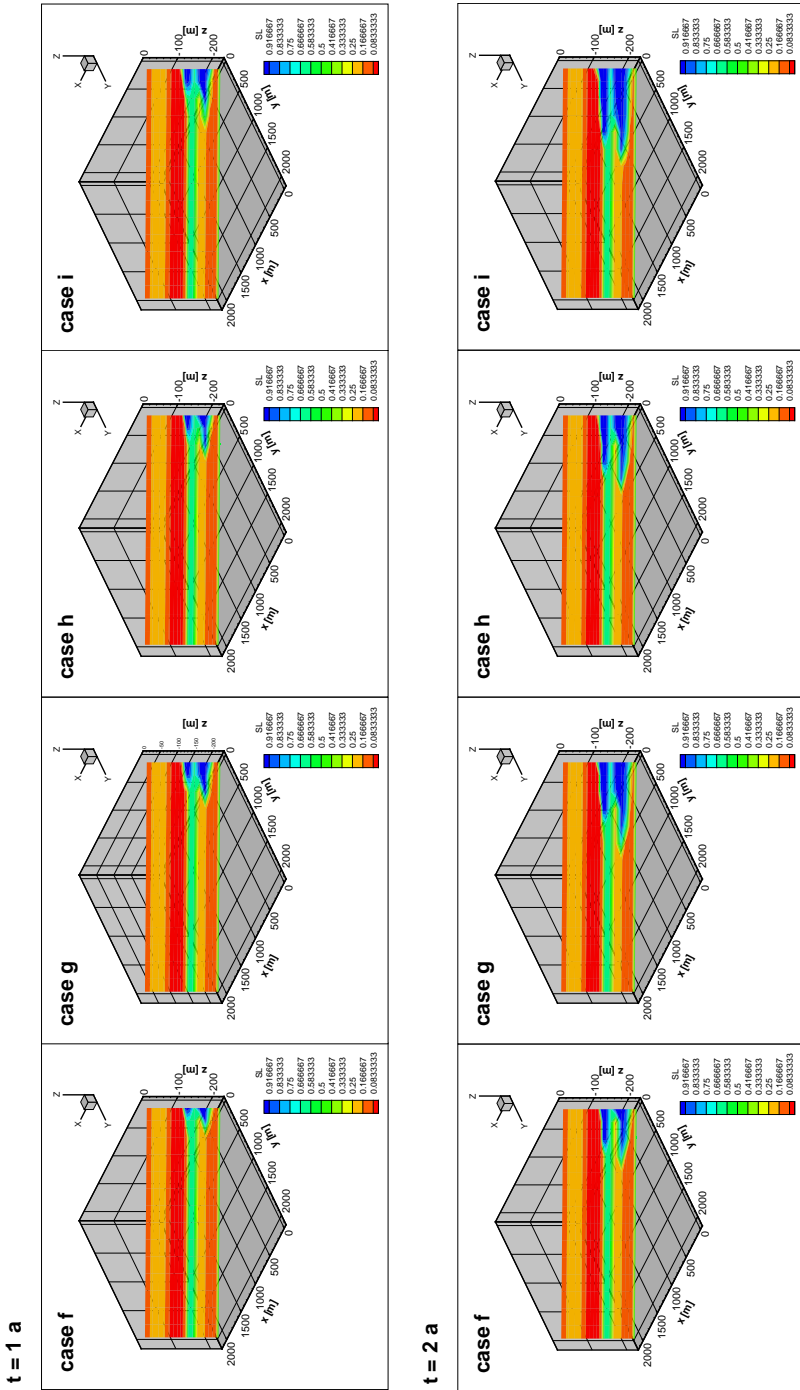


Figure 77: The layers Zyk9-11 are blocked with different  $H_2O$  injection rates: Case f 0.7523 kg/s and 2.1567 kg/s, Case g 2 1.5047 kg/s and 4.3135 kg/s, Case h2: 2.2571 kg/s and 6.4702 kg/s, Case i2 3.0094 kg/s and 8.6270 kg/s, (for each gridblock) (see Table 10). The development of the liquid saturation SL in the four cases Cases f to Case i is shown for 1 year and 2 years.

### $\text{CH}_4$ extraction and $\text{CO}_2$ injection phase after $\text{H}_2\text{O}$ blocking

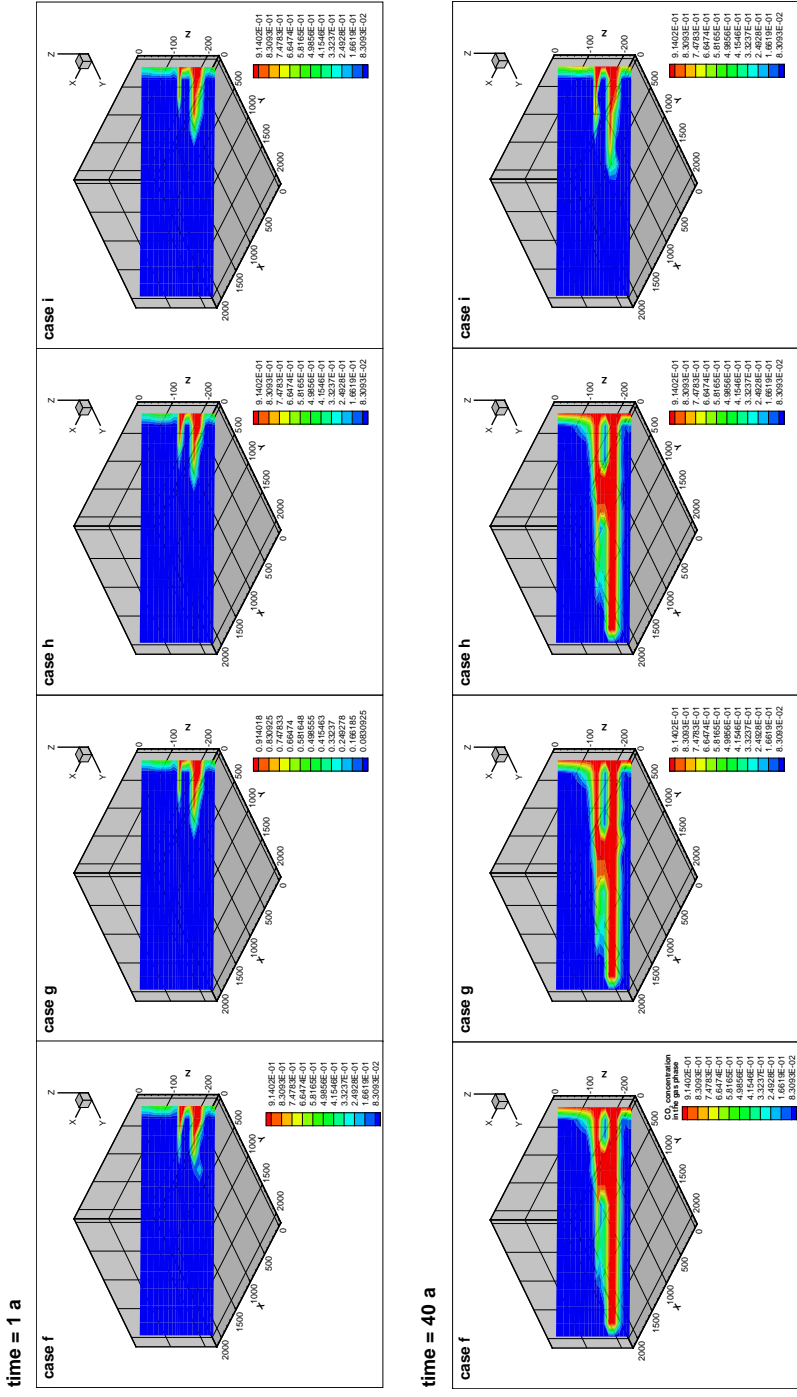


Figure 78: The  $\text{CO}_2$  mass fraction in the gas phase during the  $\text{CH}_4$  extraction and  $\text{CO}_2$  injection phase varies after blocking the layers Zyk13 and Zyk9-11 with different  $\text{H}_2\text{O}$  injection rates: Case f 0.7523 kg/s and 2.1567 kg/s, Case g2 1.5047 kg/s and 4.3135 kg/s, Case h2: 2.2571 kg/s and 6.4702 kg/s, Case i2 3.0094 kg/s and 8.6270 kg/s, (for each gridblock) (see Table 11).